

**BUILDABILITY AND MECHANICAL PERFORMANCE OF  
ARCHITECTURED CEMENT-BASED MATERIALS FABRICATED  
USING A DIRECT-INK-WRITING PROCESS**

by

**Mohamadreza Moini**

**A Dissertation**

*Submitted to the Faculty of Purdue University*

*In Partial Fulfillment of the Requirements for the degree of*

**Doctor of Philosophy**



Lyles School of Civil Engineering

West Lafayette, Indiana

August 2020

**THE PURDUE UNIVERSITY GRADUATE SCHOOL  
STATEMENT OF COMMITTEE APPROVAL**

**Dr. Jan Olek, Co-Chair**

Lyles School of Civil Engineering

**Dr. Pablo D. Zavattieri, Co-Chair**

Lyles School of Civil Engineering

**Dr. Jeffrey P. Youngblood, Co-Chair**

School of Materials Engineering

**Dr. Joseph J. Biernacki**

Department of Chemical Engineering

**Dr. Scott Jones**

National Institute of Standard and Technology

**Approved by:**

Dr. Dulcy M. Abraham

*To my mother,  
who first taught me how to convey my message to people,  
and for her always open, liberating, and nourishing conversations about life,  
that conferred upon me,  
the wisdom, to think with an open mind.*

*And to my father,  
for his steadiness, persistence, and perseverance,  
that bestowed upon me,  
pursuing life with determination, patience, and courage.*

## ACKNOWLEDGMENTS

First and foremost, I would like to thank my advisors, Prof. Jan Olek, Prof. Pablo Zavattieri, and Prof. Jeffrey Youngblood, for their support toward me throughout my Ph.D. studies at Purdue University. Their consistent and thorough insight and guidance over the past few years have strongly enriched my academic experience, my scholarly vision, and this research. I also would like to thank Professor Biernacki and Dr. Jones for their kind encouragements in the past years and for the fruitful discussions they have had with me during this research. I gratefully acknowledge the financial support of the National Science Foundation (NSF), Purdue College of Engineering, and Lyles School of Civil Engineering for funding and supporting my research.

I would also like to thank my friends and colleagues at Purdue University for their company and intellectual conversations, and the students who have assisted me in the laboratory for over three years.

Finally, my deepest gratitude goes to my parents, my brothers, and my sisters, for their unconditional love and support that has helped me navigate life with strength, especially during my Ph.D. studies.

# TABLE OF CONTENTS

LIST OF TABLES.....	9
LIST OF FIGURES.....	10
ABSTRACT.....	14
1. INTRODUCTION.....	15
1.1 Background and Motivation.....	15
1.2 Goal and Objectives.....	16
1.3 Hypotheses.....	18
1.4 References.....	19
2. RHEOLOGICAL PROPERTIES-BUILDABILITY RELATIONSHIP IN ADDITIVELY MANUFACTURED CEMENT-BASED ELEMENTS.....	22
2.1 Introduction.....	23
2.2 Materials and methods.....	25
2.2.1 Materials composition.....	25
2.2.2 Rheological characterization.....	26
2.2.3 Assessment of buildability.....	26
2.2.4 Assessment of downward deformation via isosceles triangle.....	27
2.3 Results and Discussion.....	28
2.3.1 Buildability.....	28
2.3.2 Prediction of Buildability.....	30
2.3.3 Buildability-Rheological Properties Relationship.....	31
2.3.4 Buildability, Elastic Modulus, and Prediction of Buildability.....	35
2.3.5 Isosceles triangle deformation test results.....	38
2.4 Conclusion.....	40
2.5 Appendix.....	41
2.6 Acknowledgement.....	43
2.7 References.....	44
3. ADDITIVE MANUFACTURING AND CHARACTERIZATION OF ARCHITECTURED CEMENT-BASED MATERIALS VIA X-RAY MICRO-COMPUTED TOMOGRAPHY.....	49
3.1 Introduction.....	50

3.2	Methods .....	51
3.2.1	3D-Printing Setup .....	51
3.3	Ink Design, Mixing Procedure, and Curing.....	52
3.3.1	Slicing and Design.....	54
3.3.2	Micro-CT and Scanning Specimens .....	55
3.4	Results and Discussion .....	56
3.4.1	3D-Printed Lamellar Architecture Micro-CT (0.4X and 4X scans) .....	56
3.4.2	Cast Specimen in 0.4X micro-CT (0.4X scan) .....	62
3.5	Summary.....	65
3.6	Acknowledgements.....	65
3.7	References.....	65
4.	QUANTITATIVE INVESTIGATION OF PROCESSING-MICROSTRUCTURE RELATIONSHIP IN 3D-PRINTED LAMELLAR CEMENT PASTE ELEMENTS VIA MICRO- COMPUTED TOMOGRAPHY .....	68
4.1	Introduction .....	69
4.2	Materials and Methods.....	70
4.2.1	3D-Printing, Slicing, and Design.....	70
4.2.2	Ink Design, Mixing Procedure, and Curing .....	71
4.2.3	Micro-Computed Tomography (Micro-CT) of the Elements .....	72
4.2.4	Image Analysis.....	72
4.3	Results.....	74
4.3.1	Micro-CT Characterization of the Entire Lamellar and Cast Elements (0.4X Scan) .	74
4.3.2	Analysis of the Categories of Pores in 3D-Printed Lamellar Element (0.4X Scan)...	78
4.3.3	Micro-CT Characterization of a Region of Interest (ROI) in 3D-Printed Lamellar Element (4X Scan) .....	81
4.4	Summary and Conclusion.....	86
4.5	Acknowledgments.....	88
4.6	References.....	88
5.	ADDITIVE MANUFACTURING AND PERFORMANCE OF ARCHITECTURED CEMENT-BASED MATERIALS.....	90
5.1	Manuscript .....	91

5.2	Experimental Section .....	107
5.3	Appendix.....	110
5.4	Acknowledgments.....	110
5.5	Supporting Information: Additive Manufacturing and Performance of Architected Cement-based Materials.....	111
5.6	References.....	125
6.	INFLUENCE OF INTERNAL ARCHITECTURES ON MECHANICAL RESPONSE AND FRACTURE BEHAVIOR OF 3D-PRINTED CEMENT-BASED ELEMENT UNDER COMPRESSIVE LOAD .....	129
6.1	Introduction .....	130
6.2	Methods .....	131
6.2.1	3D-Printing, Slicing, and Design.....	131
6.2.2	Ink Design, Mixing Procedure, and Curing .....	132
6.2.3	Sample Preparation and Mechanical Testing.....	133
6.2.4	Micro-Computed Tomography (Micro-CT) of Fractured Elements .....	133
6.3	Results and Discussion .....	134
6.3.1	Mechanical Properties of Cast and Architected Elements.....	134
6.3.2	Stress-Strain Behavior .....	135
6.3.3	Specific Compressive Strength (Sp. C.S.) .....	137
6.3.4	Specific Work-of-Failure (Sp. WOF).....	137
6.3.5	Discussion of the Overall Mechanical Responses .....	138
6.3.6	Fracture Behaviors.....	138
6.3.7	Cast Element (Tested in XY Plane).....	142
6.3.8	Lamellar Element (Tested in XY Plane) .....	142
6.3.9	Bouligand Element (Tested in XY Plane).....	143
6.3.10	Discussion on Fracture Behaviors.....	143
6.3.11	Discussion on Fracture Behavior in Relation to Mechanical Properties .....	144
6.4	Conclusion .....	145
6.5	Acknowledgments.....	146
6.6	Appendix.....	147
6.7	References.....	151

7. CONCLUSIONS AND RECOMMENDATIONS .....156

## LIST OF TABLES

Table 2.1. Cement paste materials composition containing a ranges of chemical high-range-water-reducing admixture (HRWRA) and viscosity-modifying-admixture (VMA). .....	25
Table 4.1. Comparison of the pore volumes of 3D-printed (lamellar) element and cast element based on the frequency plot presented in Figure 4.3f, collected during a 0.4X magnification. ....	78
Table 4.2. Analysis of the pore types and their corresponding range of volumes in 3D-printed (lamellar) element and cast element based on the frequency plot presented in Figure 4.3f, collected during 4X magnification .....	80
Table 4.3. Comparison of the range of volumes of three microstructural distinct phases based on the frequency plot presented in Figure 4.5g.....	84
Table 6.1. Rendition of the cast, 3D-printed lamellar, and 3D-printed Bouligand elements and their respective plane in which they were tested (shown in dashed lines) in uniaxial compression (dash lines represent testing plane).....	134

## LIST OF FIGURES

Figure 1.1. The five aspects of additively manufactured hcp elements .....	18
Figure 2.1. (a-c) Schematics of three main printability phenomena during 3D-printing of cement-based materials: inability to extrude, two failure mechanisms, yielding and buckling and (d-i) Representative images of these three phenomena in 3D-printed cement paste elements with various materials composition.....	24
Figure 2.2. (a) 3D-printer setup for cement-based materials using a gantry system (Ultimaker 2 Extended+) and stepper motor-based extrusion (Discov3ry) system for 3D-printing of (b) A hollow cylinders geometry with a diameter of 70 mm and thickness of 1.63 mm used for assessment of buildability. ....	27
Figure 2.3. (a) Design, (b,c) Stereolithography, and curing of 3D-printing of an isosceles triangle used as a platform for (d) 3D-printing cement paste over varied span length, followed by (e) Hardening of cement paste, (f) CT-scan of the hardened cement paste, and (g) Quantification of deflection ( $\delta$ ) of printed individual cement paste filaments with respect to the horizontal line. ....	28
Figure 2.4. Assessment of buildability of hollow cylinders based on the number of successfully printed layers (height of $\sim 1$ mm per layer) in various materials composition: (a) Plain paste, (b) Paste with chemical admixtures at 53% solid loading, and (c) Paste with chemical admixture at $\sim 55\%$ solid loading .....	29
Figure 2.5. Correlation between buildability (number of printed layers) and rheological properties: (a) Shear Modulus, $G$ , (b) Complex shear modulus, $G^*$ , (c) Storage modulus, $G'$ , (d) Loss modulus, $G''$ , (e) Yield stress, $\tau_y$ , (f) Yield strain, $\gamma_{critical}$ , (g) Complex viscosity $\eta^*$ .....	33
Figure 2.6. (a) Modulus of elasticity, $E$ vs. predicted buildability, $L$ , (b) Modulus of elasticity, $E$ vs. measured buildability, (c) Predicted buildability, $L$ vs. measured buildability. ....	36
Figure 2.7. Mid-span deflection vs. span length of individual cement paste filaments with various materials compositions: (a) Plain paste with W/C ratio of 0.35, 0.3, and 0.275, (b) Paste with constant W/C ratio of 0.275 and various chemical admixtures, and (c) Paste with constant W/C ratio of 0.25 and various chemical admixtures. ....	39
Figure 3.1. 3D printer setup: a) Gantry 3D printer (Ultimaker 2 Extended +) and stepper motor-based extrusion (Discov3ry) system; b) Syringe and plunger mounted onto the stepper motor system; (c) Nozzle holder assembly mounted onto the 3D printer gantry guide rods; d) Nozzle holder assembly and the female luer lock used to connect the tube to the nozzle; e) male luer lock used to connect syringe to the tube; f) nozzle and luer locks shown separately .....	52
Figure 3.2. Schematics of lamellar architectures: a) Printing path of individual layers; b) Printing path of a cube specimen and; c) Cross-section of the specimen with lamellar architecture; d) 3D-printed lamellar architecture cube via DIW .....	54
Figure 3.3. X-ray micro-CT images of the microstructure of 3-days old paste specimen with lamellar architecture collected during 0.4X scan: a) 2D projection on the XZ plane; b) 2D	

projection on the YZ plane; c) 2D projection on the XY plane, and; d) Three-dimensional rendition of the entire volume of the specimen .....	57
Figure 3.4. CT images of the microstructure of 3-days old intact specimen with lamellar architecture collected during 4X scan: a) XZ; b) YZ; c) XY planes; d) 3D image of the solid skeleton; e) 3D image of pore network .....	59
Figure 3.5. Schematic illustration of arrangements of filaments and shapes of the pores along the Y direction: a) As-designed pattern in lamellar architecture containing diamond-shaped pore and; b) Rearranged filament pattern showing triangular-shaped pores (similar to those depicted in 4X CT image (Figure 3.4 e) .....	61
Figure 3.6. X-ray micro-CT images of the 3-days old intact cast specimen collected during the 0.4X scan: a) 2D projection on the XY plane and; b) 3D rendition of the entire specimen .....	63
Figure 4.1. Schematics of printing path and resulting 3D-printed specimen with lamellar architected element: (a) schematics of printing path of individual layers of lamellar architecture; (b) schematics of printing path of the entire element; (c) schematics of cross-section of the lamellar element; and (d) resulting 3D-printed lamellar element. ....	71
Figure 4.2. Representative visualization of applied K-means clustering segmentation algorithm to a (a) raw 2D sliced image of the entire cross section of an intact lamellar architected element (viewed in XY plane) collected during a 0.4X scan; and (b) its corresponding segmented image of 2 clusters (solid in green and pores in blue); (c) raw 2D sliced image of the entire cross section of an intact lamellar architected element (on the XY plane) collected during a 4X scan; and (d) its corresponding segmented image of 3 clusters (hydrated cement paste in green, anhydrous grains in red, and pores in blue).....	73
Figure 4.3. Comparison of the microstructure and quantification of phases in the entire cast (a1-e1,f) and 3D-printed lamellar (a2-e2,f) hardened cement paste elements using 588 and 714 slices captured during a 0.4X CT scan, respectively: (a1,a2) three-dimensional rendition of the entire volume of the elements; (b1,b2) two typical raw slice images; (c1,c2) two typical slice images processed using K-means segmentation technique; (d1,d2) histograms of pore (blue), and solid (green) phases; (e1,e2) total volumetric percentages of pore and solid phases; and (f) frequency plot of pore phases (frequency of given pore volume) of the entire volume of the elements.....	76
Figure 4.4. (a) schematics of the arrangement of filaments in the cross-section of the lamellar element and (b) Visualization of representative examples of macro-pores, micro-channels, micro-pores, and interfacial regions. ....	79
Figure 4.5. Quantification of phases of the microstructure of a representative region of interest of intact 3D-printed lamellar hardened cement paste element using 403 slices captured during a 4X CT scan: (a) three-dimensional rendition of the entire volume of the element; (b) three-dimensional rendition of representative region of interest (ROI); (c) a typical raw slice image from the representative region; (d) a typical slice image processed using K-means segmentation; (e) histogram of pore (blue), hydrated (green), and anhydrous (red) phases; (f) volumetric percentage of each phase; and (g) Frequency plot (frequency of given pore volume) of the entire representative region (i.e., sliced images). ....	82

Figure 5.1. Various 3D printed architectures of hardened cement paste (hcp) elements; a) Compliant structure with honeycomb architecture; b) cellular sandwich panel prism with solid top and bottom layers; c-d) Bouligand architecture with, respectively, pitch angles  $\gamma = 2^\circ$  and  $45^\circ$ ; e) 3D rendition of the design of Bouligand architecture with  $\gamma = 45^\circ$  and; f) 3D rendition of the entire volume of Bouligand architecture with  $\gamma = 45^\circ$  from X-ray micro-CT. All scale bars are 10.0 mm long. .... 93

Figure 5.2. Mechanical response of 3D printed solid prisms with various architectures tested in 3PB; a) Schematic of the top face (X-Z plane) of the specimens showing orientation of the filaments; b) Schematic of the 3PB test; c) Specific modulus of rupture of 3D printed and cast elements; d-f) Post-failure images of specimens with  $0^\circ$ ,  $45^\circ$  and  $90^\circ$  filament orientation illustrating crack paths (as viewed along Z axis); g-i) Crack paths on the bottom face of specimens (as viewed along the Y axis); j-k) micro-cracks along the interfaces in prisms with  $0^\circ$  and  $45^\circ$  filament orientations (viewed in X-Y plane, along Z axis) and; i) uncracked interfaces in prism  $90^\circ$  with filament orientation (viewed in the X-Y plane along the Z-axis. Unless indicated, all scale bars are 1.50 mm long. .... 95

Figure 5.3. Mechanical response of Bouligand architecture using ball-on-three-balls test; a) Load-displacement for printed and cast disc specimens, including screenshot of acoustic spectrum recorded during testing; b) Specific modulus of rupture; c) ork of failure, and d) Modulus of rupture (MOR) versus relative density for Bouligand architectures with varying pitch angles ( $8^\circ$ ,  $15^\circ$ ,  $30^\circ$ ,  $45^\circ$ ,  $90^\circ$ ) and percentages of infill (60% and 100%) compared to MOR of cast control discs; e-g) Views of bottom faces of discs with different Bouligand architecture; h) Schematic of Bouligand architecture with helicoidal alignment of filaments. .... 97

Figure 5.4. Crack paths and fracture patterns of various 3D printed Bouligand architectures; a1-a8)  $\gamma = 8^\circ$ , 100% infill; b1-b6)  $\gamma = 8^\circ$ , 60% infill; c1-c3)  $\gamma = 45^\circ$ , 60% infill and; d1-d2)  $\gamma = 30^\circ$ , 60% infill after B3B test. All scale bars are 1.0 mm long. .... 99

Figure 6.1. Schematics of printing path and resulting 3D-printed specimens with (a1-a4) lamellar architected element and (b1-b4) Bouligand architected elements: (a1) schematics of printing path of individual layers of lamellar architecture; (b1) Schematics of printing path of individual layers of Bouligand architecture (with pitch angle of  $\alpha = 3^\circ$  in Z direction); (a2,b2) schematics of printing path of the entire elements; (a3) schematics of the cross-section of the elements; (a4) resulting 3D-printed lamellar and Bouligand architected elements. .... 132

Figure 6.2. Comparison of (a) stress-strain; (b) specific compressive strength (Sp. C.S.) and (c) Specific work-of-failure (Sp. WOF) of the cast, lamellar, and Bouligand architected hcp elements at the age of 3 days quantified up to 20% drop of the peak load; and (d) corresponding statistical differences between them. .... 135

Figure 6.3. Post-fracture X-ray micro-CT images of the microstructure of cast hardened cement paste specimen tested in XY plane and collected during 0.4X scan: (a) 2D view on the XZ plane; (b) 2D view on the YZ plane; (c) 2D view on the XY plane; and (d) three-dimensional rendition of the entire volume of the element. .... 139

Figure 6.4. Post-fracture X-ray micro-CT images of the microstructure of 3D-printed hardened cement paste specimen with lamellar architecture tested in XY plane and collected during 0.4X

scan: (a) 2D view on the XZ plane; (b) 2D view on the YZ plane; (c) 2D view on the XY plane; and (d) three-dimensional rendition of the entire volume of the element. ....140

Figure 6.5. Post-fracture X-ray micro-CT images of the microstructure of 3D-printed hardened cement paste specimen with Bouligand architecture tested in XY plane and collected during 0.4X scan: (a) 2D view on the XZ plane; (b) 2D view on the YZ plane; (c) 2D view on the XY plane; (e) 2D view on the XY plane at three different heights of the specimen (f) three-dimensional rendition of the entire volume of the specimen. ....141

## **ABSTRACT**

Additive Manufacturing (AM) allows for the creation of elements with novel forms and functions. Utilizing AM in development of components of civil infrastructure allows for achieving more advanced, innovative, and unique performance characteristics. The research presented in this dissertation is focused on development of a better understanding of the fabrication challenges and opportunities in AM of cement-based materials. Specifically, challenges related to printability and opportunities offered by 3D-printing technology, including ability to fabricate intricate structures and generate unique and enhanced mechanical responses have been explored. Three aspects related to 3D-printing of cement-based materials were investigated. These aspects include: fresh stability of 3D-printed elements in relation to materials rheological properties, microstructural characteristics of the interfaces induced during the 3D-printing process, and the mechanical response of 3D-printed elements with bio-inspired design of the materials' architecture. This research aims to contribute to development of new pathways to obtain stability in freshly 3D-printed elements by determining the rheological properties of material that control the ability to fabricate elements in a layer-by-layer manner, followed by the understanding of the microstructural features of the 3D-printed hardened cement paste elements including the interfaces and the pore network. This research also introduces a new approach to enhance the mechanical response of the 3D-printed elements by controlling the spatial arrangement of individual filaments (i.e., materials' architecture) and by harnessing the weak interfaces that are induced by the 3D-printing process.

# 1. INTRODUCTION

There is a great need for researchers to apply scientific approaches to enhance the understanding of engineering materials and to develop new knowledge toward creating more advanced, durable, and ecologically viable built environments. The overall goal of the research presented in this dissertation is to contribute to the development of more advanced components of civil infrastructure using additive manufacturing technologies. To achieve this goal, this dissertation is oriented toward overcoming the fabrication challenges of additive manufacturing of cement-based materials, specifically printability, while exploring the opportunities offered by this technology, such as the ability to fabricate components with controlled architecture, in order to generate novel mechanical responses. This dissertation demonstrates a pathway to achieve novel architected cement-based elements using additive manufacturing on a small scale, that can enable new approaches in the design and fabrication of civil infrastructure components on a large scale.

## 1.1 Background and Motivation

There is a rising interest in the use of additive manufacturing (also known and interchangeably used as 3D-printing) technologies in the design and development of innovative cement-based materials with unique and novel performances and functionalities [1–8]. This interest is mostly in response to the increasing demand for improvements in durability sustainability, and mechanical performance of the materials and the construction productivity that is emphasized in areas such as transportation and energy infrastructures [9–11]. However, additive manufacturing of cement-based materials is a rather nascent field. Despite recent developments in fabrication of materials using 3D-printing technologies, there are limited research efforts that focus on the understanding of the mechanical behavior of additively manufactured cement-based materials. Nevertheless, such an understanding of the mechanical responses of additively manufactured cement-based materials is necessary (across multiple scales) as it is a precursor to the development of an established design pathway in the future.

Several fabrication challenges and design opportunities continue to rise in the development of cement-based materials using additive manufacturing technologies [12,13]. Direct-ink-writing

(DIW) is an extrusion-based additive manufacturing technique that uses a 3D-printer to fabricate structural elements in a layer-by-layer deposition process [14–18]. This technique allows for utilization and continuous deposition of a variety of colloid, slurry, and paste materials (typically with ceramic and cementitious base) to create the desired 3D elements using a computer-controlled 3D printer. 3D-printing of cement-based elements from fresh cement pastes and mortars depends upon the ability to maintain the shape of the elements upon deposition (i.e., extrusion in case of a DIW process) especially at early-stages of cement hydration [19,20]. The low early-age load-bearing capacity of cement-based materials triggers research questions about materials composition and suitable rheological properties. Moreover, the brittle behavior of the hardened cement-based materials, along with the presence of layer-wise interfaces from the additive manufacturing process, represents another significant challenge with respect to the overall mechanical behavior of 3D-printed elements.

On the other hand, opportunities offered by the 3D-printing process are quite unique and promising. Cleverly designed and additively manufactured materials (such as ceramic, metallic, polymeric, and composite) have been shown in the past to allow for control of the materials' architecture (by a purposeful arrangement of geometrical patterns of the printed filaments). Materials with such architectures have demonstrated enhanced mechanical performances, such as energy absorption, strain recovery, impact resistance, and load-bearing capacity [21–26]. Desirable and unique performance characteristics have also been proven achievable using novel forms and additive manufacturing of cement-based materials, although the number of studies in this area is limited [27–30]. The research presented in in this dissertation focuses on addressing the printability of fresh cement-based materials at early ages, defined as the combination of extrudability and buildability, as well as exploiting the opportunities of applying novel architectures into the design and fabrication of cement-based materials.

## **1.2 Goal and Objectives**

The main goal of the research presented in this dissertation is to contribute to the development of components of advanced concrete infrastructure by using additive manufacturing technologies. To achieve this goal, five objectives are identified and are discussed in details in the subsequent chapters:

- (1) To understand the role of rheological properties of the printable material on the buildability of elements fabricated via the Direct-Ink-Writing (DIW) process.
- (2) To understand the microstructural characteristics of the 3D-printed hardened cement paste (hcp) elements.
- (3) To understand the pore characteristics of the microstructure of 3D-printed hcp elements.
- (4) To understand the role of the internal architectures and the interfaces on the mechanical behavior of 3D-printed hcp elements under biaxial flexure.
- (5) To understand the role of the internal architectures and interfaces on the mechanical behavior of 3D-printed hcp elements under compression.

Chapter two focuses on the challenges related to the control of materials rheological properties that facilitates the buildability of 3D-printed elements. Buildability is specifically defined as the height of successfully printed element before it undergoes failure by either yielding or buckling. Chapter three focuses on the microstructural aspects of the 3D-printed elements, such as pores and interfaces that are generated during the 3D-printing process and remain present in the hardened microstructure. Chapter four explicitly focuses on such characteristics of the pore phase as pore frequency distribution and the connectivity of porosity at the interfaces between filaments of the 3D-printed hcp elements. Chapter five focuses on the opportunities related to harnessing the interfaces present in 3D-printed hcp elements by using novel bio-inspired architectures (such as Bouligand architecture) created by the DIW process. Chapter six focuses on the role the interfaces and previously mentioned novel bio-inspired architectures (such as lamellar and Bouligand architectures) in controlling the mechanical response and fracture behaviors of 3D-printed hcp elements in compression. Chapter seven summarizes the overall findings and highlights the future research questions that can be postulated based on the conclusions drawn from this research. In short, as demonstrated in **Figure 1.1**, this dissertation is structured to discuss the printability in DIW process in chapter two, the qualitative and quantitative characteristics of the hardened microstructure in chapters three and four, and the mechanical properties and performances of the additively manufactured architected hcp elements in chapters five and six.

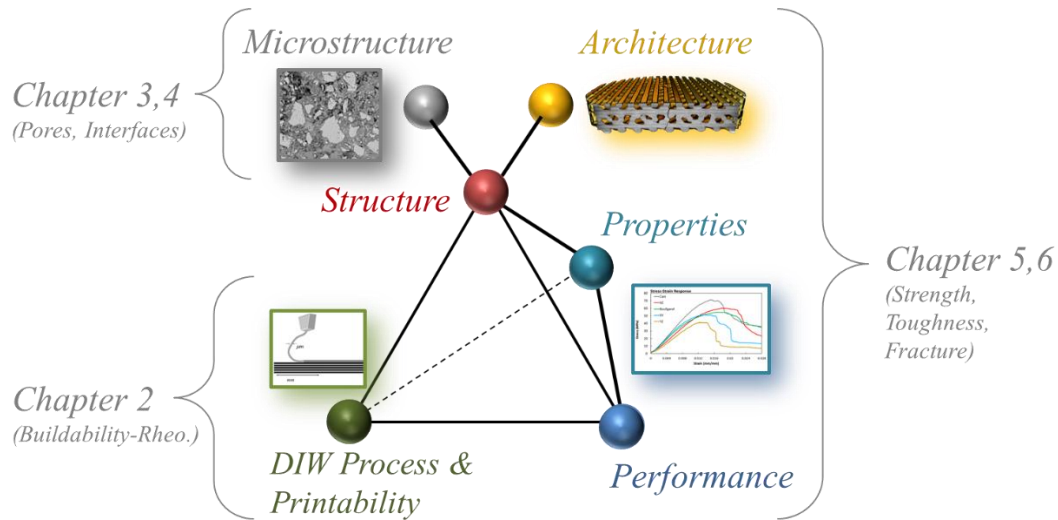


Figure 1.1. The five aspects of additively manufactured hcp elements

### 1.3 Hypotheses

Each chapter of this dissertation examines a specific hypothesis. These hypotheses are articulated as follows: The hypothesis of chapter two is that elastic shear moduli control the early-age buildability in 3D-printed cement paste elements. This hypothesis is investigated investigating materials with a wide range of rheological properties and connecting these properties with buildability. Due to the layer-by-layer nature of the DIW process and the visible layer of water on the surface of freshly deposited cement paste filaments, the potential for the formation of a ‘weak’ interface is presumed. The hypothesis of chapter three is that the interfaces between the deposited filaments are more porous and thereby weaker, than the bulk hcp materials and, therefore, are weaker than the material. This hypothesis was examined by using an X-ray microscope to conduct an interior tomography of the entire 3D-printed elements as well as a selected region of interest (ROI) within the element. The hypothesis of chapter four is that interfacial porosity presented in chapter three results in inherent connectivity of pores in 3D-printed elements. This hypothesis of chapter four was examined by performing image analysis on the tomography data described in chapter three. The hypothesis of chapter five is that combining weak interfaces with Bouligand architectures can improve the toughness of the 3D-printed elements by spreading the damage through the interfaces, without sacrificing the strength. A ball-on-three-ball test was used to examine the mechanical responses of 3D-printed elements. The hypothesis of chapter six is that materials' internal architecture and weak interfaces determine the overall mechanical response and

fracture behaviors in compression. An additional hypothesis of chapter six is similar to that of chapter five in that the weak interfaces and Bouligand architectures are expected to improve the toughness of the 3D-printed elements in compression without sacrificing the strength by spreading the damage at the pre-existing porous (and helical) interfaces. This hypothesis of chapter six was examined by using an X-ray microscope to conduct interior tomography of the fractured 3D-printed elements and by determining the response under compressive load.

#### 1.4 References

- [1] T. Wangler, R.J. Flatt, First RILEM International Conference on Concrete and Digital Fabrication – Digital Concrete, 2018.
- [2] R.A. Buswell, W.R.L. De Silva, S.Z. Jones, J. Dirrenberger, Cement and Concrete Research 3D printing using concrete extrusion: A roadmap for research, *Cem. Concr. Res.* 112 (2018) 37–49. doi:10.1016/j.cemconres.2018.05.006.
- [3] G. De Schutter, K. Lesage, V. Mechtcherine, V. Naidu, G. Habert, I. Agusti-juan, Vision of 3D printing with concrete — Technical, economic and environmental potentials, *Cem. Concr. Res.* 112 (2018) 25–36. doi:10.1016/j.cemconres.2018.06.001.
- [4] D. Lowke, E. Dini, A. Perrot, D. Weger, C. Gehlen, B. Dillenburger, Particle-bed 3D printing in concrete construction – Possibilities and challenges, *Cem. Concr. Res.* 112 (2018) 50–65. doi:10.1016/j.cemconres.2018.05.018.
- [5] B.N. Sanjayan, Jay G., Ali Nazari, ed., 3D Concrete Printing Technology: Construction and Building Applications, Butterworth-Heinemann, 2019.
- [6] N. Labonnote, A. Rønnquist, B. Manum, P. Rüther, Additive construction: State-of-the-art, challenges and opportunities, *Autom. Constr.* 72 (2016) 347–366. doi:10.1016/j.autcon.2016.08.026.
- [7] S. Lim, T. Le, J. Webster, R. Buswell, S. Austin, A. Gibb, T. Thorpe, Fabricating Construction Components Using Layered Manufacturing Technology, *Glob. Innov. Constr. Conf.* 2009. (2009) 512–520. doi:10.1016/j.autcon.2011.06.010.
- [8] H. Yin, M. Qu, H. Zhang, Y. Lim, 3D Printing and Buildings: A Technology Review and Future Outlook, *Technol. + Des.* 2 (2018) 94–111. doi:10.1080/24751448.2018.1420968.
- [9] A.W. Herrmann, “Asce 2013 report card for america’s infrastructure.,” IABSE Symp. Report, *Int. Assoc. Bridg. Struct. Eng.* 99, (2013) 9–10.

- [10] D.D. Camacho, P. Clayton, W.J. O'Brien, C. Seepersad, M. Juenger, R. Ferron, S. Salamone, Applications of additive manufacturing in the construction industry - A forward looking review, *Autom. Constr.* 89 (2018) 110–119.
- [11] J.J. Biernacki, J.W. Bullard, G. Sant, K. Brown, F.P. Glasser, S. Jones, T. Ley, R. Livingston, L. Nicoleau, J. Olek, F. Sanchez, R. Shahsavari, P.E. Stutzman, K. Sobolev, T. Prater, Cements in the 21 st century: Challenges, perspectives, and opportunities, *J. Am. Ceram. Soc.* 100 (2017) 2746–2773. doi:10.1111/jace.14948.
- [12] J.D. Silva, W.R. Leal de, S.Z. Jones, 3D printing using concrete extrusion: a roadmap for research, *Cem. Concr. Res.* (2018) (this issue). doi:10.1016/j.cemconres.2018.05.006.
- [13] T. Wangler, N. Roussel, F.P. Bos, T.A.M. Salet, R.J. Flatt, Cement and Concrete Research Digital Concrete: A Review, 123 (2019). doi:10.1016/j.cemconres.2019.105780.
- [14] J.A. Lewis, Direct-write assembly of ceramics from colloidal inks, *Curr. Opin. Solid State Mater. Sci.* 6 (2002) 245–250. doi:10.1016/S1359-0286(02)00031-1.
- [15] J.E. Smay, J. Cesarano, J.A. Lewis, Colloidal inks for directed assembly of 3-D periodic structures, *Langmuir.* 18 (2002) 5429–5437. doi:10.1021/la0257135.
- [16] J.A. Lewis, G.M. Gratson, Direct writing in three dimensions, *Mater. Today.* 7 (2004) 32–39. doi:10.1016/S1369-7021(04)00344-X.
- [17] J.A. Lewis, Direct ink writing of 3D functional materials, *Adv. Funct. Mater.* 16 (2006) 2193–2204. doi:10.1002/adfm.200600434.
- [18] R.A. Barry, R.F. Shepherd, J.N. Hanson, R.G. Nuzzo, P. Wiltzius, J.A. Lewis, Direct-write assembly of 3D hydrogel scaffolds for guided cell growth, *Adv. Mater.* 21 (2009) 2407–2410. doi:10.1002/adma.200803702.
- [19] L. Rueschhoff, W. Costakis, M. Michie, J. Youngblood, R. Trice, Additive Manufacturing of Dense Ceramic Parts via Direct Ink Writing of Aqueous Alumina Suspensions, *Int. J. Appl. Ceram. Technol.* 13 (2016) 821–830. doi:10.1111/ijac.12557.
- [20] W.J. Costakis, L.M. Rueschhoff, A.I. Diaz-Cano, J.P. Youngblood, R.W. Trice, Additive manufacturing of boron carbide via continuous filament direct ink writing of aqueous ceramic suspensions, *J. Eur. Ceram. Soc.* 36 (2016) 3249–3256. doi:10.1016/j.jeurceramsoc.2016.06.002.
- [21] Z. Jia, L. Wang, 3D printing of biomimetic composites with improved fracture toughness, *Acta Mater.* 173 (2019) 61–73. doi:10.1016/j.actamat.2019.04.052.

- [22] D. Herzog, V. Seyda, E. Wycisk, C. Emmelmann, G.T. Gray, V. Livescu, P.A. Rigg, C.P. Trujillo, C.M. Cady, S.R. Chen, J.S. Carpenter, T.J. Lienert, S.J. Fensin, T. Tancogne-Dejean, A.B. Spierings, D. Mohr, H. Manzano, J.S. Dolado, A. Ayuela, F. Abdeljawad, D.S. Bolintineanu, A. Cook, H. Brown-Shaklee, C. DiAntonio, D. Kammler, A. Roach, A. Pineau, A.A. Benzerga, T. Pardoen, S. Xiao, H. Mei, D. Han, W. Yuan, L. Cheng, C. Zhang, X. Hu, T. Sercombe, Q. Li, Z. Wu, P. Lu, Additive manufacturing of metals, *Acta Mater.* 117 (2016) 371–392. doi:10.1016/j.actamat.2016.07.019.
- [23] M.R. Mansouri, H. Montazerian, S. Schmauder, J. Kadkhodapour, 3D-printed multimaterial composites tailored for compliancy and strain recovery, *Compos. Struct.* 184 (2018) 11–17. doi:10.1016/j.compstruct.2017.09.049.
- [24] X. Zheng, W. Smith, J. Jackson, B. Moran, H. Cui, D. Chen, J. Ye, N. Fang, N. Rodriguez, T. Weisgraber, C.M. Spadaccini, Multiscale metallic metamaterials, *Nat. Mater.* 15 (2016) 1100–1106. doi:10.1038/nmat4694.
- [25] G.X. Gu, M. Takaffoli, M.J. Buehler, Hierarchically Enhanced Impact Resistance of Bioinspired Composites, *Adv. Mater.* 29 (2017) 1–7. doi:10.1002/adma.201700060.
- [26] M. DeVries, G. Subhash, A. Mcghee, P. Ifju, T. Jones, J. Zheng, V. Halls, Quasi-static and Dynamic Response of 3D-printed Alumina, *J. Eur. Ceram. Soc.* 38 (2018) 3305–3316. doi:10.1016/j.jeurceramsoc.2018.03.006.
- [27] S.M. Sajadi, P.J. Boul, C. Thaemlitz, A.K. Meiyazhagan, A.B. Puthirath, C.S. Tiwary, M.M. Rahman, P.M. Ajayan, Direct Ink Writing of Cement Structures Modified with Nanoscale Additive, 1801380 (2019) 1–10. doi:10.1002/adem.201801380.
- [28] Y. Xu, H. Zhang, E. Schlangen, M. Lukovi, B. Savija, Cementitious cellular composites with auxetic behavior, 111 (2020). doi:10.1016/j.cemconcomp.2020.103624.
- [29] M. Moini, J. Olek, J.P. Youngblood, B. Magee, P.D. Zavattieri, Additive Manufacturing and Performance of Architected Cement-Based Materials, *Adv. Mater.* 30 (2018). doi:10.1002/adma.201802123.
- [30] J.A. Rosewitz, H.A. Choshali, N. Rahbar, Bioinspired design of architected cement-polymer composites, *Cem. Concr. Compos.* 96 (2019) 252–265. doi:10.1016/j.cemconcomp.2018.12.010.

## 2. RHEOLOGICAL PROPERTIES-BUILDABILITY RELATIONSHIP IN ADDITIVELY MANUFACTURED CEMENT-BASED ELEMENTS

This chapter contains experimental data collected by Mohamadreza Moini. Data conceptualization was a collaborative effort with Jeffrey P. Youngblood, Jan Olek, and Pablo D. Zavattieri. The manuscript was written by Mohamadreza Moini and edited by Jeffrey P. Youngblood, Jan Olek, and Pablo D. Zavattieri.

### Highlights

- Shear Modulus  $G$ , is the most relevant rheological property to control buckling failure in 3D-printed cement paste materials.
- An isosceles triangle was introduced for assessment of cement paste early-age deformation over varied span lengths and for understanding the working mechanisms of chemical admixtures on early-age deformations of 3D-printed elements.
- Euler's theory was used for prediction of buildability and overestimated the buildability by 93% to 194%, mainly due to assuming ideal geometry with no initial or printing imperfection and linear elasticity.

### Abstract

Ability to extrude and to achieve shape stability of layer-wised additively manufactured cement-based elements depends upon the early-age rheological properties (shear moduli, yield stress, viscosity) of the deposited materials. Upon successful extrusion, buildability challenges can manifest in two common failure mechanisms: *yielding* at lower layers and *buckling* of the element. However, it is yet unclear that among various rheological properties which one controls the early-age materials' deformation during printing processes and contributes to the resulting buildability of the elements. This chapter focuses on how buildability is dependent upon rheological properties as well as predicting the buildability using a buckling theoretical framework. Specifically, the relationship between early-age rheological properties of various cement pastes and the buildability of hollow cylinders dominated by buckling failure mechanism was investigated. It was found that certain shear moduli of the fresh pastes ( $G$ ,  $G^*$ , and  $G'$ ) obtained from oscillatory shear stress

sweep tests (within the first 30 minutes of hydration) correlates well with the buildability of hollow elements more than other rheological properties (loss modulus  $G''$ , yield stress  $\sigma_{yield}$ , yield strain  $\gamma_{yield}$ , and complex viscosity  $\eta^*$ ). Measured shear modulus ( $G$ ) was used to calculate elastic modulus ( $E$ ) of the pastes using the assumed value of the 0.5 for Poisson's ratio ( $\nu$ ) for fresh cement paste. Euler's buckling theory was used to predict buildability (height of the element) of hollow cylinders. It was found that Euler's theory overestimates the buildability by 93% to 194%, mainly due to assuming ideal geometry (and no initial or printing imperfection) and linear elasticity. An isosceles triangle was introduced as a support structure and was used for assessment of early-age deformation of individual cement paste filaments over varied span lengths. The results provide insight into the role of the solid content and working mechanisms of chemical admixtures on improving materials' design and early-age deformations.

**Keywords:** Fresh cement paste, Failure mechanisms, Early-age deformation, Buildability

## 2.1 Introduction

Extrusion-based additive manufacturing (AM) of cement-based material, similar to other ceramic materials, is dependent upon the ability to fabricate elements with suitable shape stability [1–4]. Ability to extrude and to achieve shape stability in layer-wised additively manufactured cement-based elements depends upon the early-age rheological properties (shear moduli, yield stress, viscosity) of the deposited materials [5–8]. More specifically, three printability phenomena as depicted in Figure 1 can occur that poses challenges to the fabrication process: (i) inability to extrude the material from the nozzle (**Figure 2.1a**), and (ii) inability to successively build-up layer upon layer due to deformation at the bottom layers (i.e., yielding, **Figure 2.1b**) or (iii) due to buckling of the element (**Figure 2.1c**). In additive manufacturing of cement paste, inability to extrude can translate to intermittent extrusion or no extrusion (**Figure 2.1d,e**). Once the extrusion is achieved, buildability challenges can manifest itself in two common failure mechanisms: yielding (**Figure 2.1f,g**) at lower layers and buckling of the element (**Figure 2.1h,i**) [9,10]. Once yielding is overcome, buckling will be the ultimate candidate for the failure of the element.

The investigation of shape stability of 3D-printed elements [1,9–16] and early-age deformations of cement-based materials [17–20] is a growing area of research. However, it is yet unclear that among various rheological properties which one controls the early-age deformations

of cement paste during printing processes and contributes to the resulting buildability of the elements [10]. Similarly, the fresh stability of cement-based materials at the lack of formwork remains a challenge [21]. This chapter focuses on how buildability is dependent upon rheological properties as well as predicting the buildability using a buckling framework. Specifically, the relationship between early-age rheological properties of various cement pastes and the buildability of hollow cylinders dominated by buckling failure mechanism was investigated. Measured shear modulus ( $G$ ) was used to calculate elastic modulus ( $E$ ) of the pastes using the assumed value of the 0.5 for Poisson's ratio ( $\nu$ ) for fresh cement paste. Euler buckling theory was used to predict buildability (height of the element) before it buckles.

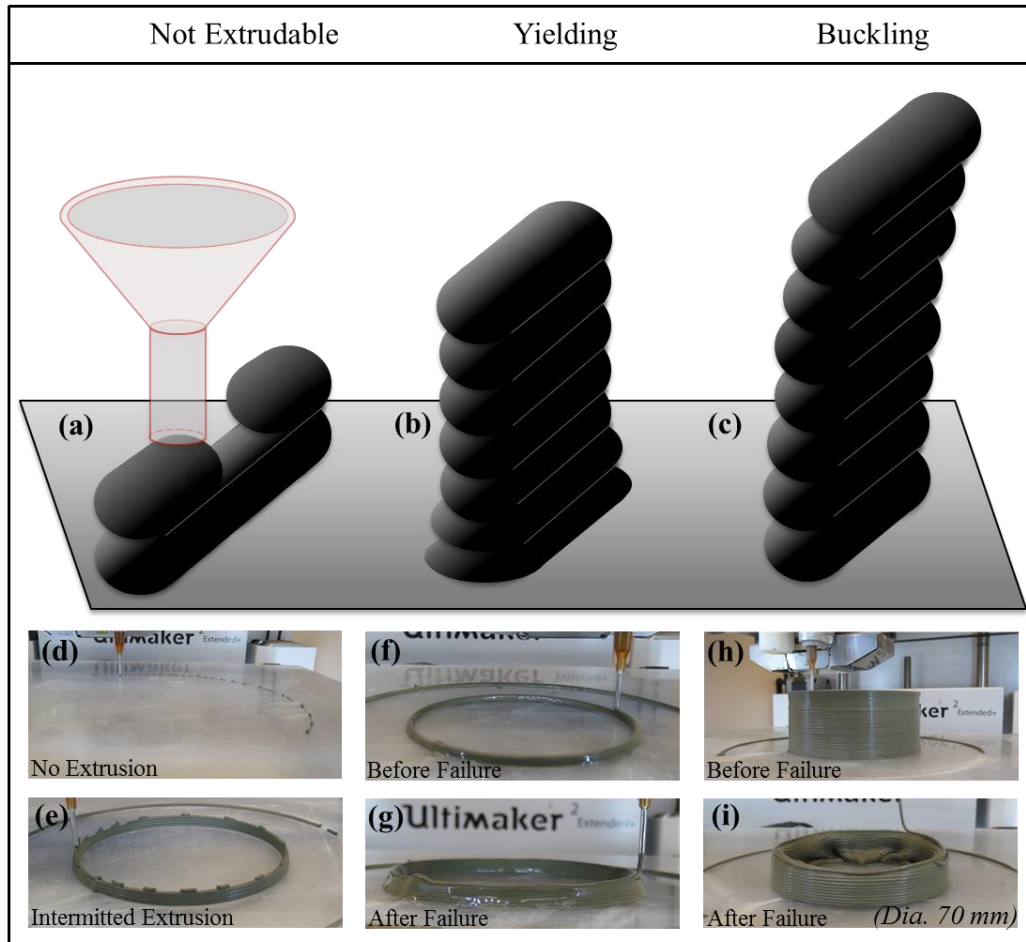


Figure 2.1. (a-c) Schematics of three main printability phenomena during 3D-printing of cement-based materials: inability to extrude, two failure mechanisms, yielding and buckling and (d-i) Representative images of these three phenomena in 3D-printed cement paste elements with various, materials composition.

An isosceles triangle was introduced as a support structure to be used for assessment of early-age deformation of cement pastes upon deposition. Individual cement paste filaments were printed over a wide range of span lengths provided by the isosceles triangle.

## 2.2 Materials and methods

### 2.2.1 Materials composition

Cement paste compositions shown in **Table 1** were used to provide a broad range of rheological properties and buildability and allow for probing the rheology-buildability relationship. Plain pastes with solid contents between 47% -56% corresponding to a water/cement (w/c) ratio of 0.35-0.25 were used to investigate a broad range of extrudability and buildability. Pastes with high-range-water-reducing-admixture (HRWRA) were used as a means to increase the solid loading and potentially improving buildability. Hydrophilic polymeric viscosity-modifying-admixture (VMA) was used to improve materials consistency and resistance to bleeding during extrusion. Pastes with a combination of HRWRA and VMA were used to increase the solid content and improve materials' consistency and potentially increase buildability. Type I cement (ASTM C150), deionized water, MasterGlenium 7700 HRWRA, and MasterMatrix 362 VMA were used. Both chemical admixtures met the requirements of the ASTM C494. A mixing procedure using a Twister Evolution Venturi vacuum mixer was previously developed by authors and was used in this work [22].

Table 2.1. Cement paste materials composition containing a ranges of chemical high-range-water-reducing admixture (HRWRA) and viscosity-modifying-admixture (VMA).

<b>Materials Composition</b>	<b>Solid Loading (%)</b>	<b>Water/Cement Ratio</b>	<b>HRWRA (%)</b>	<b>VMA (%)</b>
Plain Paste	47,51,53,56	0.25, 0.275, 0.30. 0.35	-	-
Plain Paste+HRWRA	53, 55	0.25, 0.275	0.15-0.25	-
Plain Paste+VMA	53	0.275	-	0.05-0.2
Plain Paste+HRWRA+VMA	53-55	0.25, 0.275	0.05-0.25	0.05

### 2.2.2 Rheological characterization

A Malvern Bohlin Gemini HR rheometer, equipped with 40 mm serrated parallel plates were used for oscillatory shear rheometry tests. Serrated surfaces were used to minimize the slippage during the tests. A gap of 0.6 mm was used. A solvent trap was used to avoid water evaporation during the test. Oscillatory shear rheometry protocols have been commonly used for studying viscoelastic properties of cement paste [23–26]. The first step in performing oscillatory shear rheometry tests is to find the linear viscoelastic region (LVR), where  $G'$  and  $G''$  are independent of applied frequency and strain [27]. A frequency sweep is commonly used to find LVR [23]. The LVR was determined by conducting a frequency sweep from 0.1-100 Hz. The temperature was kept constant at  $25 \pm 0.2$  °C. Frequency of 1 Hz has been commonly used for fresh cement paste oscillatory strain or stress sweep tests [23–28] and was found to be within LVR here as well. A stress-controlled oscillatory shear stress sweep from 0.01 to 3000 Pa at a frequency of 1 Hz test beginning within the linear viscoelastic region (LVR) and continued to non-linear LVR was used to characterize viscoelastic properties including shear modulus ( $G$ ), complex shear modulus ( $G^*$ ), storage modulus ( $G'$ ), and loss modulus ( $G''$ ) and flow properties including yield stress ( $\sigma_{yield}$ ), yield strain ( $\gamma_{yield}$ ), and complex viscosity ( $\eta^*$ ). The samples were pre-sheared before each test at 50 1/s for 30 s followed by a 30 s recovery. The LVR is bound by critical strain and critical frequency [27–29].  $G$  was characterized using a first-order fit to the linear portion of the stress-strain using a zero intercept.  $G^*$ ,  $G'$  and  $G''$  were characterized as constants within the LVR [29].  $\sigma_{yield}$  and  $\eta^*$  were taken at the strain in which crossover of  $G'$  and  $G''$  (i.e., at  $\gamma_{yield}$ ) [30]. All rheological properties were determined from the average value of at least two separate measurements using a freshly mixed paste. Although cement-based materials' rheological properties are time-dependent [31,32], all rheological properties were characterized between 15-20 minutes of mixing water and cement (during the dormant period of cement hydration) in which the rheological properties are nearly constant, and their time-dependency is minimized.

### 2.2.3 Assessment of buildability

A 3D printer capable of printing cement paste via layer-by-layer extrusion with two separate units (**Figure 2.2a**) was previously established by the authors and was used in this work [22]. Hollow cylinders with a diameter of 70 mm and a wall thickness of 1.63 mm were fabricated using

the paste compositions described in **Table 2.1**, as demonstrated in **Figure 2.2b**. A printing speed of 750 mm per minute and a layer height of 1 mm was used for slicing to print the hollow cylinders. The extrusion started 5 minutes after mixing water and cement. Buildable elements were continuously printed until either yielding or buckling occurred. Buildability was defined as the height of successfully printed element before the element yields or buckles. A material handling procedure for charging the extrusion system with fresh cement pastes was previously developed by authors and was used in this work [33]. Similarly, a commercially available slicer (Simplify3D) was used to generate the G-code commands. A slicing procedure was previously established by the authors and was used in this work [33].

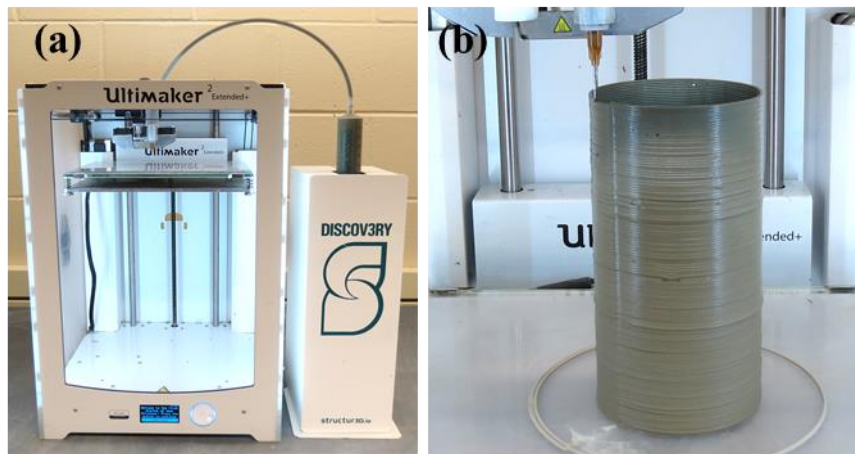


Figure 2.2. (a) 3D-printer setup for cement-based materials using a gantry system (Ultimaker 2 Extended+) and stepper motor-based extrusion (Discov3ry) system for 3D-printing of (b) A hollow cylinders geometry with a diameter of 70 mm and thickness of 1.63 mm used for assessment of buildability.

#### 2.2.4 Assessment of downward deformation via isosceles triangle

An isosceles triangle (**Figure 2.3a**) was designed and used as a support structure for the assessment of the downward deformation of cement paste filaments [8]. A photopolymer resin material and the Formlabs Form 3 Stereolithography (SLA) 3D-printer (**Figure 2.3b**) was used to fabricate the triangle. The triangle was then rinsed and cured in the post-curing station using UV light at 60 °C for 30 minutes (**Figure 2.3c**). Individual cement paste filaments with selected materials compositions described in **Table 2.1** were 3D-printed over varied span lengths (**Figure 2.3d**). The hardening of 3D-printed cement paste over the isosceles triangle, the object was rapidly

scanned using a micro-CT, as demonstrated in the rendering of **Figure 2.3f**. The downward deformation of the individual cement paste filaments ( $\delta$ ) over each span was measured.

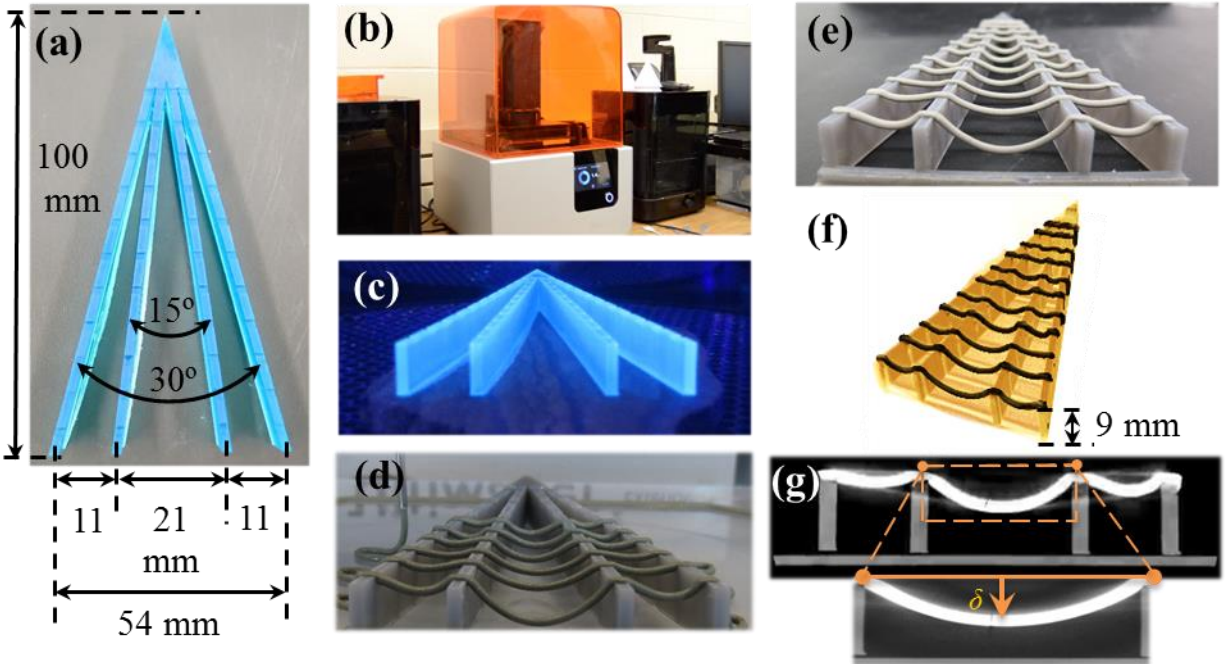


Figure 2.3. (a) Design, (b,c) Stereolithography, and curing of 3D-printing of an isosceles triangle used as a platform for (d) 3D-printing cement paste over varied span length, followed by (e) Hardening of cement paste, (f) CT-scan of the hardened cement paste, and (g) Quantification of deflection ( $\delta$ ) of printed individual cement paste filaments with respect to the horizontal line.

## 2.3 Results and Discussion

### 2.3.1 Buildability

Three main phenomena occur during extrusion and 3D-printing. All pastes except for the plain paste with a solid loading of 56% shown in **Figure 2.4a** were extrudable, mostly due to high solid content and processing limitations such as insufficient extrusion pressure. Upon successful extrusion, two failure mechanisms of yielding and buckling were observed in the hollow cylinder element and caused extreme deformation and loss of shape stability. The elements that failed via yielding mechanism deformed at the bottom layers and typically had a small buildability of less than 10 mm, such as those with solid contents above below 51% (**Figure 2.3a**). The yielding is most likely due to low solid content and insufficient build-up of the fresh microstructure that is inadequate to resist the deformation and self-weight of the layers [10]. On the other hand, the

elements that failed via the buckling mechanism achieved a buildability as high as 142 mm, as demonstrated in **Figure 2.4a,b,c**. Buckling-dominated failure of hollow cylinders was observed through deformation of filaments on the top layers in a rapid and inward folding, leading to collapse of the elements from the top to the bottom. The buckling can be attributed to accumulation of geometrical imperfections and deviation of filaments with respect to one another [34]. The range of buildability of this failure mechanism was quite large and had little to do with the way the elements buckled but rather to do with the materials design, composition, and rheological properties.

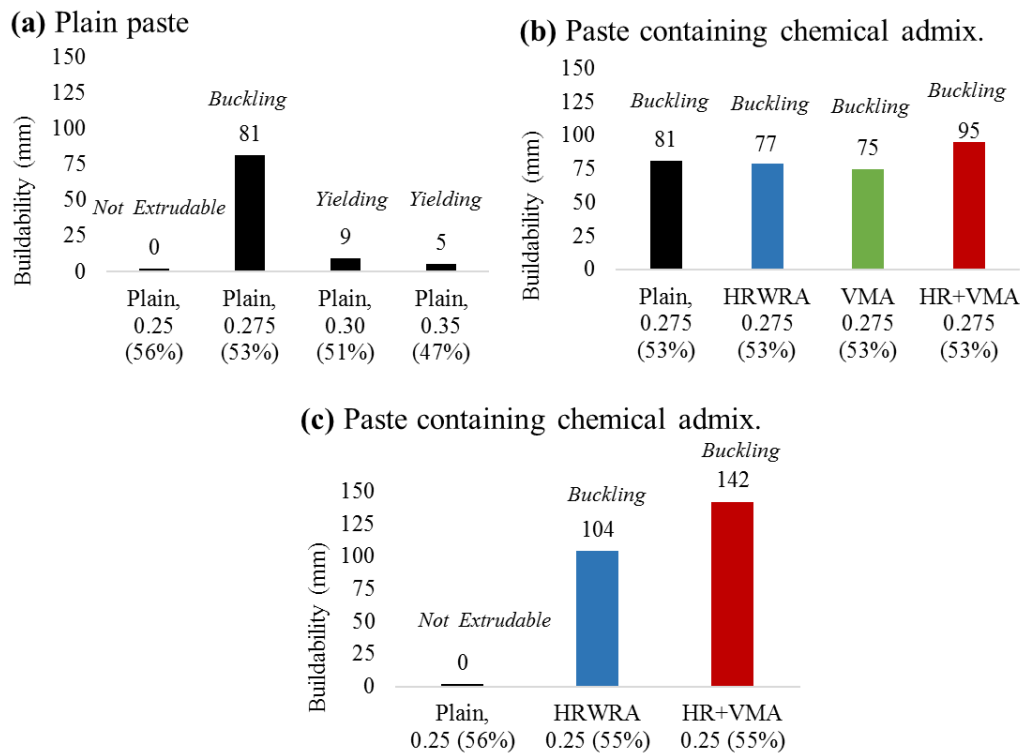


Figure 2.4. Assessment of buildability of hollow cylinders based on the number of successfully printed layers (height of ~ 1 mm per layer) in various materials composition: (a) Plain paste, (b) Paste with chemical admixtures at 53% solid loading, and (c) Paste with chemical admixture at ~55% solid loading

Plain cement paste with solid loading of 53% was found to provide a good buildability of 81 mm, where a solid loading of 56% was not found extrudable (**Figure 2.3a**). These two solid loadings were selected and used as reference data points to achieve extrudability and to probe the rheology-buildability via the use of a wide range of paste compositions containing chemical admixtures (**Figure 2.3b**). HRWRA decreases buildability at 53% solid content (**Figure 2.4b**),

and it facilitates to make a previously unextrudable plain paste, extrudable and highly buildable at 55% solid content (**Figure 2.4c**). Counter-intuitively, VMA was found to reduce buildability (**Figure 2.4b**). Additionally, when VMA was used in conjunction with HRWRA, the buildability was increased in both levels of 53% and 55% solid content (**Figure 2.4b**), indicating a different working mechanism than when only VMA or HRWRA were used. The results allude to a relationship between materials composition (and their corresponding rheological properties) and buildability. Therefore, one can hypothesize that one or more rheological properties of the pastes are correlated with the buildability of the hollow cylinders that fail via a buckling mechanism.

### 2.3.2 Prediction of Buildability

Euler's buckling theory [35,36] was used to predict buildability from elastic modulus ( $E$ ) (**Eq. 1**). Euler's equation is commonly used for prediction of the buckling load of a slender element, granted the member remains fully elastic. Therefore, several assumptions were made using **Eq. 1**, including: (a) behavior is purely elastic, and (b) cross-section of the hollow element is constant.

$$P_e = \frac{\pi^2 EI}{(KL)^2} \quad (\text{Eq. 1})$$

$P_e$  is the Euler's buckling load,  $I$  is the moment of inertia of the cross-section,  $L$  is the unbraced length of the column, and  $K$  is the effective length factor to account for end conditions of the element. Effective length is the distance between two points of inflection upon buckling. Assuming end conditions of rotation fixed and translation fixed bottom and rotation free and translation free top of the hollow element  $K = 2$  was used to take into account the effective length [36].

Rewriting Euler's equation for the length of the element gives:

$$\text{Buildability } (L) = \sqrt[3]{\frac{\pi^2 EI}{K^2(\rho \cdot A \cdot g)}} \quad (\text{Eq. 2})$$

$\rho$  is the density of fresh cement paste,  $A$  is the area of the element, and  $g$  is gravity constant. The elastic modulus ( $E$ ) can be calculated from shear modulus ( $G$ ) using the following relationship:

$$E = 2G(1 + \nu) \quad (\text{Eq. 3})$$

$\nu$  is the Poisson's ratio of cement paste. Measured shear modulus ( $G$ ) was used to calculate elastic modulus ( $E$ ) of the pastes using the assumed Poisson's ratio ( $\nu$ ) value of the 0.5 for fresh cement paste [37].

### 2.3.3 Buildability-Rheological Properties Relationship

The buildability versus rheological properties of all pastes is demonstrated in **Figure 2.5a-g**. The data points with the three categories of none-extrudable paste, the yielding failure mechanism, and buckling failure mechanism were demonstrated by the orange, green, and blue ovals. The correlation between the buildability of elements failed via buckling, and the rheological properties were investigated. Buildability was found to be the more correlated with variation of certain shear moduli of the fresh cement paste ( $G$ ,  $G^*$ , and  $G'$ ) obtained from the oscillatory shear stress sweep tests than other rheological properties ( $G''$ , yield stress, yield strain, and complex viscosity). This correlation is represented by higher  $R^2$  values between  $G$ ,  $G^*$ , and  $G'$  and buildability ( $R^2 = 0.63, 0.57, \text{ and } 0.56$ , respectively), compared to the  $R^2$  values between  $G''$ ,  $\sigma_{yield}$ ,  $\gamma_{yield}$ ,  $\eta^*$  and buildability ( $R^2 = 0.24, 0.05, 0.07, \text{ and } 0.10$  respectively). It can be postulated that the higher correlation between buildability and  $G$ ,  $G^*$ , and  $G''$  compared to  $G''$ ,  $\sigma_{yield}$ ,  $\gamma_{yield}$ ,  $\eta^*$  lies within the two reasons:

- (i) In theory, buckling is not dominated by materials' strength properties (i.e., yield stress and viscosity) but rather by materials' stiffness (i.e., elastic modulus  $E$ ) as shown **Eq. 1**. Shear modulus ( $G$ ) is theoretically related to elastic modulus (as shown in **Eq. 3**); therefore, in principle, buildability can be expected to show a correlation to shear modulus, granted the buckling to be the physical phenomenon by which the hollow cylinder fails. Complex shear modulus ( $G^*$ ) and elastic component of viscoelastic fresh cement paste (storage modulus  $G'$ ) are related to  $G$ , and therefore, to  $E$ . Thus, they are also expected to demonstrate a correlation.
- (ii) Hollow cylinders are static during printing (until buckle at some height) and are loaded quasi- statically in a layer-by-layer manner under their weight (without nozzle pushing on the layers underneath). Due to the quasi-static nature of the buildability test and as proved by observations, the axial loads resulting in potential deformations due to self-weight do not cause any visible macroscopic flow in the individual layers. Therefore, in theory, it is not expected that the materials flow properties including yield stress ( $\sigma_{yield}$ ) and viscosity

( $\eta^*$ ), the strain at which yield occurs ( $\gamma_{yield}$ ), or the viscous component of viscoelastic fresh cement paste (loss modulus  $G''$ ) to demonstrate any correlation with buildability.

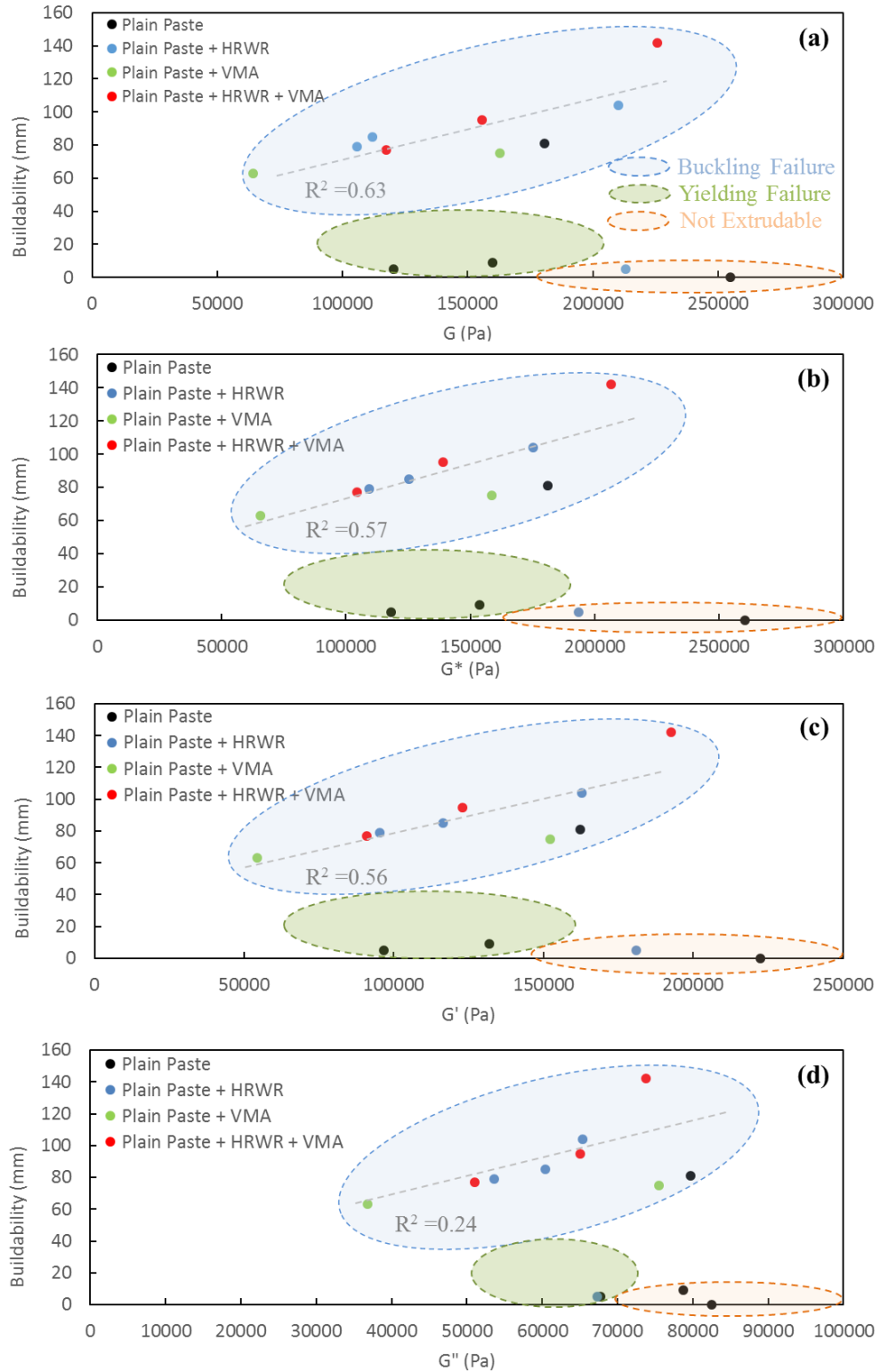
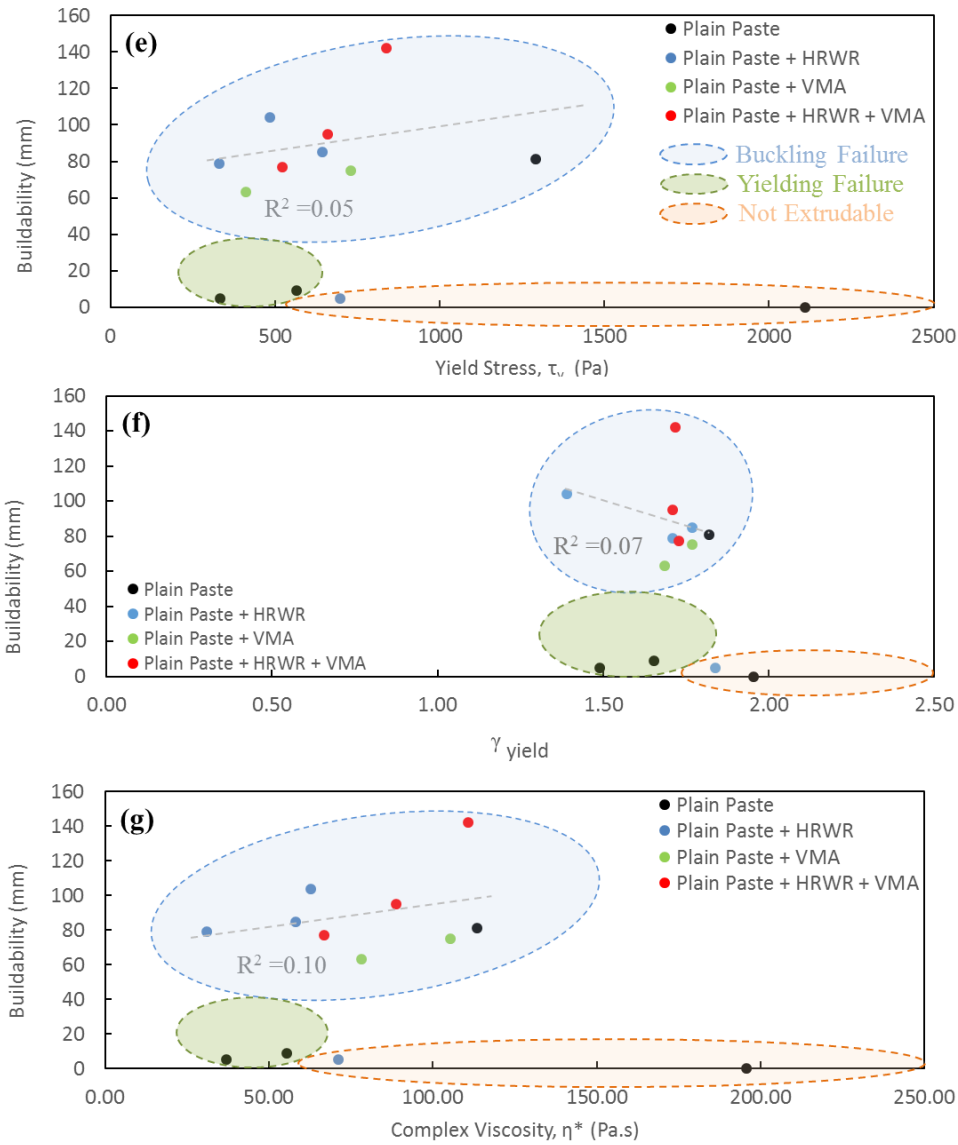


Figure 2.5. Correlation between buildability (number of printed layers) and rheological properties: (a) Shear Modulus, G, (b) Complex shear modulus,  $G^*$ , (c) Storage modulus,  $G'$ , (d) Loss modulus,  $G''$ , (e) Yield stress,  $\tau_y$ , (f) Yield strain,  $\gamma_{critical}$ , (g) Complex viscosity  $\eta^*$ .

Figure 2.5 continued



Moreover, the buildability was more precisely correlated with the shear modulus  $G$  ( $R^2 = 0.63$ ), compared to complex shear modulus  $G^*$  ( $R^2 = 0.57$ ) and storage modulus  $G'$  ( $R^2 = 0.57$ ). A possible reason is the direct and physically correct relationship between  $G$  (slope of stress-strain) and  $E$  as shown in **Eq. 3**, compared to the indirect relationship between  $G^*$  and  $G'$  and  $E$  (i.e., calculated based on materials stress stimulus and fitting a mathematical model for strain response). In summary, the correlations reported in **Figure 2.5a-g** provides insight that some shear moduli (specifically  $G$ ,  $G^*$ , and  $G'$ ) are more important than others for controlling the buildability of the thin hollow cylinder elements. In particular, the buildability correlated to shear modulus  $G$ . It also

infers that materials rheological properties such as yield stress are most likely essential at earlier layers/stages of printing where yielding failure has the probability/chance of occurrence. Such hypothesis have been evaluated by other researchers have resulted in similar understanding that gravity-induced stresses surpass the materials yield stress at a given time, the element yields at lower layers [38–41].

### 2.3.4 Buildability, Elastic Modulus, and Prediction of Buildability

From the discussion of measured shear moduli-buildability relationship (**Figure 2.5**) and the theoretical relationship between  $E$  and buildability, one can argue that buildability can be predicted using  $E$  that is calculated from measured shear moduli. The accuracy of such prediction then becomes critical. Prediction of buildability from Euler's theory was proceeded here using the elastic moduli of all the pastes ( $E$ ,  $E^*$ ,  $E'$ ) calculated from the measured shear moduli ( $G$ ,  $G^*$ ,  $G'$ ) using **Eq. 3**. The Euler's buckling theory was rewritten for  $L$  per **Eq. 2** for prediction of buildability. The predicted buildability  $L$  was plotted versus  $E$ ,  $E^*$ ,  $E'$  for two different effective length factor  $K$  (**Figure 2.6.a**). It was found that Euler's theory (with  $K = 2$ ) overestimates the buildability by 104% to 210% using  $E$ , 101% to 206% using  $E^*$ , and 93% to 194% using  $E'$ . One caveat is that  $K$  depends on the end constraints as it influences the effective length, as discussed before. An element with free translation and rotation movement at the top, similar to that of our hollow cylinder, has an effective length of 2 ( $K = 2$ ) compared to an element with fixed translation and rotation ( $K = 1$ ). In the case of our hollow cylinder, assuming a constrained top ( $K = 1$ ) is inaccurate and led to even a higher overestimation buildability compared to when free translation and rotation was used ( $K = 2$ ) (**Figure 2.6.a**).

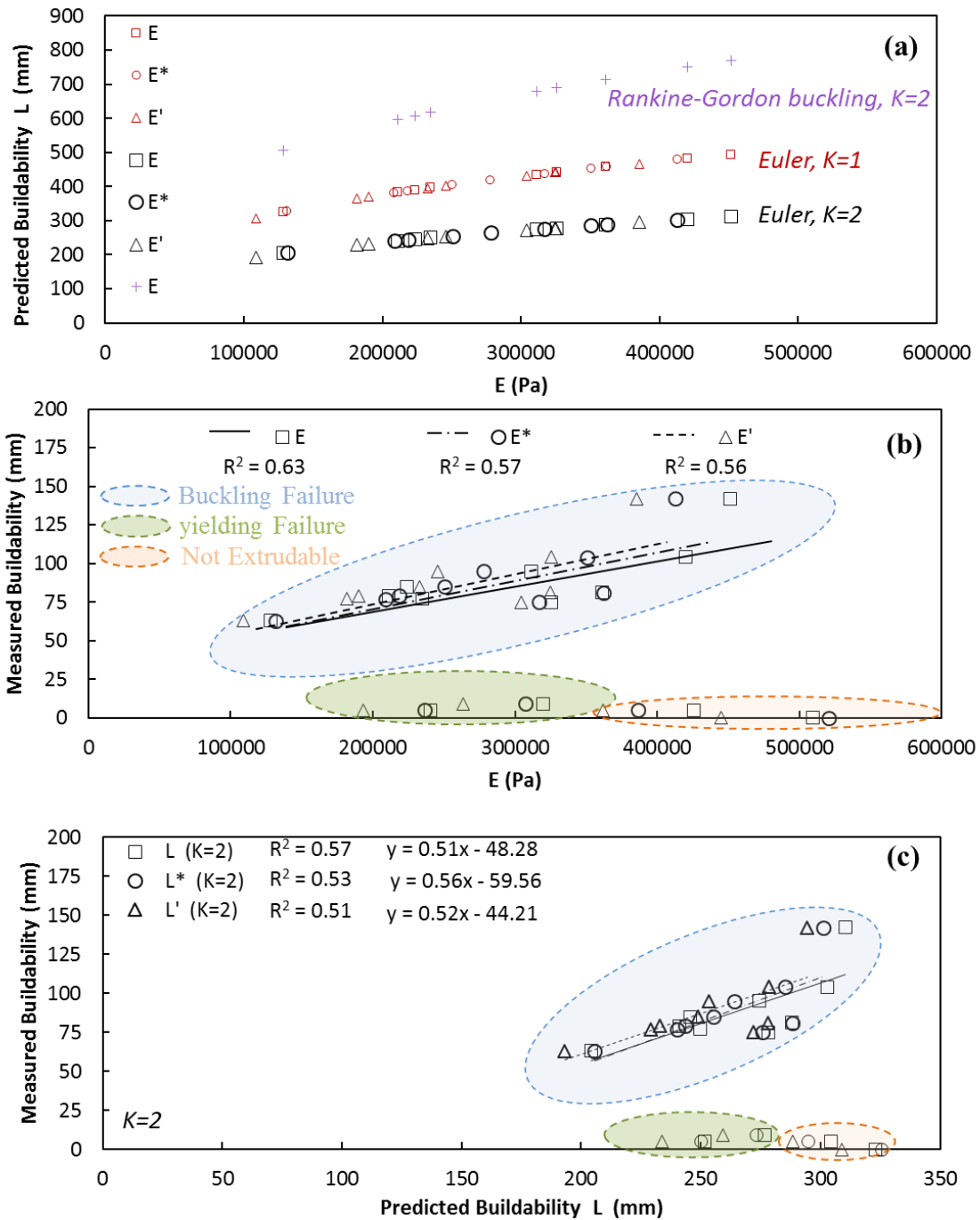


Figure 2.6. (a) Modulus of elasticity,  $E$  vs. predicted buildability,  $L$ , (b) Modulus of elasticity,  $E$  vs. measured buildability, (c) Predicted buildability,  $L$  vs. measured buildability.

It must be noted that several other theoretical or semi-empirical frameworks for prediction of critical load of slender elements exist and can be used for prediction of buildability. However, their use can only result in proper predictions if the assumptions for their use can be realistically

applied to the problem of predicting the buildability of 3D-printed viscoelastic materials. Here, Rankine-Gordon semi-empirical buckling equation [42] that extends the Euler's equation to consider crushing strength of the material, in addition to the elastic modulus and geometry as follow:

$$P_R = \frac{\sigma_{yc}A}{1 + a(L_0/r)^2} \quad (Eq. 4)$$

$L_0$  is the effective length ( $L_0 = KL = 2L$ ),  $A$  is the cross-sectional area,  $r$  is the radius of gyration, and  $a$  is the denominator constant:

$$a = \frac{\sigma_{yc}}{\pi^2 E} \quad (Eq. 5)$$

Yield strength  $\sigma_{yield}$  was used as crushing strength  $\sigma_{yc}$  and  $E$  calculated from  $G$  was used in rewriting Rankine-Gordon equation and solving a 3<sup>rd</sup> order equation for predicting buildability ( $L$ ) where self-weight becomes critical. The use of the Rankine-Gordon equation resulted in an overestimation of buildability higher than either of the two Euler's estimations, as demonstrated in **Figure 2.6.a**.

As **Figure 2.6.a** demonstrated the predicted buildability and elastic moduli ( $E$ ,  $E^*$ ,  $E'$ ) relationship, one can also look into the relationship between measured buildability and elastic moduli ( $E$ ,  $E^*$ ,  $E'$ ). It is expected that buildability demonstrates a stronger correlation with  $E$  compared to the other two elastic moduli ( $E^*$  and  $E'$ ). This relationship was plotted and examined by comparing coefficients of determination. Similar trends between buildability and elastic moduli to those observed between buildability and shear moduli (**Figure 2.5a,b,c**) were found. As expected, buildability was more precisely correlated with the  $E$  ( $R^2 = 0.63$ ), compared to  $E^*$  ( $R^2 = 0.57$ ) and  $E'$  ( $R^2 = 0.56$ ) as demonstrated in **Figure 2.6.b**. The reason again has to do with the direct relationship between  $E$  calculated from **Eq. 3** and  $G$  (slope of stress-strain), compared to the indirect relationship between  $E^*$  and  $E'$  with  $G$ .

More importantly, the relationship between the predicted buildability ( $L$ ) at its best estimation (using Euler, with  $K = 2$ ) and the measured buildability for all of the pastes with buckling failure mechanism was plotted in **Figure 2.6c**. The buildability ( $L$ ,  $L^*$ ,  $L'$ ) was predicted using the elastic moduli ( $E$ ,  $E^*$ ,  $E'$ ) and were estimated close to one another.  $E$  was found to be a more precise predictor of buildability compared to the other two moduli ( $E^*$ ,  $E'$ ). None of the three elastic moduli very accurate predictors of buildability. Overall, several reasons for the overestimation of buildability using Euler's theory can be conceived:

- (i) *Assumption of perfect straightness*: Euler's theory assumes an ideal geometry (i.e., perfectly vertical element) with no initial imperfection [34]. Elements are rarely perfectly straight in reality. Layer-by-layer 3D-printing results in ample fabrication imperfections in the orders of 100s of microns, such as misalignment of filaments/layers with respect to one another (deviations enhanced by processing effects such as vibration and inertia effects) another to that results in accumulation of geometrical imperfections as the element is built up.
- (ii) *Assumption of perfect linear elasticity*: It must also be noted that Euler's theory was applied, assuming the elements behave within their elastic region [43]. This assumption needs further investigation and verification. Although no visible macroscopic 'flow' was observed in the printed layers, that does not assure us of a perfectly linear elastic response before buckling. Early-age deformations upon materials deposition and rate of building up the element can also reduce the elastic modulus of fresh paste and cause the hollow cylinder to behave plastically. The isosceles triangle test was developed to separately look into early-age deformation of individual cement paste filaments [3,8].

In addition, due to difficulties in obtaining close-form solutions for the buildability of viscoelastic materials partly due to potential inelastic behavior, numerical methods can be efficiently used to explore the influence of processing parameters (rate of building up, nozzle size) and effects (vibration, inertia) on buildability.

### **2.3.5 Isosceles triangle deformation test results**

The isosceles triangle test was developed to assess of deformation of individual filaments of selected pastes over varied span lengths and obtain insight about the role of materials composition. The mid-span deflection was used as a measure of deformation. The mid-span deflection (maximum deflection) measured upon hardening form micro-CT was plotted versus the span length (**Figure 2.7**). A second-order polynomial equation was fit to the experimental data for more clear visualization. The range of deformations, as presented in **Figure 2.7** are quite varied and dependent upon materials composition (i.e., solid loading and chemical admixtures).

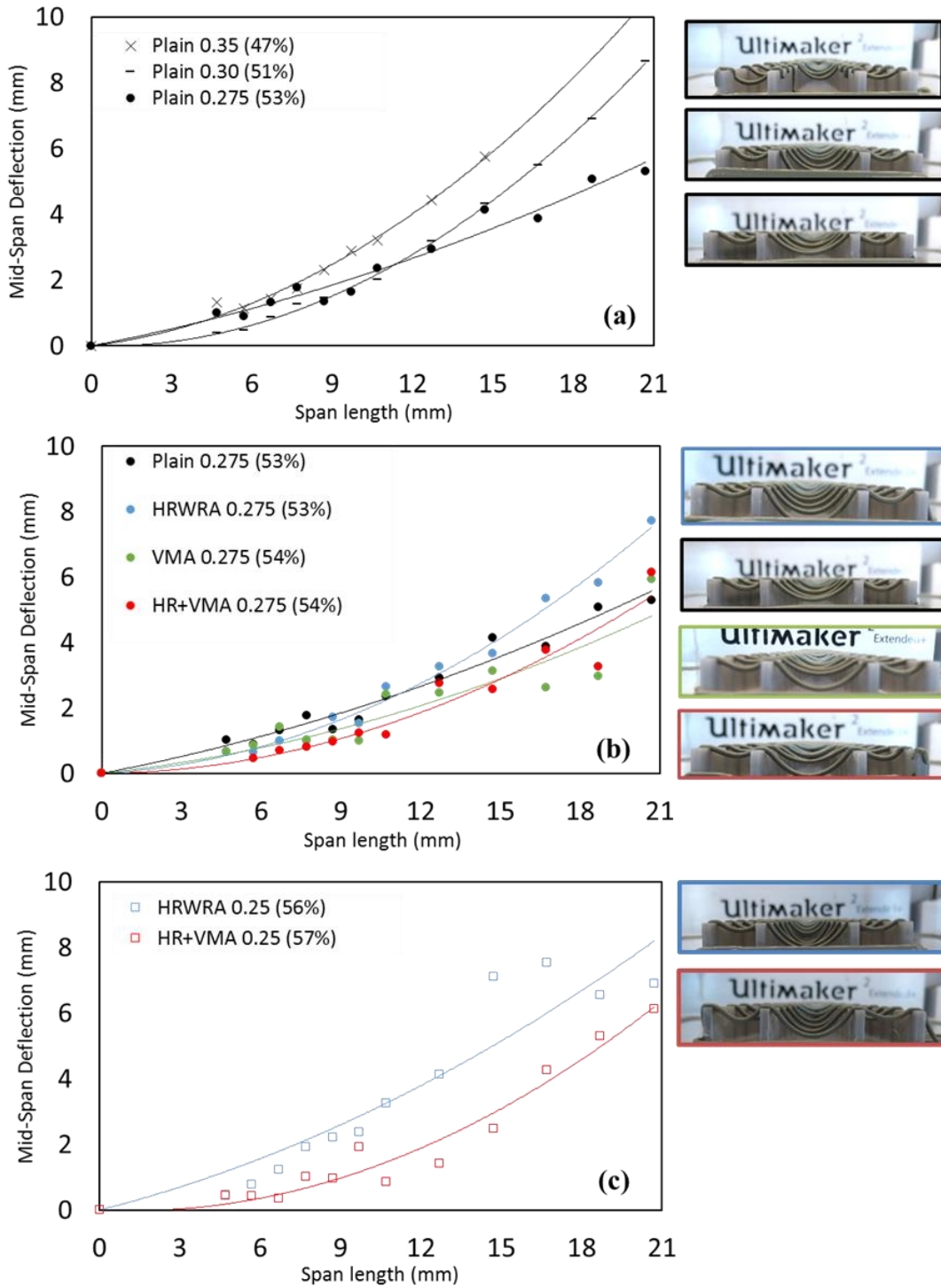


Figure 2.7. Mid-span deflection vs. span length of individual cement paste filaments with various materials compositions: (a) Plain paste with W/C ratio of 0.35, 0.3, and 0.275, (b) Paste with constant W/C ratio of 0.275 and various chemical admixtures, and (c) Paste with constant W/C ratio of 0.25 and various chemical admixtures.

The effects of solid loading and chemical admixtures can be observed in **Figure 2.7.a,b,c.**, the higher the solid content, the lower the mid-span deflection (**Figure 2.7.a**). For nearly constant solid loading of 53%-54% as reference (**Figure 2.7.b**), the use of HRWA increases mid-span deflection at spans longer than 12 mm, whereas the use of VMA decreases mid-span deformation. The combined use of HRWA and VMA also decreases the mid-span deflection compared to the reference plain paste, rather slightly, compared to the paste with VMA, and rather drastically compared to the paste with HRWA (**Figure 7.b**). At a solid loading of 56%-57%, the data demonstrate the same effects in the use of combined HRWA and VMA, in the way that it highly reduces mid-span deflection compared to the paste with HRWA. The trend in which the combined use of VMA and HRWA reduce the early-age deformation over isosceles triangle test is aligned with the buildability assessment and indicating a different working mechanism than when only VMA or HRWA were used. Several mechanisms for the role of HRWA [44] and polymeric VMA [45,46] are discussed by researchers. However, those mechanisms can be altered at low solid contents such as pastes used in this study or by printing process. The reference and the past with VMA in this solid content were not extrudable.

In summary, the isosceles triangle was used to examine the deformation of individual filament (or their ability to resist deformation under self-weight) and the relationship between this deformation and materials composition. The self-weight effects of the test can be used to investigate the relationship between structural built-up of various materials composition and the early-age deformations at the initial stages of hydration. The test can also be used to study the working mechanisms of chemical admixture and provides a basis for precise fine-tuning of the materials design as required. However, further research is needed to probe the deformation at the filament scale over the varied span length and its correlation with the buildability at the element scale. Similarly, treatment of the filaments as elastic beams is possible for the extraction of  $E$  and prediction of buildability. However, such an approach requires further verification of elasticity and alteration of the test (such as retaining a perfectly horizontal filament as the initial condition prior to deformation under self-weight).

## 2.4 Conclusion

In this chapter, the correlation between a wide range of rheological properties of cement pastes and the buildability of hollow elements fabricated with those inks and failed via buckling

was investigated. It was found that certain shear moduli of the fresh pastes ( $G$ ,  $G^*$ , and  $G'$ ) obtained from oscillatory shear stress sweep tests (within the first 30 minutes of hydration) correlate well with the buildability of hollow elements more than other rheological properties ( $G''$ , yield stress, yield strain, and complex viscosity). Moreover, the shear modulus ( $G$ ) demonstrated a higher correlation to buildability than the complex shear modulus ( $G^*$ ) and the storage modulus ( $G'$ ). Most importantly, the buildability-rheology investigation provides evidence that certain shear moduli ( $G$ ,  $G^*$ , and  $G'$ ) of fresh cement paste, specifically the shear modulus  $G$ , is the most relevant rheological property if buckling is the dominant failure mechanism of the 3D-printed element. Therefore, the shear modulus  $G$ , then can be used to tailor the materials design for achieving shape stability. The rheology-buildability relationships also infer that materials rheological properties such as yield stress are only important at earlier layers and stages of the printing process where yielding failure has a probability of occurrence (depending on the loading/printing rate). It must be noted that extrudability and buildability are also dependent upon printing processes and parameters such as extrusion pressure, printing speed, nozzle size, which all affect the ‘flow’ of the materials in the extrusion process.

Three properties obtained from oscillatory shear stress sweep can be used to calculate corresponding elastic moduli ( $E$ ,  $E^*$ ,  $E'$ ) to predict buildability. It was found that using calculated elastic moduli, Euler's theory can be used to predict buildability. However, Euler's theory at best overestimates the buildability by 92% to 184%, mainly due to assuming ideal geometry with no initial or printing imperfection and linear elasticity. These two simplifications can result in the overestimation in the prediction of buildability.

An isosceles triangle was introduced as a support structure and was used for assessment of early-age deformation of individual cement paste filaments over varied span lengths. The results provide insight into the role of the solid content and working mechanisms of chemical admixtures and fine-tuning materials' design and early-age deformations. Therefore, it can be used as a new reference testing method for assessment materials resistance to deformations.

## 2.5 Appendix

**Figure 2.S1** further describes the correlation between solid loading and all measured rheological properties and demonstrates a threshold for extrudability and yielding. **Figure 2.S2** describes the correlation between solid loading and buildability. A similar threshold observed in **Figure 2.S1** is

also evident here, mainly due to the correlation between shear moduli and buildability. These two supplementary figures provide insight for the design of cement paste composition.

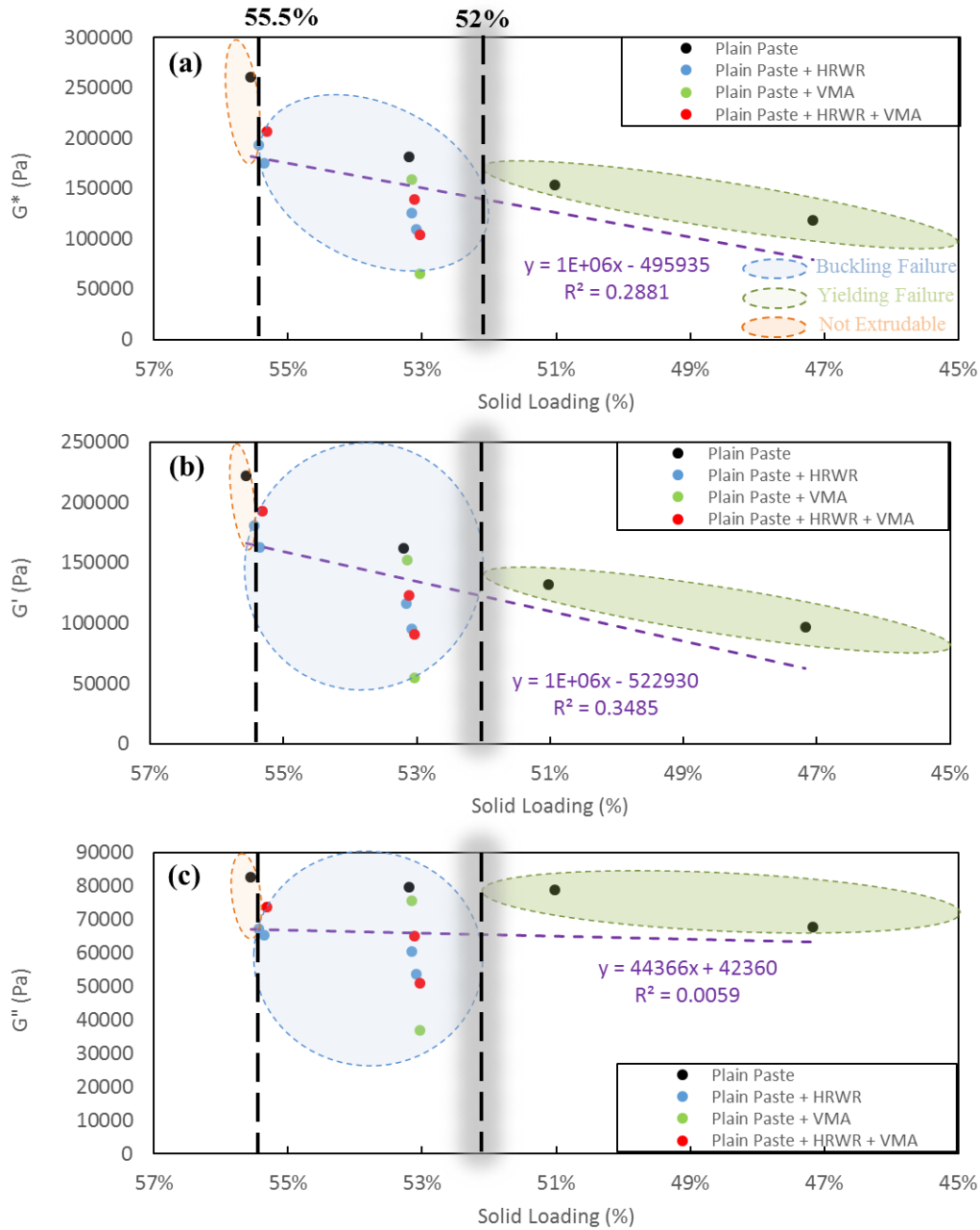
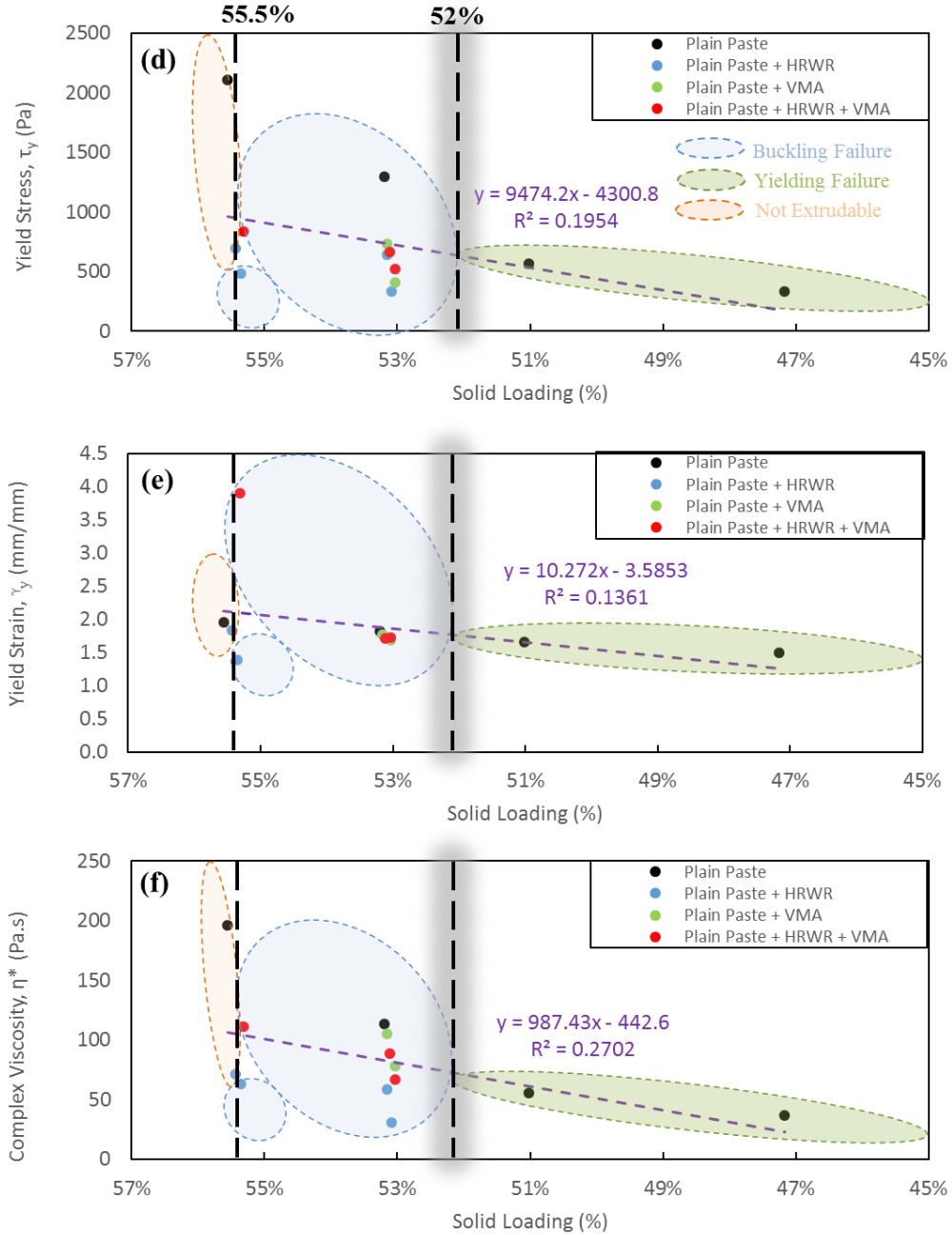


Figure 2.S1. Correlation between solid loading (%) and rheological properties: (a) Complex shear modulus,  $G^*$ , (b) Storage modulus  $G'$ , (c) Loss modulus,  $G''$ , (d) yield stress,  $\tau_y$ , (e) yield strain,  $\gamma_{critical}$ , (f) complex viscosity  $\eta^*$ .

Figure 2.S1. continued



## 2.6 Acknowledgement

The Type I cement used in this work was donated by Buzzi Unicem, USA, and the chemical admixtures were donated by BASF, USA. I gratefully acknowledge the generous support of this research by the National Science Foundation (CMMI Grant 1562927) as well as Purdue College

of Engineering. I acknowledge the use of the Zeiss Xradia 510 Versa 3D X-Ray Microscope Facility in the Department of Physics and Astronomy that was supported by the Executive Vice President for Research and Partnerships, Major Multi-User Equipment Program 2017 at Purdue University.

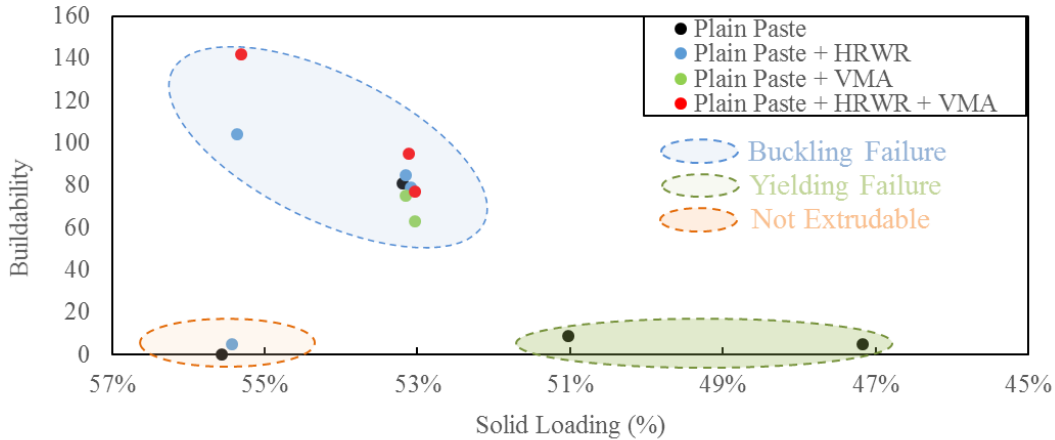


Figure 2.S2. Correlation between solid loading (%) measured buildability.

## 2.7 References

- [1] R. J. M. Wolfs, A.S.J. Suiker, Structural failure during extrusion-based 3D printing processes, (2019) 565–584. doi:10.1007/s00170-019-03844-6.
- [2] A.M. Barki, L. Bocquet, A. Stevenson, Linking Rheology and Printability for Dense and Strong Ceramics by Direct Ink Writing, (2017) 1–10. doi:10.1038/s41598-017-06115-0.
- [3] J.A. Lewis, Direct-write assembly of ceramics from colloidal inks, *Curr. Opin. Solid State Mater. Sci.* 6 (2002) 245–250. doi:10.1016/S1359-0286(02)00031-1.
- [4] A. Paolini, S. Kollmannsberger, E. Rank, Additive manufacturing in construction : A review on processes , applications , and digital planning methods, *Addit. Manuf.* 30 (2019) 100894. doi:10.1016/j.addma.2019.100894.
- [5] L. Rueschhoff, W. Costakis, M. Michie, J. Youngblood, R. Trice, Additive Manufacturing of Dense Ceramic Parts via Direct Ink Writing of Aqueous Alumina Suspensions, *Int. J. Appl. Ceram. Technol.* 13 (2016) 821–830. doi:10.1111/ijac.12557.

- [6] W.J. Costakis, L.M. Rueschhoff, A.I. Diaz-Cano, J.P. Youngblood, R.W. Trice, Additive manufacturing of boron carbide via continuous filament direct ink writing of aqueous ceramic suspensions, *J. Eur. Ceram. Soc.* 36 (2016) 3249–3256. doi:10.1016/j.jeurceramsoc.2016.06.002.
- [7] K.G. Kuder, S.P. Shah, *Rheology of Extruded Cement-Based Materials*, (2008).
- [8] J.E. Smay, J. Cesarano, J.A. Lewis, Colloidal inks for directed assembly of 3-D periodic structures, *Langmuir*. 18 (2002) 5429–5437. doi:10.1021/la0257135.
- [9] A.S.J. Suiker, *International Journal of Mechanical Sciences Mechanical performance of wall structures in 3D printing processes : Theory , design tools and experiments*, *Int. J. Mech. Sci.* 137 (2018) 145–170. doi:10.1016/j.ijmecsci.2018.01.010.
- [10] N. Roussel, Rheological requirements for printable concretes, *Cem. Concr. Res.* 112 (2018) 76–85. doi:10.1016/j.cemconres.2018.04.005.
- [11] R.J.M. Wolfs, F.P. Bos, T.A.M. Salet, Early age mechanical behaviour of 3D printed concrete: Numerical modelling and experimental testing, *Cem. Concr. Res.* 106 (2018) 103–116. doi:10.1016/j.cemconres.2018.02.001.
- [12] L. Reiter, T. Wangler, N. Roussel, R. Flatt, The role of early age structural build-up in digital fabrication with concrete, *Cem. Concr. Res.* (2018) (this issue). doi:10.1016/j.cemconres.2018.05.011.
- [13] B.N. Diggs-mcgee, E.L. Kreiger, M.A. Kreiger, M.P. Case, Print time vs . elapsed time : A temporal analysis of a continuous printing operation for additive constructed concrete, *Addit. Manuf.* 28 (2019) 205–214. doi:10.1016/j.addma.2019.04.008.
- [14] S. Ketel, G. Falzone, B. Wang, N. Washburn, G. Sant, A printability index for linking slurry rheology to the geometrical attributes of 3D-printed components, *Cem. Concr. Compos.* (2018) 0–1. doi:10.1016/j.cemconcomp.2018.03.022.
- [15] E.L. Kreiger, M.A. Kreiger, M.P. Case, Development of the construction processes for reinforced additively constructed concrete, *Addit. Manuf.* 28 (2019) 39–49. doi:10.1016/j.addma.2019.02.015.
- [16] V. Naidu, M. Krause, V. Mechtcherine, Automation in Construction Direct printing test for buildability of 3D-printable concrete considering economic viability, *Autom. Constr.* 109 (2020) 102986. doi:10.1016/j.autcon.2019.102986.

- [17] D. Marchon, S. Kawashima, H. Bessaies-bey, S. Mantellato, S. Ng, Cement and Concrete Research Hydration and rheology control of concrete for digital fabrication : Potential admixtures and cement chemistry, *Cem. Concr. Res.* 112 (2018) 96–110. doi:10.1016/j.cemconres.2018.05.014.
- [18] A. Kazemian, X. Yuan, E. Cochran, B. Khoshnevis, Cementitious materials for construction-scale 3D printing : Laboratory testing of fresh printing mixture, *Constr. Build. Mater.* 145 (2017) 639–647. doi:10.1016/j.conbuildmat.2017.04.015.
- [19] W. Ricardo, H. Fryda, J.-N. Bousseau, P.-A. Andreani, T.J. Andersen, Evaluation of Early-Age Concrete Structural Build-Up for 3D Concrete Printing by Oscillatory Rheometry, 1 (2020) 35–47. doi:10.1007/978-3-030-20216-3.
- [20] T.T. Le, S.A. Austin, S. Lim, R.A. Buswell, A.G.F. Gibb, T. Thorpe, Mix design and fresh properties for high-performance printing concrete, *Mater. Struct. Constr.* 45 (2012) 1221–1232. doi:10.1617/s11527-012-9828-z.
- [21] P. Carneau, R. Mesnil, N. Roussel, O. Baverel, Additive manufacturing of cantilever - From masonry to concrete 3D printing, *Autom. Constr.* 116 (2020) 103184. doi:10.1016/j.autcon.2020.103184.
- [22] M. Moini, J. Olek, J. Youngblood, B. Magee, D. Zavattieri, Additive Manufacturing and Performance of Architected Cement-based Materials, *Under Rev.* (2018). doi:10.1002/adma.201802123.
- [23] L.J. Struble, H. Zhang, G.K. Sun, W.G. Lei., Oscillatory shear behavior of portland cement paste during early hydration, *Concr. Sci. Eng.* 141–149.
- [24] D. Han, R.D. Ferron, Effect of mixing method on microstructure and rheology of cement paste, *Constr. Build. Mater.* 93 (2015) 278–288. doi:10.1016/j.conbuildmat.2015.05.124.
- [25] T. Conte, M. Chaouche, Rheological behavior of cement pastes under Large Amplitude Oscillatory Shear, *Cem. Concr. Res.* 89 (2016) 332–344. doi:10.1016/j.cemconres.2016.07.014.
- [26] Q. Yuan, X. Lu, K.H. Khayat, D. Feys, C. Shi, Small amplitude oscillatory shear technique to evaluate structural build-up of cement paste, *Mater. Struct. Constr.* 50 (2017) 1–12. doi:10.1617/s11527-016-0978-2.

- [27] Y. Qian, S. Kawashima, Use of creep recovery protocol to measure static yield stress and structural rebuilding of fresh cement pastes, *Cem. Concr. Res.* 90 (2016) 73–79. doi:10.1016/j.cemconres.2016.09.005.
- [28] Y. Qian, S. Kawashima, Flow onset of fresh mortars in rheometers: Contribution of paste deflocculation and sand particle migration, *Cem. Concr. Res.* 90 (2016) 97–103. doi:10.1016/j.cemconres.2016.09.006.
- [29] Z. Sun, T. Voigt, S.P. Shah, Rheometric and ultrasonic investigations of viscoelastic properties of fresh Portland cement pastes, *Cem. Concr. Res.* 36 (2006) 278–287. doi:10.1016/j.cemconres.2005.08.007.
- [30] M. Bellotto, Cement paste prior to setting: A rheological approach, *Cem. Concr. Res.* 52 (2013) 161–168. doi:10.1016/j.cemconres.2013.07.002.
- [31] S.Z. Jones, D.P. Bentz, N.S. Martys, W.L. George, A. Thomas, *Rheological Control of 3D Printable Cement Paste and Mortars*, Springer International Publishing, 2019. doi:10.1007/978-3-319-99519-9.
- [32] D. Marchon, S. Kawashima, H. Bessaies-Bey, S. Mantellato, S. Ng, Hydration and rheology control of concrete for digital fabrication: Potential admixtures and cement chemistry, *Cem. Concr. Res.* (2018). doi:10.1016/j.cemconres.2018.05.014.
- [33] M. Moini, J. Olek, B. Magee, P. Zavattieri, J. Youngblood, Additive manufacturing and characterization of architected cement-based materials via X-ray micro-computed tomography, 2019. doi:10.1007/978-3-319-99519-9\_16.
- [34] Tjörvi Björnsson, *Structural analysis of columns with initial imperfections*, University of Iceland, 2017.
- [35] L. Euler, *De Curvis Elasticis* Lausanne and Geneva (The Euler formula was derived in a later paper, *Sur le Forces des Colonnes* Memoires de VAcademie Royale des Sciences et Belles Lettres, Vol. 13, Berlin, 1759.), (1744) 267–268.
- [36] W.F. Chen, E.M. Lui, *Columns with End Restraint and Bending in Load and Resistance Design Factor*, (1985) 105–132.
- [37] A. Boumiz, C. Vernet, F.C. Tenoudjif, C. Technique, I. Fran, G. Cedex, *Mechanical Properties of Cement Pastes and Mortars at Early Ages Evolution with Time and Degree of Hydration*, 7355 (1991).

- [38] R. Jayathilakage, P. Rajeev, J.G. Sanjayan, Yield stress criteria to assess the buildability of 3D concrete printing, *Constr. Build. Mater.* 240 (2020) 117989. doi:10.1016/j.conbuildmat.2019.117989.
- [39] A. Szabo, L. Reiter, E. Lloret-Fritschi, F. Gramazio, M. Kohler, R.J. Flatt, Processing of Set on Demand Solutions for Digital Fabrication in Architecture, in: Mechtcherine V., Khayat K., Secieru E. *Rheol. Process. Constr. Mater. RILEM Bookseries*, Vol 23. Springer, Cham, 2019: pp. 440–447.
- [40] J. Kruger, S. Zeranka, G. Van Zijl, Automation in Construction 3D concrete printing: A lower bound analytical model for buildability performance quantification, *Autom. Constr.* 106 (2019) 102904. doi:10.1016/j.autcon.2019.102904.
- [41] J. Kruger, S. Cho, S. Zeranka, C. Viljoen, G. Van Zijl, 3D concrete printer parameter optimisation for high rate digital construction avoiding plastic collapse, *Compos. Part B.* 183 (2020) 107660. doi:10.1016/j.compositesb.2019.107660.
- [42] John Case, C.T.F. Ross, A. Chilver, *Strength of Materials and Structures*, 4th ed., Wiley, United Kingdom, 1999.
- [43] N.J. Hoff, *Buckling and Stability*.
- [44] G. Gelardi, R.J. Flatt., Working mechanisms of water reducers and superplasticizers, in: *Sci. Technol. Concr. Admixtures*, Woodhead Publishing, 2016: pp. 257–278.
- [45] E. Schlangen, S.C. Figueiredo, Special Issue 4th Brazilian Conference on Composite Materials (2018) Effect of viscosity modifier admixture on Portland cement paste hydration and microstructure, 212 (2019) 818–840. doi:10.1016/j.conbuildmat.2019.04.020.
- [46] M. Palacios, R.J. Flatt., Working mechanism of viscosity-modifying admixtures., in: *Sci. Technol. Concr. Admixtures*, Woodhead Publishing, 2016: pp. 415–432.

### **3. ADDITIVE MANUFACTURING AND CHARACTERIZATION OF ARCHITECTURED CEMENT-BASED MATERIALS VIA X-RAY MICRO-COMPUTED TOMOGRAPHY**

This chapter contains work that was originally published in Springer Nature as “Mohamadreza Moini, Jan Olek, Bryan Magee, Pablo Zavattieri, and Jeffrey Youngblood. *Additive manufacturing and characterization of architected cement-based materials via X-ray micro-computed tomography. In First RILEM International Conference on Concrete and Digital Fabrication, Digital Concrete 2018. DC 2018. RILEM Bookseries. Volume 19., pp. 176-189. Springer, Cham, 2018.*” The original article has been used with permission as stated below.

Reprinted by permission from Springer Nature: Springer, Cham, In: First RILEM International Conference on Concrete and Digital Fabrication – Digital Concrete 2018. DC 2018. RILEM Bookseries. “Additive Manufacturing and Characterization of Architected Cement-based Materials via X-ray Micro-computed Tomography.” Mohamadreza Moini, Jan Olek, Bryan Magee, Pablo Zavattieri, and Jeffrey Youngblood, COPYRIGHT (2018).

Moreover, this chapter contains experimental data collected by Mohamadreza Moini. Data conceptualization was a collaborative effort with co-authors, Jan Olek, Jeffrey P. Youngblood, B. Magee, and Pablo D. Zavattieri. The manuscript was written by Mohamadreza Moini and edited by co-authors. The original article has also been modified for dissertation formatting purposes. I also acknowledge Chven Mitchell from the the 3D X-Ray Microscope Facility in the Department of Physics and Astronomy who assisted with the training on the use of Zeiss Xradia 510 Versa 3D X-ray Microscope that was supported by the Executive Vice President for Research and Partnerships, Major Multi-User Equipment Program 2017 at Purdue University.

#### **Abstract**

There is an increasing interest in the fabrication of cement-based materials via additive manufacturing (AM) techniques. However, the processing-induced heterogeneities and interfaces represent a major challenge. The role of processing in creating interfaces and their characteristics requires understanding of the microstructure of 3D-printed hardened cement paste (hcp). This work investigates the microstructural features of architected cement-based materials, including processing-induced heterogeneous patterns, interfacial regions (IRs), and pore network

distributions with respect to the architectural pattern. A 3D printer was modified and merged with an extrusion system and specimens were 3D-printed using a layer-wise direct ink writing (DIW) process capable of fabrication of 'lamellar' architectures of materials. A lab-based X-ray microscope (XRM) was used to perform X-ray micro-computed tomography (micro-CT) evaluations to explore the microstructural characteristics of 3-day old intact (i.e. not tested) 3D printed and cast specimens at two levels of magnification: 0.4X and 4X. CT scans of printed specimen revealed a patterned pore network and several microstructural features, including: a) macropores (visible during printing), b) micropores at interfacial regions (IRs), c) accumulation of anhydrous cement particles near macropores, and d) rearrangement of filaments away from their designed toolpath. In comparison, microstructural investigation of cast specimen at 4X scan revealed randomly distributed pores with no connectivity throughout the specimen. The aptitude of micro-CT as a non-destructive technique for microstructural characterization of architected cement-based materials is discussed. The role of processing to induce and to pattern heterogeneities such as IRs in materials is demonstrated and the role of architecture in controlling such heterogeneities and their directionality through the interface is discussed.

**Keywords:** 3D-printing, Cement Paste, Micro-CT, Interfacial Region (IR)

### 3.1 Introduction

Properties of hardened cement paste (hcp) are influenced by its microstructure and the way in which the material is cast and placed [1]. Specifically, characteristics of the pore network (i.e., the size and distribution of internal flaws), the morphology of microstructural components, and heterogeneities in the microstructure, all affect mechanical properties of hardened cement-based materials [1,2]. Over the last decades, the use of advanced characterization techniques, such as scanning electron microscopy (SEM), has significantly advanced the understanding of microstructure of cement-based materials. However, the effectiveness of SEM is limited in terms of obtaining three-dimensional information about connectivity and size distribution of pore network [1,3].

X-ray micro-Computed Tomography (micro-CT) has been previously applied to cement-based mortar and concrete materials to characterize pore network [4] and microstructure [5] and their relationships with a variety of key properties including: fracture properties [5,6,7], damage

mechanisms [2,8,9], mass transport [10], and evolution of cement hydration [11]. Micro-CT is a non-destructive technique that captures three-dimensional images of materials without the need for destructive preparation processes such as drying, surface treatments, and vacuuming; all of which are commonly required when preparing specimens for typical microstructural characterization techniques such as MIP, gas sorption, and SEM [1]. As such, the use of micro-CT for microstructural characterization of 3D-printed hcp is advantageous as it does not alter the microstructure while allowing for imaging of elements as large as 10s of millimeters.

During this research, a laboratory-based (i.e. not requiring synchrotron facilities) X-ray microscope was used to explore the microstructural characteristics of intact (i.e. not tested) printed and cast 3-day old cement paste specimens at two magnifications: 0.4X and 4X corresponding, respectively, to the resolution of 32.24  $\mu\text{m}$  and 4.04  $\mu\text{m}$ .

3D-printing via direct-ink-writing (DIW) of colloids, slurries, and pastes allows for control of the architecture of the element and can give rise to a variety of microstructural features [12,13,14]. In this work, four microstructural features observed in 3D-printed lamellar architecture are discussed. All four features were qualitatively detected at 0.4X scans, and further verified at 4X scan. Finally, the microstructure of the printed specimen was compared to a microstructure of conventionally cast specimen.

## 3.2 Methods

### 3.2.1 3D-Printing Setup

To establish a 3D printer capable of printing cement paste via DIW techniques, two separate units were combined. A gantry-based 3D printer (Ultimaker 2 Extended+ used for printing thermoplastic materials) was merged with a stepper motor-driven extrusion system (Structur3d Discov3ry Paste Extruder) to serve as a paste extruder (see **Figure 3.1a**). These two units were connected with tube and luer locks. The resulting system is capable of printing pastes with high yield stress and viscosity and can fabricate elements at prototyping scale (mm). The extruder is capable of applying desirable displacements (extrusion rates) via mounted 75 mL ink-charged syringes as depicted in **Figure. 3.1b**). The 3D printer was modified to allow for mounting of a nozzle holder assembly on the printer gantry rods (**Figure 3.1c**). The nozzle holder is consisted of two lightweight aluminum parts designed and custom-fabricated specifically for this printer. To

continuously feed the paste from the syringe to the printer nozzle, a polyethylene tube for paste delivery (with an internal diameter of 4.3 mm and 450 mm long) was passed through the nozzle holder assembly. A female luer lock was inserted into the nozzle holder to connect the tube to the nozzle (**Figure 3.1d**). To connect the other side of the tube, onto the syringe a male luer lock (**Figure 3.1e**). The luer locks and the standard Nordsen nozzle (gauge 15 with 1.36 I.D.) are shown **Figure 3.1f**.

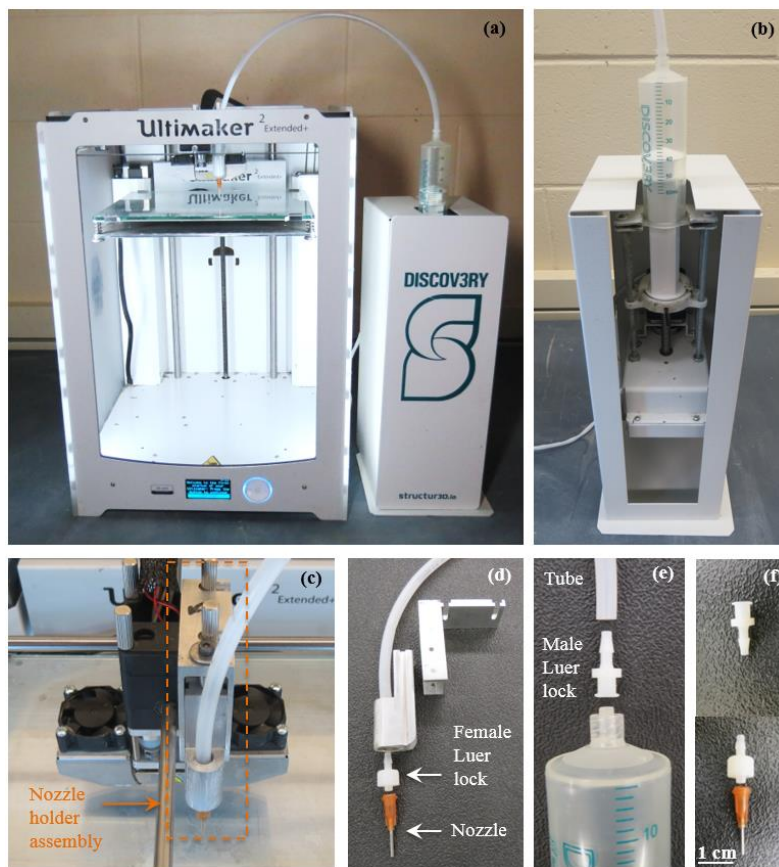


Figure 3.1. 3D printer setup: a) Gantry 3D printer (Ultimaker 2 Extended+) and stepper motor-based extrusion (Discov3ry) system; b) Syringe and plunger mounted onto the stepper motor system; c) Nozzle holder assembly mounted onto the 3D printer gantry guide rods; d) Nozzle holder assembly and the female luer lock used to connect the tube to the nozzle; e) male luer lock used to connect syringe to the tube; f) nozzle and luer locks shown separately

### 3.3 Ink Design, Mixing Procedure, and Curing

An iterative mix design process was employed to identify cement paste inks with flow properties (i.e., yield stress, and viscosity) suitable for the DIW process. A combination of high-range-water-reducing-admixture (HRWRA) and viscosity modifying admixture (VMA) are

widely used in self-consolidating concrete to avoid opposing effects of segregation at rest and high fluidity during pumping [15]. In DIW process of cement paste, it is also critical to achieve yields stresses that are high enough to allow the materials to be self-supporting (shape-holding). In the process of DIW of ceramic slurries (on the mm scale) the increase in the content of solids results in both, the increase in yield stress and in viscosity [16]. Moreover, the yield stress of cement paste is known to decrease with the addition of superplasticizers and the apparent viscosity is typically known to increase with the addition of VMAs [15]. In this work, the successful ink was designed with yield high enough for shape-holding and viscosity suitable for extrusion. A low water to cement ratio of 0.27, corresponding to a solid content of 53% (by mass), was used in this work. This percentage of solid content is found to provide suitable in ceramic paste as well [16]. In the case of cement paste, such low water to cement ratio can produce very stiff mixtures that can experience bleeding while undergoing extrusion. As such, a HRWRA was used to lower yield stress (and to ensure extrudability) and VMA was used to reduce bleeding. The use of VMA is highly desirable for DIW process. Specifically, it enhances the stability of the ink during extrusion and that of the specimen upon deposition [15].

The final ink used in this work consisted of the sub 150  $\mu\text{m}$  fraction of commercially available Type I cement (ASTM C150 [17]) obtained from Buzzi Unicem, USA; the deionized water; HRWRA (MasterGlenium 7700), and VMA (MasterMatrix 362). Both chemical admixtures met the requirements of the ASTM C494 [18]. Optimal dosages were established based on findings of a related previous study [19]. For each 250.0 g of cement, the mix contained 65.2, 1.1 and 3.0 grams of deionized water, HRWRA and VMA, respectively. HRWRA and VMA were added to the water consecutively and stirred until they could not be visually observed. The liquid phase was then added to cement. A Twister Evolution Venturi vacuum mixer was used for mixing the paste to eliminate entrapped air as the presence of the air bubbles will degrade the quality of the ink. The pre-mixing mode of the mixer was used during the first 25 seconds of the mixing to process the paste at slow speed while subjected to a 70% of vacuum level provided by the mixer. This was followed by mixing at 400 rpm for 90 seconds at 70% vacuum level. The paste was mixed for a second time at 400 rpm for 90 seconds at 100% vacuum level of the mixer. The paste was then loaded into the syringe. The syringe was then outfitted with the plunger and mounted on the extruder as depicted in **Figure 3.1b**. The mixing process was performed within 5 min after combining cement and liquid. The specimens were cast and printed in lab environment at  $18 \pm$

3 °C and  $45 \pm 5$  % relative humidity. Immediately after printing (or casting), the specimens were placed in a sealed curing box which maintained constant relative humidity of  $93 \pm 2$  % (by using saturated solution of potassium nitrate). The box was kept at constant temperature of  $18 \pm 3$  °C.

### 3.3.1 Slicing and Design

In order to generate a toolpath required for lamellar architecture, a commercially available slicer (Simplify3D) was used to generate the G-code commands. A cubical 3D object was introduced to the slicer and geometrical parameters were assigned to it to achieve desired printing path and architecture. The G-code command included 5 axis of control: Point cloud coordinates (X, Y, Z axis) to control the movements of the nozzle and the bed; extrusion (E axis) to control the amount of extrusion relative to the nozzle movement; and printing speed (F axis) to control the speed of the nozzle movement. E and F axis were controlled via an extrusion rate multiplier and printing speed in the slicer. Several other printing parameters, including the location, the amount, and the speed of retraction, were also scripted to the G-code in the slicer. To generate the tool path, a 25x25x25 mm cube was introduced to the slicer and a continuous printing path in each layer was designed to create lamellar architectures (**Figure 3.2a**). To achieve a solid specimen, 100% infill was used for lamellar architectures (**Figure 3.2b**). A layer height (filament height) of 1.00 mm and the internal diameter of the nozzle of 1.36 mm were specified in the slicer. The specified printing speed of 250 mm/min employed, resulting in a speed of 87 seconds/layer. These printing and geometrical parameters were established by trial and error to obtain a suitable print quality (i.e., filament width and height close to that specified in the slicer). A schematic cross-section of the lamellar architecture considered and a resulting specimen are shown in **Figures 3.2c** and **3.2d**.

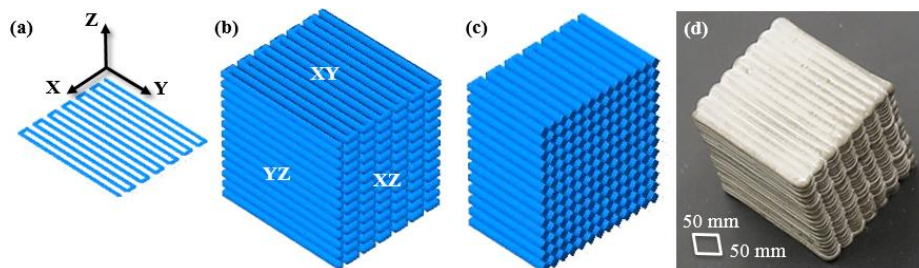


Figure 3.2. Schematics of lamellar architectures: a) Printing path of individual layers; b) Printing path of a cube specimen and; c) Cross-section of the specimen with lamellar architecture; d) 3D-printed lamellar architecture cube via DIW

### 3.3.2 Micro-CT and Scanning Specimens

X-ray micro-computed tomography (micro-CT) is an imaging technique that involves the recording of series of 2D radiographs (images), taken at various angles around a rotating object, to mathematically reconstruct a spatial map and digitally render the entire volume (i.e., three-dimensional appearance) of an object [2]. Resulting 3D renditions are typically presented as a series of 2D (i.e., sliced images) with intensities corresponding to X-ray absorption and material density at each voxel [20]. The resulting variations in intensity allow for identification of various phases and features of the microstructure and their 3D distribution.

Conventionally, X-ray microscopes employed for micro-CT characterization technique, use a flat panel detector and thus rely on single-step (i.e., geometric) magnification. As a result, resolution degrades with increasing sample size and working distance. In this study, an X-ray microscope (XRM), Zeiss Xradia 510 Versa was utilized, which allows of an increase in the resolution of scans through dual-stage magnification process. In the first stage, the field of view (FOV) desirable to scan the entire volume of the specimen was established via geometric magnification process, which involved setting distances between the source, detector, and specimen (as in conventional micro-CTs). In a second stage, additional optical magnification was enabled at the detector system through objective lenses. The detector is equipped with scintillator and objective lens which converts X-rays to light rays and thus allows for optical magnification and higher resolution. The initial (i.e. the 0.4X) scan allowed a large FOV and thus facilitated to scan the entire specimens (32.24  $\mu\text{m}$  pixel size). This was followed by a 4X scan, allowing higher resolution (4.04  $\mu\text{m}$  pixel size) at regions of interest (ROI). A beam energy of 150 KeV, a power of 10 W, exposure times of 0.94 second and 4 seconds, and full 360° rotation were used for 0.4X and 4X scans of printed specimen and a beam energy of 140 KeV, a power of 9 W, exposure times of 1 second, and full 360° rotation were used for 0.4X scans of cast specimen respectively. Dragonfly software was used for post-processing of the data. One cast and one 3D-printed hcp cubes (25x25x25 mm  $\pm$  1 mm) were used in this experiment.

## 3.4 Results and Discussion

### 3.4.1 3D-Printed Lamellar Architecture Micro-CT (0.4X and 4X scans)

**0.4X Scan.** The 0.4X magnification CT scan of the intact specimen revealed the presence of four microstructural features: macropores, micropores, rearrangement of filaments and accumulation of anhydrous cement grains. These features are illustrated in **Figures 3.3a, 3.3b and 3.3c**, for XZ, YZ, XY planes respectively, and in **Figure 3.3d** for the 3D rendition of the interior of the lamellar architecture specimen. In micro-CT images of hcp, darker intensities represent pores filled with air or water, with greyscale intensities corresponding to hydrated cement paste products and brighter regions corresponding to anhydrous cement grains [1]. The previously mentioned four microstructural features are analyzed in more details below:

**Macropores.** As seen in **Figures 3.3a and 3.3d**, there are several regions that contain large pores (macropores) located between adjacent filaments of the same layer. These pores are aligned along the filament in the direction of the Y axis as can be seen in the regions outlined by white rectangles in **Figures 3.3a and 3.3d**. They are typically wider than 100  $\mu\text{m}$  and range in length from few to 10s of millimeters. These macropores are the result of variability in the width of the filament as it is being extruded from the tip of the nozzle. That variability is, in turn, likely the result of inconsistencies in the local properties of ink under extrusion.

**Micropores (Micro-channels).** The second type of pores was observed to exist between adjacent filaments of the adjacent layers (see the regions outlined by blue rectangles shown in **Figures 3.3a and 3.3d**). These micropores (or micro-channels) are smaller than 100  $\mu\text{m}$  in diameter but can be 10s of millimeters long. They are located between filaments along the Y axis (i.e., they are present in the interfacial regions (IRs) of the filaments). The horizontal (i.e., XY) slices H1 and H2 shown in **Figure 3.3c**, correspond to, respectively, the core (i.e., through the center) and interfacial regions of the filaments as indicated in cross-sectional view (XZ) in **Figure 3.3a**. Similarly, vertical (YZ) slices W1 and W2 shown in **Figure 3.3b** also correspond to the core and interface regions of the filaments indicated in **Figure 3.3a**. Analysis of **Figures 3.3b and 3.3c** indicate that micro-channels (appearing in these figures as darker regions within the matrix) are only present in the images representing slices through interfaces (i.e. they are absent from images representing slices through the cores). It should be noted, however, that these micro-channels are

more pronounced in horizontal than in the vertical planes. This can be clearly seen by comparing images of the IR H2 (shown in **Figure 3.3b** and IR W2 (shown in **Figure 3.3c**).

Finally, one would expect that the gap formed between four semi-circular filaments will have a diamond-shaped cross-section (when viewed along the axes of the filaments). However, as illustrated in **Figures 3.4** and **3.5**, this was not the case for the lamellar architecture specimen prepared for this study as the gaps have been found to be triangular in shape. The next sections describe two other characteristics of the printed microstructure (rearrangement of the filaments and accumulation of anhydrous cement grains near macropores), which are considered to be responsible for the formation of these triangular gaps.

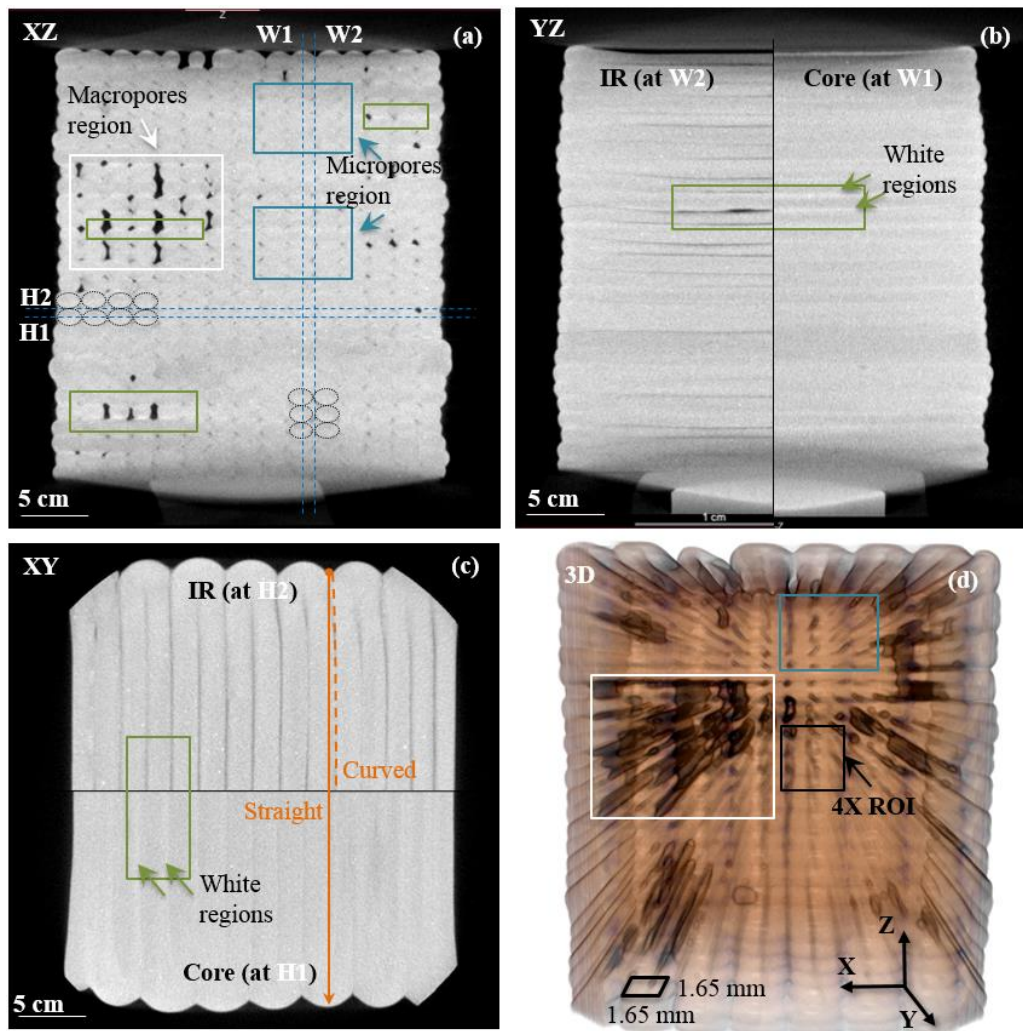


Figure 3.3. X-ray micro-CT images of the microstructure of 3-days old paste specimen with lamellar architecture collected during 0.4X scan: a) 2D projection on the XZ plane; b) 2D projection on the YZ plane; c) 2D projection on the XY plane, and; d) Three-dimensional rendition of the entire volume of the specimen

*Self-Drifting of Filaments from the Programmed Toolpath.* The examination of CT images revealed that the internal filaments of the lamellar architecture self-drifted (to an extent of about half width of the filament) from their targeted (programmed) toolpath. From the top view (i.e., XY plane), the filaments in all interior layers were observed to follow slightly curved, rather than straight, paths. This is in spite of the fact that the nozzle was programmed to move along a linear tool path parallel to the Y axis. This observation was made possible due to the differences in the gray level intensities between the signals from the core sections and interfaces of the filaments. A typical curvature is highlighted in **Figure 3.3c** by the set of two orange lines: the solid line on the left showing the location where a straight interface should have been observed and the dashed line on the right that shows the actual (slightly curved) path of the actual interface. In the consecutive layers of the microstructure, the direction of this curvature successively changes to left and right. This has to do with the opposite direction of printing path in successive layers. The causes of this self-drifting of the filaments are further elaborated in the section describing the 4X scan.

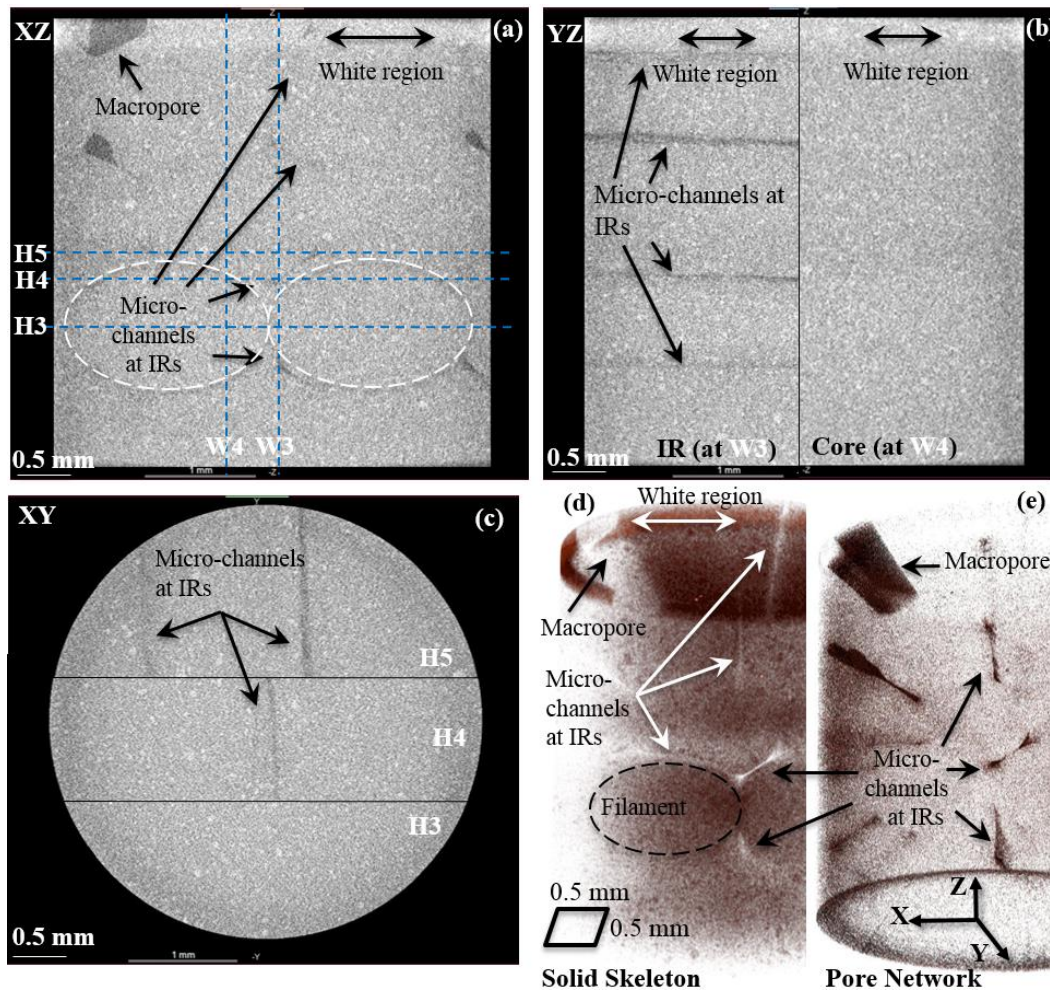


Figure 3.4. CT images of the microstructure of 3-days old intact specimen with lamellar architecture collected during 4X scan: a) XZ; b) YZ; c) XY planes; d) 3D image of the solid skeleton; e) 3D image of pore network

***Accumulation of Anhydrous Cement Grains near Macropores ('White Regions')***. The 0.4X CT scans also revealed the accumulation of the unhydrated (anhydrous) cement grains in the IRs near the macropores. This phenomenon was observed in both, the horizontal and vertical interfacial planes of lamellar architecture. In addition, the 4X scan demonstrated the presence of a subtle, 'brighter' zone at the horizontal interfaces, typically also near the macropores. These brighter regions of the microstructure are referred to in this chapter as 'white regions' and are outlined by green rectangles in **Figures 3.3a, 3.3b** and **3.3c**. The more in-depth analysis of these white regions is presented in the section describing the 4X scan.

**4X Scan.** The 3D scan of the specimens resulting from the 0.4X scan shown in **Figure 3.3d** has been used to select an internal region of interest (ROI) to be evaluated at higher (i.e., 4X)

magnification. That ROI is outlined by a red square rectangle in **Figure 3.3d** and the details are presented in **Figure 3.4**. The examination at the magnification 4X was performed to further explore the four types of microstructural features discussed during the analysis of the results from the 0.4X scan. Specifically, the 4X CT scan provided additional information on the shape of the micro-channels and their connectivity in the IRs, the rearrangement of the paths of the filaments, and the nature of white regions. The 2D projections of individual XZ, YZ, XY planes are shown in, respectively, **Figures 3.4a**, 4b and 3.4c; **Figure 3.4d** shows the 3D rendition of the interior of the specimen. The higher resolution of these images (compared to the resolution obtained during the 0.4X scans), allowed for the identification of larger cement grains (they appear as bright spots against the gray matrix of the hydrated products) and pores (they appear as dark spots).

**Macropores.** The previously mentioned ROI was selected to capture the bottom edge of a typical macropore between two filaments of the same layer. An example of such pore is shown in the top left corner of **Figure 3.4a**. This macropore is also shown in the image of the solid skeleton (**Figure 3.4d**) and that of the pore network (**Figure 3.4e**).

**Micropores (Micro-channels).** This section provides further analysis of the shape of the micro-channels as observed in 4X images. Specifically, it can be observed that the triangular micro-channels (**Figure 3.4a**) are commonly connected to one another and, when viewed in 3D, they form of an inclined dog-bone shape as illustrated in **Figures 3.4d** and **3.4e**. As filaments rearrange upon deposition and move closer together, the connectivity between the micro-channels can be facilitated. Thorough investigation of the 4X scanned volume qualitatively indicated that this connectivity between micro-channels occurs through IRs and form pattern of pore network aligned with the filament architecture (**Figure 3.4d** and **4e**). The typical three horizontal (XY) slices of H3, H4, H5 (indicated in **Figure 3.4a**) and shown in **Figure 3.4c**), demonstrate the homogeneous characteristics of the microstructure along the ‘cores’ (H3), compared to heterogeneous characteristic along IRs where micro-channels are present (H4, H5). Similarly, the vertical (YZ) slices of W3 and W4 (indicated in **Figure 3.4a** and shown in **Figure 3.4b**), demonstrate the homogeneous characteristic of the microstructure along the ‘cores’ (W4), compared to the heterogeneous characteristic of the microstructure along ‘IRs’ (W3).

**Self-Drifting of Filaments from the Programmed Toolpath.** As discussed in the section presenting the 4X scan, the triangular cross-sectional shape of the micro-channels is correlated with the rearrangement of the filaments. This indicates that the filaments are shifted upon

deposition towards an adjacent filament deposited before them. This was confirmed via visual observations during printing. Rearrangement of the filament toward a higher packing arrangement shown in **Figure 3.4e** further confirms this observation. As the filaments rearrange from their designed path, the shape of the pores changes from diamond to triangle as schematically shown in **Figure 3.5a** and **5b**. The similarity between the triangular cross-sectional shapes of microchannels shown in **Figure 3.4e** and the illustration presented in **Figure 3.5b** confirms that the formation of the triangular-shape pores is the result of self-drifting of the filaments.

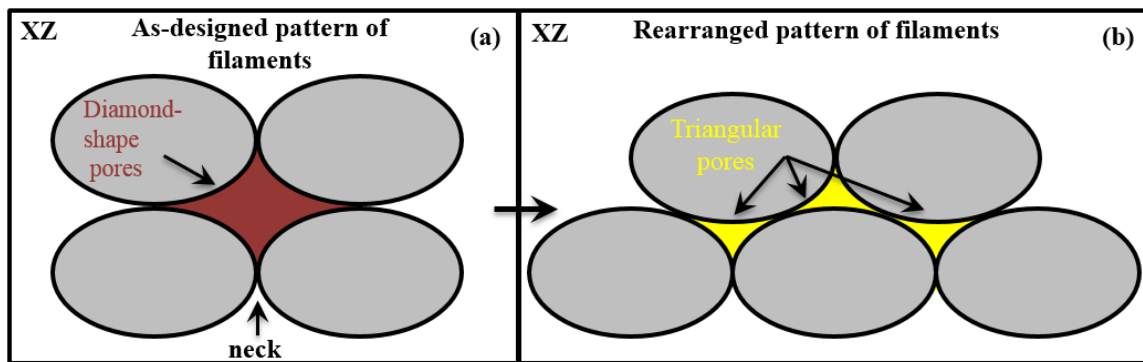


Figure 3.5. Schematic illustration of arrangements of filaments and shapes of the pores along the Y direction: a) As-designed pattern in lamellar architecture containing diamond-shaped pore and; b) Rearranged filament pattern showing triangular-shaped pores (similar to those depicted in 4X CT image (Figure 3.4 e))

A variety of mechanisms for interaction and driving force for filament rearrangements can be hypothesized. As an example, during deposition, each filament interacts with the adjacent filament and therefore is shifted towards it. As each filament is deposited, it is designed to overlap and make contact with its adjacent filaments. In addition, the phenomenon such as die swell and relaxation of the filament due to gravity upon deposition may facilitate this contact. Once the filaments make contact, the viscous flow can be driven by the differences in surface curvature between the body of the filament and its neck regions (see **Figure 3.5a**), and can bring the adjacent filaments closer. In addition, the rearrangement may cause lamellar architecture to achieve a higher packing density and possibly establish a densifying mechanism of viscoelastic materials upon deposition.

*Accumulation of Anhydrous Cement Grains near Macropores ('White Regions')*. The subtle trace of 'white region' at the horizontal interfaces discussed in connection with the 0.4X scan is captured in greater details in 4X (see the top parts of **Figure 3.4a** and **3.4b**). A thorough

investigation this region demonstrates that the white region contained a higher fraction of anhydrous cement grains, which explains why they appear brighter as cement grains have higher density relative to the density of the hydration products and pores. Similarly, the images of the solid skeleton (shown in **Figure 3.4d**) and that of the pore network (shown in **Figure 3.4e**), both illustrate the accumulation of anhydrous cement grains in the white region. The fact that white regions are only seen in the horizontal planes suggests that an encouraging drying environment during the printing of each layer occurs in these planes. The presence of the macropores may have additionally enhanced drying. The use of ink with a low water to cement ratio of 0.275 can also be contributing to the increased rate of drying at the horizontal IRs due to longer exposure time to air drying compared to vertical IRs.

### **3.4.2 Cast Specimen in 0.4X micro-CT (0.4X scan)**

**0.4X Scan.** The 0.4X scan of cast specimen showed the random distribution of the pore network. The XY plane of 0.4X scan of intact cast specimen is illustrated in **Figure 3.6a** whereas **Figure 3.6b** shows the 3D rendition of the interior of the specimen. The darker regions in both images represent pore regions. The random distribution of pores in cast elements and the lack of patterned heterogeneous network compared to those observed in lamellar architecture (**Figure 3.3**), highlights the differences between the microstructure of traditionally cast and 3D-printed hcp specimen.

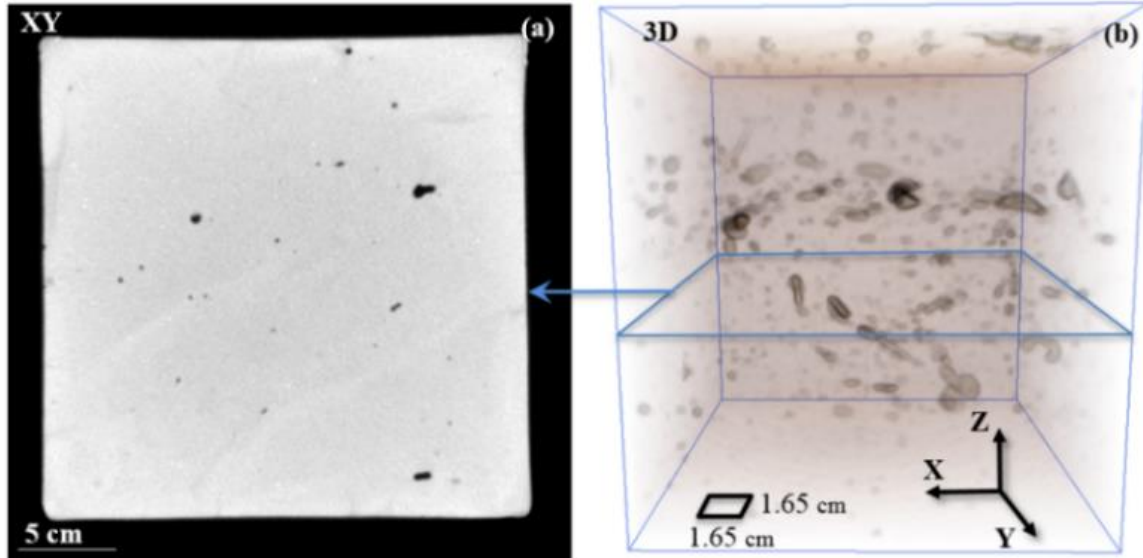


Figure 3.6. X-ray micro-CT images of the 3-days old intact cast specimen collected during the 0.4X scan: a) 2D projection on the XY plane and; b) 3D rendition of the entire specimen

**Further Discussion.** The alignment of macropores and micro-channels with the pattern of the filaments in the lamellar architecture (**Figure 3.3d** and **Figure 3.4e**) suggests that the pore network is inherently associated with the specific architecture of the specimen. However, it is also possible that the location and the amount of the macropores are linked to the specific printing parameters used in this study.

From 0.4X scan, it is evident that the characteristics of the microstructure are different between the solid cores and IRs, induced by the presence of interfacial porosity and the differences in its distribution. It could be hypothesized that the heterogeneous micropore network is present due to the initial presence of extrusion-induced lubricating layer (i.e. layer containing water that surrounds the filament upon deposition) which makes the outer region of the filaments more prone to evaporation thus resulting in the creation of the micropores at IRs. The evaporation and the subsequent wetting at the interface due to deposition of successive layers could also give rise to anisotropic properties of the microstructure and 3D-printed elements. It is also considered that the presence of triangular micro-channels as shown in **Figure 3.5b** could be induced during deposition. Given the round shape of the nozzle, air and lubricating water surrounding the filaments can be trapped in between filaments upon deposition of each layer. The presence of lubricating layer followed by drying mechanisms during the print and continuing hydration of cement paste can leave micropores at the IRs across the circumferential zone of the filament as indicated by the

dashed oval in **Figure 3.4e**. From 0.4X scan, it is evident that the characteristics of the microstructure are different between the solid cores and IRs, due to the presence of interfacial porosity and the differences in its distribution. Horizontal interfaces were exposed to air for a longer period of time than vertical interfaces during the printing process. The higher amount of horizontal (dark) IRs compared to (also dark) vertical IRs (**Figures 3c** and **3.3b**) indicates the higher amount of drying and resulting micropores in horizontal planes (XY). This observation indicates the existence of the correlation between exposure time and formation of heterogeneous IRs in different planes, which can result in anisotropy of mechanical properties of the 3D-printed specimen. The accumulation of anhydrous cement grains near macropores in horizontal IRs could be the result of the higher amount of drying at the horizontal IRs. These IRs are shown to be connected to one another through the micro-channels in the microstructure of 3D-printed lamellar architecture as shown in **Figure 3.4e**. This heterogeneously patterned pore network, together with the presence of macropores, causes anisotropy in the 3D-printed elements. This anisotropy can lead to differences in mechanical properties between the 3D-printed specimen and the cast specimens, depending on the architecture of materials and the interfacial (bond) strength of 3D-printed element in different directions. The presence of the interface is very important as IRs follows the pattern of the filament and overall layered architecture of the element. The architecture can then be designed to allow damage and micro-cracking to be promoted at the weak IR to achieve higher fracture resistance without sacrificing the strength.

It was previously discussed that in 3D-printed hcp elements, a wide variety of heterogeneous features could exist over a broad range of scales [21,22,23]. Application of micro-CT characterization technique for 3D printed lamellar architecture demonstrated the presence of the weak IRs induced by the processing and patterned via architecture. In addition, rearrangement of the filaments and the resulting change in morphology of the pores was revealed. Connectivity of micropores was discovered in the 4X scan in 3D-printed architecture. As revealed by comparing the 4X scans of the printed and cast specimens, their microstructure is very different. These observations reveal the role of processing in determining the microstructure of materials.

### 3.5 Summary

- Micro-CT images of 3D-printed lamellar architecture collected during this study revealed four characteristic features of the microstructure not observed in the cast specimens, thus indicating these features resulted from the processing of material.
- The previously mentioned microstructural features included the following: a) macropores (i.e., visible gaps formed during printing), b) micropores at interfacial regions (IRs) of filaments in the form of micro-channels smaller than 100  $\mu\text{m}$ , c) self-rearrangement of filaments from their designed toolpath, and d) high accumulation of anhydrous cement particles near the large pores. All of these four features were qualitatively detected at the 0.4X scans, and further verified at the 4X scan. The presence of these features could play a role in determining the overall mechanical response of architected hcp specimen.
- Pore network (at both macro and micro scale) appeared to be aligned with respect to the direction of the filaments in the lamellar architecture of the printed specimen.
- Micro-CT demonstrated great aptitude (as non-destructive technique) for capturing spatial heterogeneities of the microstructure of 3D-printed elements as large as 10s of mm. The dual-stage magnifications system used in this study facilitated higher resolutions at large working distance, thus allowing CT of larger specimens.

### 3.6 Acknowledgements

The authors gratefully acknowledge generous support from the National Science Foundation (CMMI 1562927) of this research.

### 3.7 References

- [1] Gallucci, E., Scrivener, K., Groso, A., Stampanoni, M., & Margaritondo, G.: 3D experimental investigation of the microstructure of cement pastes using synchrotron X-ray microtomography ( $\mu\text{CT}$ ). *Cement and Concrete Research* 37(3), 360-368 (2007).
- [2] De Wolski, S. C., Bolander, J. E., & Landis, E. N.: An in-situ X-ray microtomography study of split cylinder fracture in cement-based materials. *Experimental Mechanics* 54(7), 1227-1235 (2014).

- [3] Scrivener, K. L.: Backscattered electron imaging of cementitious microstructures: understanding and quantification. *Cement and Concrete Composites* 26(8), 935-945 (2004).
- [4] Lu, S., Landis, E. N., & Keane, D. T.: X-ray microtomographic studies of pore structure and permeability in Portland cement concrete. *Materials and Structures* 39(6), 611-620 (2006).
- [5] Diamond, S., & Landis, E.: Microstructural features of a mortar as seen by computed microtomography. *Materials and Structures* 40(9), 989-993 (2007).
- [6] Landis, E. N., Nagy, E. N., & Keane, D. T.: Microstructure and fracture in three-dimensions. *Engineering Fracture Mechanics* 70(7-8), 911-925 (2003).
- [7] Landis, E. N., Nagy, E. N., Keane, D. T., & Nagy, G.: Technique to measure 3D work-of-fracture of concrete in compression. *Journal of engineering mechanics* 125(6), 599-605 (1999).
- [8] Landis, E. N., & Keane, D. T.: X-ray microtomography for fracture studies in cement-based materials. In: *Developments in X-Ray Tomography II*, pp. 105-114. International Society for Optics and Photonics. (1999).
- [9] Landis, E. N., Zhang, T., Nagy, E. N., Nagy, G., & Franklin, W. R.: Cracking, damage and fracture in four dimensions. *Materials and Structures* 40(4), 357-364 (2007).
- [10] Sugiyama, T., Promentilla, M. A. B., Hitomi, T., & Takeda, N.: Application of synchrotron microtomography for pore structure characterization of deteriorated cementitious materials due to leaching. *Cement and Concrete Research* 40(8), 1265-1270 (2010).
- [11] Gastaldi, D., Canonico, F., Capelli, L., Boccaleri, E., Milanesio, M., Palin, L., ... & Stampanoni, M.: In situ tomographic investigation on the early hydration behaviors of cementing systems. *Construction and Building Materials* 29, 284-290 (2012).
- [12] Lewis, J. A.: Direct ink writing of 3D functional materials. *Advanced Functional Materials* 16(17), 2193-2204 (2006).
- [13] Duoss, E. B., Weisgraber, T. H., Hearon, K., Zhu, C., Small, W., Metz, T. R., Vericella, J.J., Barth, H.D., Kuntz, J.D., Maxwell, R.S. and Spadaccini, C.M.: Three-dimensional printing of elastomeric, cellular architectures with negative stiffness. *Advanced Functional Materials* 24(31), 4905-4913 (2014).
- [14] Raney, J. R., Compton, B. G., Mueller, J., Ober, T. J., Shea, K., & Lewis, J. A.: Rotational 3D printing of damage-tolerant composites with programmable mechanics. *Proceedings of the National Academy of Sciences* 115 (6), 1198-1203 (2018).

- [15] Aïtcin, P. C., Flatt, R. J. (Eds.): Science and technology of concrete admixtures. Woodhead Publishing. (2015).
- [16] Rueschhoff, L., Costakis, W., Michie, M., Youngblood, J., & Trice, R.: Additive manufacturing of dense ceramic parts via direct ink writing of aqueous alumina suspensions. *International Journal of Applied Ceramic Technology* 13(5), 821-830 (2016).
- [17] ASTM C150 – Standard Specification for Portland Cement (2017).
- [18] ASTM C494 – Standard Specification for Chemical Admixtures for Concrete (2016).
- [19] Moini M.: Master's thesis, University of Wisconsin-Milwaukee (2015).
- [20] Landis, E. N., & Keane, D. T.: X-ray microtomography. *Materials characterization* 61(12), 1305-1316 (2010).
- [21] Le, T. T., Austin, S. A., Lim, S., Buswell, R. A., Law, R., Gibb, A. G., & Thorpe, T.: Hardened properties of high-performance printing concrete. *Cement and Concrete Research* 42(3), 558-566 (2012).
- [22] Spangenberg, J., Roussel, N., Hattel, J. H., Stang, H., Skocek, J., & Geiker, M. R.: Flow induced particle migration in fresh concrete: theoretical frame, numerical simulations and experimental results on model fluids. *Cement and Concrete Research* 42(4), 633-641 (2012).
- [23] Choi, M., Roussel, N., Kim, Y., & Kim, J.: Lubrication layer properties during concrete pumping. *Cement and Concrete Research* 45, 69-78 (2013).

## 4. QUANTITATIVE INVESTIGATION OF PROCESSING-MICROSTRUCTURE RELATIONSHIP IN 3D-PRINTED LAMELLAR CEMENT PASTE ELEMENTS VIA MICRO-COMPUTED TOMOGRAPHY

This chapter contains experimental data collected by Mohamadreza Moini. Image analysis was a collaborative effort between Mohamadreza Moini and Ahmadreza Baghaie. Data conceptualization was a collaborative effort with Jan Olek, Jeffrey P. Youngblood, and Pablo D. Zavattieri. The manuscript was written by Mohamadreza Moini and edited by Jan Olek, Jeffrey P. Youngblood, and Pablo D. Zavattieri.

### Highlights

- The processing-microstructure relationship was investigated.
- 3D-printed element represented a unique patterned and connected pore microstructure, indicating of a connected pore network.
- The connected pore microstructure was found an interconnection between micro-channels and micro-pores at the interfacial regions.
- 3D-printed element represented a unique patterned pore microstructure in which three features previously reported (macro-pores, micro-channels, and interfacial micro-pores), were found to have resided in three distinct pore volume domains.
- The largest pores found in the entire 3D-printed element were larger than that of the reference cast element (at 32-39  $\mu m$  range of resolutions). In contrast, the small high-frequency pores of the 3D-printed element were smaller than that of the cast element. The dissimilarities indicate that 3D-printing strongly alters the microstructure.

**Keywords:** Macro-pores, micro-channels, interfacial micro-pores, micro-CT, 3D-printing, hardened cement paste (hcp)

## Abstract

Direct-ink-writing (DIW) is a 3D-printing process that provides the opportunity for patterning the materials' architecture in a layer-by-layer fashion. However, exploiting this opportunity requires establishing a fundamental understanding of the relationship between the DIW process and the resulting hardened microstructure of materials. This chapter quantitatively investigates the microstructural phases of a 3D-printed hardened cement paste (hcp) element with 'lamellar architecture'. A lab-based X-ray microscope (XRM) capable of two levels of magnification (0.4X and 4X) was used to characterize the microstructure of intact 3-days old lamellar and reference cast hcp elements.

The entire volume of 3D-printed and cast hcp elements were characterized using 0.4X magnification corresponding to resolutions of  $32.24 \mu\text{m}$  and  $38.99 \mu\text{m}$ , respectively. Three microstructural features (i.e., macro-pores, micro-channels, and interfacial micro-pores) that were qualitatively reported (in chapter three) were found to reside in three distinct pore size domains. It was also found that the largest pores of the 3D-printed element were larger than the largest pores of the reference cast element. Also, the smallest high-frequency pore sizes of the 3D-printed element were found to be smaller than those observed in the cast element. A representative region of interest (ROI) of the 3D-printed element (selected from the center of the element containing a micro-channel and interfacial micro-pores) was further characterized using 4X magnification corresponding to a resolution of  $4.04 \mu\text{m}$ . Analysis of microstructure at higher (i.e., 4X) magnification of a ROI indicated that the micro-channels were connected to one another through the macro-pores present at interfacial regions. The results indicate that 3D-printed elements have a unique patterned and interconnected pore microstructure. Therefore, the presence of a connected pore network in the entire microstructure of the 3D-printed lamellar element can be inferred.

## 4.1 Introduction

3D-printing process allows patterning of the cement-based materials in three dimensions and thus achieving novel and enhanced mechanical responses [1–6]. In patterning the materials, 3D-printing process also alters the materials' microstructure. For example, several studies on the hardened microstructure of 3D-printed cement-based materials have reported that layer-by-layer 3D-printing processes resulted in formation of interfaces between deposited filaments and lesser

amount of hydration products [7,8]. Moreover, it was revealed that changes in processing parameters such as increase of printing speed and time gap between the layers increased the porosity of 3D-printed hardened cement-based materials [8,9]. A few other studies have indirectly investigated the microstructural characteristics of the interfaces between the layers by (altering processing parameters and) mechanically characterizing the bond strength of the deposited filaments [8–10]. These limited studies insightfully inform us of a processing-microstructure relationship and mechanical characteristics of the interfaces in 3D-printed cement-based materials. This chapter focuses on micro-computed tomography ( $\mu$ -CT) characterization technique to quantitatively investigate the processing-microstructure relationship in 3D-printed hardened cement paste (hcp) elements with ‘lamellar architecture’. Specifically, three of the microstructural features (i.e., macro-pores, micro-channels, and interfacial micro-pores) qualitatively reported by authors in the past [7] have been analyzed in this chapter. An image analysis was performed on the slice images of the entire 3D-printed and reference cast elements obtained from the X-ray microscope (XRM) at 0.4X magnification. The pore size and pore frequency of these three pore types of 3D-printed lamellar element were analyzed using an image analysis technique and compared to a reference cast element. Similarly, an image analysis was conducted on the slice images of a representative region of interest (ROI) obtained from a 4X magnification. The results indicate that 3D-printed elements have a unique patterned and interconnected pore microstructure.

## 4.2 Materials and Methods

### 4.2.1 3D-Printing, Slicing, and Design

A 3D printer capable of printing cement paste via layer-by-layer extrusion process with two separate units was previously established by the authors and was used in this work [7]. A standard Nordsen nozzle (gauge 15 with 1.36 I.D.) was used for depositing materials with a width of 1.63 mm. Similarly, a commercially available slicer (Simplify3D) was used to generate the G-code commands. A slicing procedure was previously established by the authors and was used in this work [7]. To design the printing paths in order to achieve the desired lamellar element, a cubical 3D object (25x25x25 mm cube) was inserted in the slicer and the geometrical parameters (including filament height, width, and orientation at each layer) and processing parameters (such as printing speed, extrusion multiplier, and infill percentage). A continuous printing path in each

layer was designed to create lamellar element as shown in **Figure 4.1a**. To achieve a toolpath for solid specimens (as shown in **Figure 4.1b**), 100% infill was used. A layer height (filament height) of  $1.00\text{ mm}$  and the extrusion width of  $1.63$  were specified in the slicer (using a nozzle with of I.D. of  $1.36\text{ mm}$ ). The specified printing speed was  $250\text{ mm}/\text{min.}$ , resulting in a speed of  $93\text{ s}$  per layer. Each layer was exposed to the environment for a duration between  $9.6\text{ s}$  to  $186\text{ s}$ . A schematic cross-section of the lamellar element was shown for clarity in **Figure 4.1c**. The resulting 3D-printed lamellar element was shown in **Figure 4.1d**.

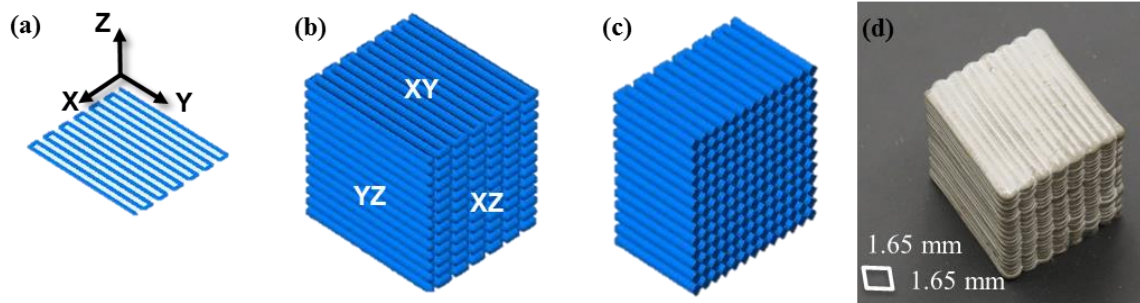


Figure 4.1. Schematics of printing path and resulting 3D-printed specimen with lamellar architected element: (a) schematics of printing path of individual layers of lamellar architecture; (b) schematics of printing path of the entire element; (c) schematics of cross-section of the lamellar element; and (d) resulting 3D-printed lamellar element.

#### 4.2.2 Ink Design, Mixing Procedure, and Curing

The final ink used in this work consisted of the sub- $150\text{ }\mu\text{m}$  fraction of commercially available Type I cement (ASTM C150 [11]) obtained from Buzzi Unicem, USA; deionized water; HRWRA (MasterGlenium 7700), and VMA (MasterMatrix 362). For each  $250.0$  grams of cement,  $65.2$ ,  $1.1$  and  $3.0$  grams of deionized water, HRWRA and VMA were used, respectively. A mixing and materials handling procedure using Twister Evolution Venturi vacuum mixer was previously developed by authors and was used in this work [10]. The specimens were 3D-printed and cast in a lab environment at  $18 \pm 3\text{ }^\circ\text{C}$  and  $45 \pm 5\%$  relative humidity. Immediately after printing (or casting), the specimens were placed in a curing container in which the temperature of  $18 \pm 3\text{ }^\circ\text{C}$  and the relative humidity of  $93 \pm 2\%$  (by using a saturated solution of potassium nitrate) was kept constant for 3 days when the specimens were taken out of the curing chamber for micro-CT characterization.

### 4.2.3 Micro-Computed Tomography (Micro-CT) of the Elements

In this study, a Zeiss Xradia 510 Versa XRM was utilized for microstructural characterization of both 3-days old 3D-printed and cast specimens, which allowed for an increase in the resolution of scans through a dual-stage magnification process. The microstructure of 3D-printed lamellar element and cast element was characterized using 0.4X magnification scans. This initial stage was established via geometric magnification, which involved setting distances between the source, detector, and specimen (as in conventional micro-CTs). The 3D-printed lamellar element was then assessed using 4X magnification scan to achieve a higher resolution and a closer look at the morphology of the microstructure of printed elements. This second stage was enabled by optical magnification was enabled at the detector system through scintillator and objective lenses. The lower resolution of 0.4X magnification ( $38.99 \mu\text{m}$  for cast and  $32.24 \mu\text{m}$  for lamellar element) allowed for identification and quantification of two microstructural phases (i.e., solid and pores) and the higher resolution of 4X magnification ( $4.04 \mu\text{m}$  for lamellar element) allowed identification of three microstructural phases (i.e., hydrated cement paste, anhydrous grains, and pores). A representative region of interest (ROI) encompassing two adjacent filaments and three adjacent layers was selected at the higher resolution scan to encompass a representative microstructure including an interface between the layers. The data was then used to conduct a quantitative analysis of the microstructure of cast and 3D-printed elements using image processing techniques. Dragonfly software was used for post-processing and visualization of the 2D and 3D images as well as for extraction of 2D images for image analysis.

### 4.2.4 Image Analysis

Image analysis was performed to quantify the distinct phases of the microstructure and their volumetric frequency distribution of the cast (collected during 0.4X scan) and 3D-printed lamellar element (collected during both 0.4X and 4X scan) K-means clustering has been a widely used method suitable for data clustering applications such as image segmentation [12]. This method, in contrast to conventional intensity thresholding (in which the threshold was specified by the user and applied to the image), uses intensity thresholding in a dynamic manner. In K-means clustering, the number of clusters was specified by the user and the algorithm finds the best threshold(s) to minimize the distance between the intensity of each pixel to its nearest cluster center. Therefore,

the algorithm works by considering a set of  $N$ -dimensional data points (where  $N = 1$  in case of grayscale images and  $N = 3$  in case of colored RGB [i.e., red-green-blue] images) and aims to find a set of  $K$  cluster centers in such a way that the mean squared distance from each data point to its nearest center was minimized.

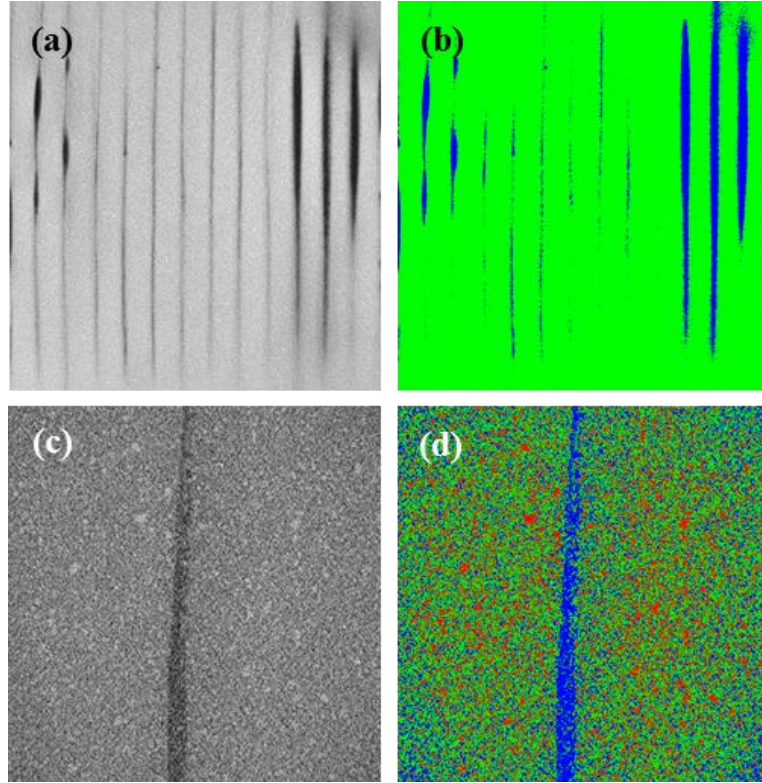


Figure 4.2. Representative visualization of applied K-means clustering segmentation algorithm to a (a) raw 2D sliced image of the entire cross section of an intact lamellar architected element (viewed in XY plane) collected during a 0.4X scan; and (b) its corresponding segmented image of 2 clusters (solid in green and pores in blue); (c) raw 2D sliced image of the entire cross section of an intact lamellar architected element (on the XY plane) collected during a 4X scan; and (d) its corresponding segmented image of 3 clusters (hydrated cement paste in green, anhydrous grains in red, and pores in blue).

In this chapter, a K-means clustering algorithm, due to its efficiency and suitability of efficient implementations, was used in the analysis of slice images. The algorithm was implemented using the Xlib plugin [13,14] of the ImageJ software [15] and was applied to 2D slices resulting in suitable segmentation of the data. Depending on the magnification used during micro-CT scans, resolution of the resulting images and identifiable phases, two clusters (i.e.,  $K=2$ )

(in case of 0.4X scans as depicted in **Figure 4.2a**) or three clusters ( $K=3$ ) (in case of 4X scans as depicted in **Figure 4.2b**) was used for segmentation. The results of segmentation were representatively shown in **Figure 4.2c,d**, for  $K=2$  and  $K=3$ , respectively. The segmented images were used for quantification of the total volume of each of the phases (i.e., clusters) of the microstructure and as well as the visualization of the range of intensities of each phase on a histogram. In-house MATLAB (The MathWorks, Inc., United States) codes were developed to compute and quantify the amount (i.e., the number of voxels of each cluster of the scanned volume) of connected components along with the volumetric frequency distribution of disconnected pore clusters. This procedure was applied to images of both 3D-printed lamellar (at 0.4X and 4X scans) and cast (at 0.4X scan) elements.

## 4.3 Results

### 4.3.1 Micro-CT Characterization of the Entire Lamellar and Cast Elements (0.4X Scan)

The quantifications of pore and solid phase of the cast and 3D-printed lamellar elements from the 0.4X magnification were presented in **Figure 4.3**. The 3D rendition of the cast and 3D-printed lamellar elements were shown in **Figure 4.3a1** and **Figure 4.3a2**, respectively. Based on the entire scanned volumes and the resolutions used ( $38.99\ \mu\text{m}$  for cast and  $32.24\ \mu\text{m}$  for 3D-printed lamellar elements), a recognizable difference can be qualitatively observed in the overall arrangement of the pores between the cast and lamellar elements. The contrast between the two microstructures was illustrated in two dimensional raw slice images of the cast (**Figure 4.3b1**) and 3D-printed elements (**Figure 4.3b2**) as well as their corresponding segmented images (**Figure 4.3c1** and **Figure 4.3c2**) analyzed using the K-means clustering technique. This approach resulted in quantification of the intensities of the pore and solid phase for cast and printed elements as illustrated in **Figure 4.3d1** and **Figure 4.3d2**, respectively. The total volumes of pores and solid phase in the cast and 3D-printed lamellar elements as shown in **Figure 4.3e1** and **Figure 4.3e2**, respectively. The total amount of porosity was found to be higher (3.5%) in the 3D-printed element compared to the cast counterpart (0.9%), as viewed in **Figures 4.3.d1-e2**. The volumetric frequency distribution of the pore phase (obtained from the entire volume) of the cast and 3D-printed elements were shown in a frequency plot in **Figure 4.3f**, revealing the volume of each connected pore pockets versus their corresponding frequency. The ‘connected pore pockets’

demonstrated at any given data point in **Figure 4.3f** represents the volume of the voxels of every pore pocket that were connected to one another and isolated from the other pockets.

The frequency plot shown in **Figure 4.3f** demonstrates that a wide range of porosity from small pores ( $< 10^7 \mu m^3$ ) with very high frequencies ( $>10^1 - 10^5$ ) to large pores ( $>10^8 \mu m^3$ ) with very small frequency ( $=1$ ) resides in microstructures of both cast and 3D-printed lamellar elements. However, the two microstructures were dissimilar in that (i) the largest pores (specifically the first 20 large pores) of 3D-printed element was larger the largest pores of the cast element and (ii) the frequency of small pores in the 3D-printed lamellar element was smaller compared to the cast element (**Figure 4. 3f**).

To clarify the former, the first ten largest pore volumes with single frequencies can be compared, as pointed out with blue and black arrows for the 3D-printed lamellar and cast elements respectively in the bottom right corner of **Figure 4.3f**. More specifically, the largest pore volume of the 3D-printed element holds a volume of  $29.09 mm^3$ , where the largest pore volume of the cast element begins to appear only occupy  $3.98 mm^3$ , indicating that the largest pore volume of the 3D-printed lamellar element was more than 7 times larger than the largest pores of the cast element. To clarify the latter, the smallest pore volume of the 3D-printed lamellar element ( $31246 \mu m^3$ ), with the frequency of  $1.07 \times 10^5$  can be compared the smallest pore volume of the cast element ( $54340 \mu m^3$ ) as shown by dashed arrows on the left-hand side of the **Figure 4.3f**. At the constant and highest frequency, the 3D-printed lamellar element inhabit pore volumes smaller in size compared to that of the cast element. This contrast does not only exist at the highest frequencies. The cast and 3D-printed elements each contained relatively close number of individual isolated pore pockets (i.e., 541 in the cast and 525 in the 3D-printed lamellar element) represented by the number of data points in **Figure 4.4g**. This data indicated the continuity and intermix of the pore phase was similar in the hardened microstructure of the cast and 3D-printed lamellar element. However, the distribution of the isolated individual pore volumes shown in the frequency plot data points (**Figure 4.3f**) importantly marks the contrast in the range of pore volumes in 3D-printed lamellar (between of  $29.09 mm^3$  to  $31245 \mu m^3$ ) and cast (between  $3.98 - 54340 \mu m^3$ ) elements.

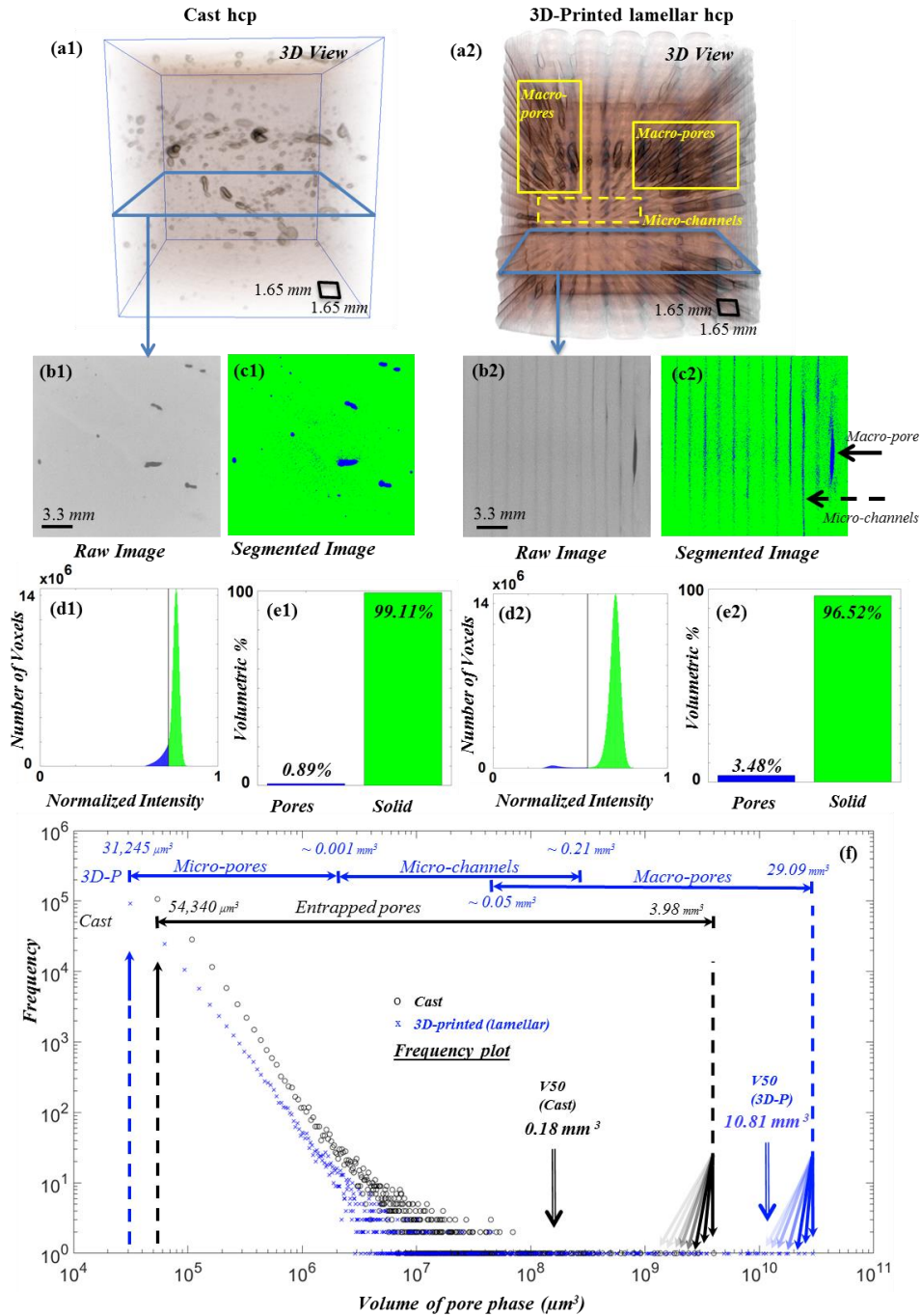


Figure 4.3. Comparison of the microstructure and quantification of phases in the entire cast (a1-e1,f) and 3D-printed lamellar (a2-e2,f) hardened cement paste elements using 588 and 714 slices captured during a 0.4X CT scan, respectively: (a1,a2) three-dimensional rendition of the entire volume of the elements; (b1,b2) two typical raw slice images; (c1,c2) two typical slice images processed using K-means segmentation technique; (d1,d2) histograms of pore (blue), and solid (green) phases; (e1,e2) total volumetric percentages of pore and solid phases; and (f) frequency plot of pore phases (frequency of given pore volume) of the entire volume of the elements.

**Figure 4.3e1,e2** demonstrates that about 3.5 % and 0.9% of volumes of, respectively, 3D-printed and the cast elements was occupied by pores. Majority of these pores in both elements were occupied by relatively infrequent larger pores as shown at the right-hand side of **Figure 4.3f**. More precisely, the analysis of frequencies of appearance shows that the pores with a frequency of 1 make up 96.16% of total pore volume in 3D-printed lamellar element whereas they only make up 64.88% of the total pore volume in cast elements. Such dissimilarities in the microstructure of 3D-printed lamellar and cast elements indicate that the 3D-printing process reduces the amount of very small pores (i.e., micro-pores) in the hcp compared to traditional casting process. This may be due to the expulsion of air bubbles to the surface of the materials during the pressurization in the syringe and/or during the extrusion at the tip of nozzle. Since there was a higher population of those pores in the 3D-printed elements at the vicinity of the interfacial regions (see **Figure 4.3c2**), it is also likely that smaller pores could have coalesced to form slightly larger pores, a phenomenon that is less likely to occur during the casting process.

To compare the median values of pore volumes in 3D-printed and cast elements (**Figure 4.3f**), a ‘ $V_{50}$ ’ was considered. The data was analyzed considering  $V_{50}$  volume, defined as the pore volume up to which the sum of the pore volumes (from either end of frequency plot) were equal. In this analysis, the first 9 large pore volumes of the 3D-printed element occupied a cumulative volume of  $176.95 \text{ mm}^3$  (which was equal to the total volume occupied by the remaining 516 pores of smaller volumes). The median values of pore volume for these two groups was  $V_{50} = 10.81 \text{ mm}^3$ . On the other hand, the 48 largest pores of the cast elements occupied only  $37.75 \text{ mm}^3$  (which was equal to a cumulative volume occupied by the remaining 493 smaller pores). The corresponding median values of pore volume for these two groups was  $V_{50} = 0.18 \text{ mm}^3$ . The two median values of pore volumes ( $V_{50}$ ) for the 3D-printed and cast elements are shown in **Figure 4.3f** as two thick blue and black double line arrows. To put the differences in pore volumes in perspective, it takes the total volume of the 19 largest pores in the cast element to equate the volume occupied by the single largest pore in the lamellar element. The comparison of the small, large, and median pore volumes of the 3D-printed and cast elements discussed here is also summarized in **Table 1**.

Table 4.1. Comparison of the pore volumes of 3D-printed (lamellar) element and cast element based on the frequency plot presented in Figure 4.3f, collected during a 0.4X magnification.

<b>0.4X Magnification</b>	<b>3D-Printed Lamellar</b>	<b>Cast</b>
Largest pore	29.09 mm <sup>3</sup>	3.98 mm <sup>3</sup>
Smallest pore*	$3.12 \times 10^{-5}$ mm <sup>3</sup>	$5.43 \times 10^{-5}$ mm <sup>3</sup>
Frequency of pore with largest volume	1	1
Frequency of pores with smallest volume	$9.21 \times 10^4$	$1.07 \times 10^5$
V <sub>50</sub>	10.81 mm <sup>3</sup>	0.18 mm <sup>3</sup>

\*pores smaller than this volume cannot be seen due to limitations in the resolutions of the instrument at 0.4X magnification

#### 4.3.2 Analysis of the Categories of Pores in 3D-Printed Lamellar Element (0.4X Scan)

Three categories of pores (i.e., macro-pores, micro-channels, interfacial micro-pores) have been previously reported by authors [7] and are schematically illustrated in **Figure 4.4**. However, the volumetric distribution of these pores was unclear. To identify volumes of these three categories of pores in view of the volume frequency distribution presented in **Figure 4.3.f**, further analysis was conducted.

Macro-pores were previously discussed to appear in the form of visible gaps between the filaments (with a width larger than 100  $\mu\text{m}$ ), which resulted from inconsistencies during the 3D-printing process such as thinning of the filaments) [7]. The macro-pores were marked in two yellow boxes shown in **Figure 4.3.a2** and identified by the black solid arrow in 2D image in **Figure 4.3.c2**. From the geometrical measurements conducted on the slice images obtained from micro-CT, the largest and smallest macro-pores can be roughly estimated to have the width varying from about 100  $\mu\text{m}$  to 800  $\mu\text{m}$ , the height varying from 500  $\mu\text{m}$  to 1500  $\mu\text{m}$ , a length varying from 1000  $\mu\text{m}$  to 17,000  $\mu\text{m}$ . These dimensions correspond to estimated volumes in the range between 0.05  $\text{mm}^3$  and 20.40  $\text{mm}^3$ , respectively. The upper bound of this estimation (20.40  $\text{mm}^3$ ) was lower than the volume of the largest pore, quantified from image analysis (29.09  $\text{mm}^3$ ). Since the volume obtained from the image analysis was considered to be more accurate, that volume was taken as the upper bound for the volume of macro-pores. The upper bound and lower bound of the volume of the

macro-pores are shown as labels placed over the horizontal arrows located at the top of the **Figure 4.3f**.

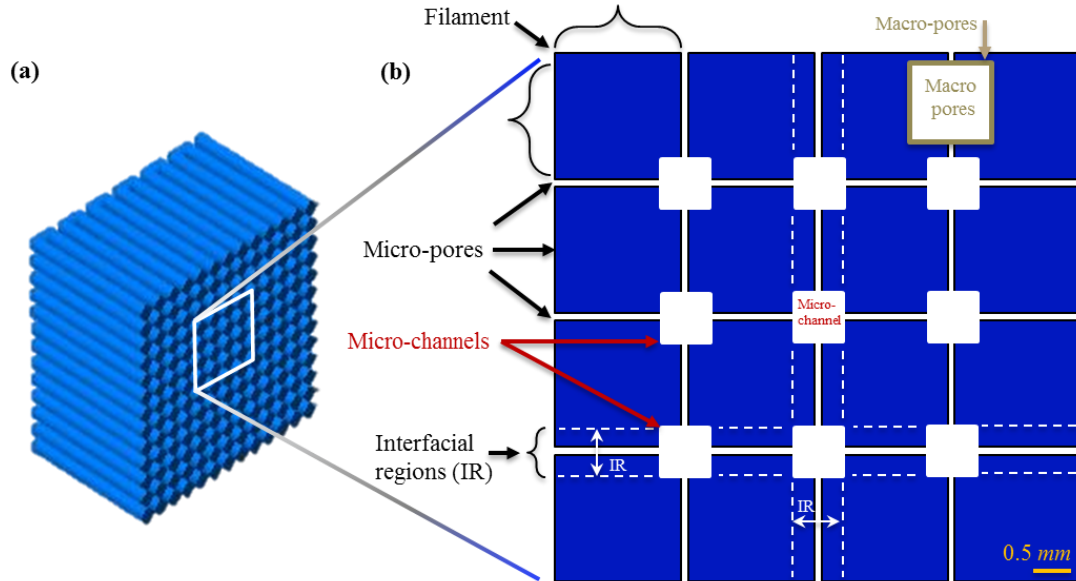


Figure 4.4. (a) schematics of the arrangement of filaments in the cross-section of the lamellar element and (b) Visualization of representative examples of macro-pores, micro-channels, micro-pores, and interfacial regions.

Micro-channels have been previously discussed [7] as the pores present between at the interface between the adjacent filaments (i.e., at the interfacial regions) and oriented along the length of the filaments as indicated by the black dashed arrow shown in **Figure 4.3c2**. From the geometrical measurements conducted on slice images, it is known that micro-channels had a typical width and height of up to  $100 \mu m$ . Assuming such square cross-section, and a length varying between the entire length of the lamellar element ( $25000 \mu m$ ) down to a very small length on the order of  $100 \mu m$  (based on the measured width for a typical micro-channel), the pore volume occupied by the largest micro-channel can be estimated to be between  $0.001 mm^3$  to  $0.25 mm^3$ . This analysis provides the range of the pore volumes associated with micro-channels as shown over the top arrows by the labels placed above the horizontal arrows located at the top of **Figure 4.3f**.

As discussed in this chapter, the interfacial micro-pores are considered to be isolated pores (located at the interfacial regions) smaller than micro-channels that were identifiable at the

achievable resolutions provided by 0.4X magnification (38.99  $\mu m$  for cast and 32.24  $\mu m$  for lamellar elements). To locate the range of pore volumes at which micro-pores reside in the frequency plot based on the 0.4X magnification, the pores smaller than 0.001  $mm^3$  (which was the lower bound of estimated pore volume of micro-channels) was taken as the upper bound. The lower bound of volume of micro-pores was taken from the actual smallest pore volume identifiable from image analysis ( $3.12 \times 10^{-5} mm^3$  equal to 31246  $\mu m^3$ ). This analysis provides the pore volume range at which micro-pores can be present at the given frequency as shown over the top arrows by the labels placed above the horizontal arrows located at the top of **Figure 4.3f**. The analysis of the three pore types and their corresponding range of volumes in the 3D-printed lamellar element is also summarized in **Table 4.2**.

Table 4.2. Analysis of the pore types and their corresponding range of volumes in 3D-printed (lamellar) element and cast element based on the frequency plot presented in Figure 4.3f, collected during 4X magnification

<b>3D-Printed Lamellar Element (4X Magnification)</b>	<b>Largest Volume</b>	<b>Smallest Volume</b>
Macro-pore volume range	29.09 $mm^3$	$5 \times 10^{-2} mm^3$
Micro-channel volume range	$2.5 \times 10^{-1} mm^3$	$1 \times 10^{-3} mm^3$
Micro-pore volume range	$1 \times 10^{-3} mm^3$	$3.12 \times 10^{-5} mm^3$

It must be noted that, interfacial micro-pores are difficult to identify and quantify using 4X magnification data. Further details regarding interfacial micro-pores are discussed in section 4.3.3. However, it must be noted here that ‘interfacial’ micro-pores in the 3D-printed lamellar element (as will be confirmed in **Figure 4.5**) prevalently resided in interfacial regions at high amounts (due to the formation of lubricating layer) [7]. However, micro-pores can also be present in the bulk part of the material (i.e., within the filaments). This type of micro-pore were the isolated pores that can exist throughout the filament of hcp microstructure away from interfacial regions. In this chapter the term ‘interfacial micro-pores’ specifically refers to the micro-pores present at the interfacial regions, and the term ‘micro-pores’ generally refers to both types of pores near the interfacial regions or in the filaments. The fact that micro-pores resided in interfacial regions have already been qualitatively described in chapter two and attributed to the formation of lubricating

layer. This lubricating layer exists at the exterior of the filaments due to the formation of water-rich layer. Therefore, this process can leave behind larger amounts of porosity at the interfacial regions, upon evaporation of water during 3D-printing and upon solidification as compared to the core of the filament. The authors have previously hypothesized about the connectivity between the micro-channels and surrounding interfacial micro-pores [7]. A qualitative analysis of the tomography data with 4X magnification is further discussed in section 4.3.3.

### **4.3.3 Micro-CT Characterization of a Region of Interest (ROI) in 3D-Printed Lamellar Element (4X Scan)**

To examine the connectivity between the micro-channels and interfacial micro-pores, the quantifications of pore and solid phases (hydrated and anhydrous) at a region of interest (ROI) in the 3D-printed lamellar element was investigated using 4X magnification tomography data (**Figure 4.5**). The 3D volume of rendition of the entire 3D-printed lamellar element is shown in **Figure 4.5a**. From this volume, a cylindrical ROI containing 2 adjacent filaments stacked in multiple layers was selected for a 4X scan corresponding to the resolutions of  $4.04 \mu m$  (**Figure 4.5b**). Quantitatively, a discernable connectivity between the micro-channels at the interfacial regions of filaments was noticeable as previously discussed by authors in detail [7]. Within the scanned ROI, a cubical volume of  $1.65 \times 1.65 \times 1.65 \text{ mm}$  was selected for conducting image analysis (as shown in red cube in **Figure 4.5b**). The cubical volume contained one micro-channel at the interfacial region in the middle of the cube and it is bound by the mid-planes of the adjacent filaments throughout the width and height (i.e., it is bound by the planes located at the centers of the core of the filaments). This cubical volume was selected in way that included a micro-channels and surrounding interfacial micro-pore (i.e., micro-pores located at the interfacial regions), and excluded macro-pores. A 2D view of a typical cross-section of the cubical volume is illustrated in raw slice image shown in **Figure 4.5c**. Using K-means segmentation technique resulted in quantification of the intensities of the three distinct phases (i.e., pores, hydrated solid, and unhydrated solid) in the cubical volume within ROI as illustrated in **Figure 4.5e**. Hardened cement paste was composed of many crystalline phases including both unreacted phases and agglomerated hydration products (calcium–silicate–hydrate gel and calcium hydroxide) [17]. Due to limited resolution of the instrument used in this study, it was not possible to identify the individual hydration products. The total volume of the pore phase, hydrated phases, unhydrated cement grains

was analyzed (**Figures 4.5f**). The result of this analysis revealed the following volumes of pores = 26%, hydrated = 51%, and unhydrated cement = 23%. It should be noted, however, that the reported porosity (26%) contains pores located at both, the interfacial regions and inside the filaments.

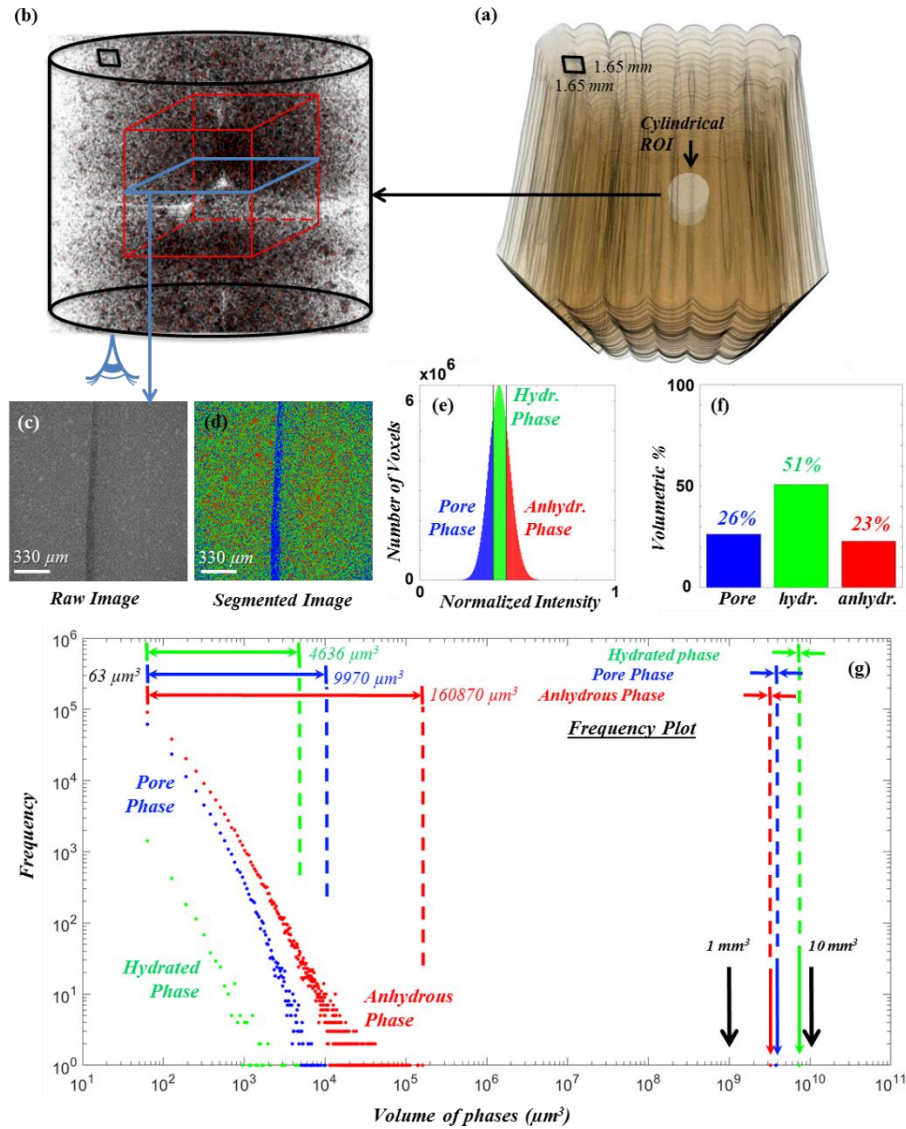


Figure 4.5. Quantification of phases of the microstructure of a representative region of interest of intact 3D-printed lamellar hardened cement paste element using 403 slices captured during a 4X CT scan: (a) three-dimensional rendition of the entire volume of the element; (b) three-dimensional rendition of representative region of interest (ROI); (c) a typical raw slice image from the representative region; (d) a typical slice image processed using K-means segmentation; (e) histogram of pore (blue), hydrated (green), and anhydrous (red) phases; (f) volumetric percentage of each phase; and (g) Frequency plot (frequency of given pore volume) of the entire representative region (i.e., sliced images).

Even more important, was the volumetric frequency distribution of all three phases as shown in the frequency plot in **Figure 4.5g**. In this figure, every data point represents the frequency of voxels associated with each of the connected phases. These voxels are isolated from the voxels representing other pockets of the corresponding phases. It can be briefly summarized that the left-hand side of the frequency plot contains the smaller and more frequent volumes of each phase, whereas the right-hand side contains single connected volume of each phase. In other words, the frequency plot shown in **Figure 4.5g** demonstrates that in each case, there was consistently one very large connected volume, presented by one single data point on the right-hand side of the frequency plot, and smaller isolated volumes, presented by high-frequency data points on the left-hand side. As shown with the green, blue, and red vertical solid arrows located at the bottom right position of **Figure 4.5g**, one large connected volume of each phase (pore, hydrated, and anhydrous) was singled out and resided between  $1 \text{ mm}^3$  to  $10 \text{ mm}^3$  on the volume axis. This single large volume as shown in **Figure 4.5g**, corresponds to  $7.36 \text{ mm}^3$  hydrated phase (shown in green),  $3.79 \text{ mm}^3$  pore phase (shown in blue), and  $3.23 \text{ mm}^3$  anhydrous phase (shown in red). These single large volumes make up almost the entire total volume of corresponding phases. Specifically, 99.99%, 99.34%, and 97.42% of the hydrated phase, pore phase, and anhydrous phase were composed of the one single largest volume mentioned above. As can be viewed on the X-axis of **Figure 4.5g**, the 2<sup>nd</sup> largest pore volume was 4, 5, and 6 orders of magnitude smaller than of the largest pore volume of the anhydrous, pore, and hydrated phases, respectively. These data indicate the presence of one large connected volume of each phase. **Table 4.3** contains the summary of the comparison of the largest and smallest volumes of each phase based on the frequency plot presented in **Figure 4.5g**.

Other than the volume frequency distribution, the number of isolated pockets of each phase (i.e., the number of points in each phase in **Figure 4.5g**) also revealed interesting information. The pore, hydrated, and anhydrous phases, each contained 102, 34, and 479 individual isolated pockets (as represented by the number of data points of each phase shown in **Figure 4.5g**). The smaller the number of isolated pockets, the more continuous the phase is. Therefore, the number of individual isolated pockets provide a measure of the continuity and intermix of each phase of the hardened microstructure. Also, the smallest detected individual isolated volume at 4X magnification was equal to the smallest voxel size of  $63.50 \mu\text{m}^3$ . The frequency analysis of each phase at this voxel

size demonstrated that the anhydrous phase (90936 grains) has the highest frequency followed by the pore phase (61628 pore pockets) and hydrated phase (1420 hydrated pockets).

Table 4.3. Comparison of the range of volumes of three microstructural distinct phases based on the frequency plot presented in Figure 4.5g.

<b>3D-Printed Lamellar Element (4X ROI)</b>	<b>Largest Volume</b>	<b>Smallest Volume</b>
Pore phase	29.09 mm <sup>3</sup>	5 × 10 <sup>-2</sup> mm <sup>3</sup>
Hydrated phase	2.5 × 10 <sup>-1</sup> mm <sup>3</sup>	1 × 10 <sup>-3</sup> mm <sup>3</sup>
Anhydrous Phase	1 × 10 <sup>-3</sup> mm <sup>3</sup>	3.12 × 10 <sup>-5</sup> mm <sup>3</sup>

From the total number of isolated pockets and the frequency of each phase (**Figure 4.5g**) we can infer that the studied systems contained higher quantities of continuous hydrated phase compared to that of pore phase and unhydrated cement phase. That inference is based on the fact that there were fewer isolated pockets in the scanned volume of hydrated phase compared to pore phase. Specifically, more continuity was observed in the pore phase as compared to the anhydrous phase. It was expected that the hydrated phase will be continuous throughout the microstructure, including the interface. Similarly, it is intuitively expected that the pore phase, especially in areas containing micro-channels and surrounding interfacial micro-pores, will be more continuous and connected than the unhydrated grains. This was expected as it was known the hydration progresses from the surface of the unhydrated grains inward and the fact that the 3D-printed hcp element was scanned at relatively early ages of hydration (only 3-days old, and thus contained many capillary pores left behind by evaporated water). Although the unhydrated phase shows less continuity throughout the microstructure compared to porous and hydrated phases, it was not expected that 97% of it fall into single connected volume. Most of such expectation were based on conventional two-dimensional investigations of hcp microstructure obtained by techniques such as SEM [18]. In this investigation, the additional (third) dimension was captured via micro-CT observations performed at magnification of 0.4X. The presence of large connected volume of unhydrated phase reveals that the majority of cement grains were interconnected in three dimensions, at least at the available resolution (i.e., 4.04 μm). Therefore, it can be concluded that the presence of a very low-

frequency (i.e., one) large connected volume for each of the phases (in contrast to the presence of isolated high-frequency smaller pore volumes) shown in **Figure 4.5g** indicates the continuity and intermixing of all three phases in three dimensions.

It must be noted that the volumetric range at which the majority of the isolated volumes of each phase (other than the largest single volumes of each phase exist), was also different between the three phases as indicated by the top arrows shown in **Figure 4.5g**. While the lower bound of this range was limited by the resolution, the upper bound varies significantly between the phases, further indicating the higher levels of homogeneity and intermix in the hydrated phase and lower levels of continuity in the anhydrous phase discussed above. The difference in the frequencies between the three phases reveals the same information as the **Figure 4.5g** frequency plot – i.e., that small anhydrous grains exist at higher frequencies compared to pore pockets, and both anhydrous and pore pockets were present at much higher frequencies than hydrated pockets. This was intuitive and also further verifies the hypothesis that there would be more continuity in the hydrated phase than in the pore and anhydrous phase.

Most importantly, in the case of pore phase, the presence of a single large pore indicates that the micro-channels (illustrated in **Figure 4.3b2,c2** based on the data obtained from the 0.4X scan of the entire volume of lamellar element) were found interconnected to one another (at this given resolution) through the micro-pores present at the interfacial regions.

Pore volume occupied 26% of the total volume of the cubical element within ROI. From this 26%, about 99.34% (i.e., 25.82%) makes up a single connected pore volume equal to  $3.79 \times 10^9 \mu\text{m}^3$ . As shown by previous qualitative analysis of representative ROI [7], this region contained both a micro-channel and micro-pores. One can speculate about the interconnectivity between the micro-channels through the presence of interfacial micro-pores. However, in order to quantitatively prove such interconnectivity, the connectivity between micro-channel and the interfacial micro-pores must be first proven. Using geometrical measurements performed on the 2D images. One can reasonably assume an average width  $100 \mu\text{m}$  for both the micro-channel and the surrounding interfacial micro-pores. Given the height and depth of the analyzed cubical volume within ROI (i.e.,  $1650 \mu\text{m} \times 1650 \mu\text{m}$ ), a ‘connected’ vertical pore volume of  $0.27 \times 10^9 \mu\text{m}^3$  at the interface can be estimated. A similar analysis can be done on the ‘connected’ horizontal pores resulting in a volume of  $0.27 \times 10^9 \mu\text{m}^3$ . Therefore, a ‘connected’ pore interfacial volume of  $0.54 \times 10^9 \mu\text{m}^3$  is estimated and is occupied by micro-channel and surrounding interfacial micro-pores.

This volume, occupied by the micro-channel and surrounding interfacial micro-pores ( $0.54 \times 10^9 \mu\text{m}^3$ ) was still relatively smaller compared to the single connected pore volume obtained from image analysis ( $3.79 \times 10^9$ ). In other words, assumptions of more-or-less realistic dimensions for the micro-channel and interfacial micro-pores resulted in an overall volume of the pores being lower than the volume of a single connected pore obtained from image analysis. Based on these discrepancies, conclusions can be reasonably drawn as follow: (i) the micro-channel and micro-pores (present at the surrounding interfacial regions) that were assumed to be connected are indeed connected. In other words, because (as shown in **Figure 4.5g**) there are no data points that can represent the single micro-channel contained in the analyzed cubical element, we can deduce that the connectivity between micro-channel and the interfacial micro-pores is proven. Beyond that, we can also conclude that (ii) the micro-channel interconnected with the surrounding interfacial micro-pores were to some degree also connected to the pores inside the filament. Supporting the second conclusion requires further analysis of the microstructural characteristics of the filament alone. The presence of wider range of pores on the left-hand-side of **Figure 4.5g**, also implies that the certain pores inside the filaments (as can be seen as the blue dots in **Figure 4.5d**) were isolated from the interconnected micro-channel and surrounding interfacial micro-pores. Therefore, based on the cubical volume analyzed, the micro-channels were demonstrated to be interconnected through the macro-pores present at the interfacial regions. Also, due to the random and arbitrary selection of the location of the ROI, it can be concluded that the entire volume of the material located outside of the analyzed cubical volume is interconnected through the porosity located between the micro-channels.

Due to limits of the magnification of micro-CT imaging it can be expected that there were pores that could not be detected at this resolution ( $4.04 \mu\text{m}$ ) and that seemingly disconnected pore pockets could indeed be interconnected.

#### 4.4 Summary and Conclusion

This chapter presents, the results of quantitative evaluation of the microstructure of 3-days-old 3D-printed hardened cement paste element with lamellar architecture. The data used in the analysis were generated using an XRM operated at two magnifications (0.4X and 4X). These magnifications yield resolutions of corresponding to  $\sim 32.24\text{-}38.99 \mu\text{m}$  and  $4.04 \mu\text{m}$ , respectively. The 3D-printed element demonstrated a significantly dissimilar pore volume distribution and

morphology, the result of the 3D-printing process. The porosity in 3D-printed lamellar element (including macro-pores, micro-channels, and interfacial micro-pores) was found to be preferentially aligned with the printing pattern (i.e., orientation of filaments) and was highly heterogeneously distributed. This type of porosity was distinctively different from the spherical pores with a random distribution observed in the microstructure of cast element. The larger pores of the 3D-printed element were found to be larger than the largest pores of the cast element. Furthermore, the smallest pores of the 3D-printed element were found to be less frequent than similar pores in cast element. The analysis of the frequencies shows that the pores with a frequency of 1 make up 96.16% of total pore volume in 3D-printed lamellar element whereas the pores with a frequency of 1, only make up 64.88% of the total pore volume in cast elements. This finding indicates that the connected pore network makes up the majority of the total quantifiable porosity present in the entire 3D-printed lamellar element. The three categories of pores (i.e., macro-pores, micro-channels, and interfacial micro-pores) were found to reside in three distinct pore size domains.

Analysis of microstructure at higher (i.e., 4X) magnification of a ROI indicated that the micro-channels were connected to one another through the macro-pores present at interfacial regions. These two make up the majority of the total porosity (99.34%) observed at this magnification, The rest of the porosity consisted of the individual isolated pores that exist inside the filaments. Therefore, it can be concluded that the entire microstructure of 3D-printed lamellar elements consists of a connected porous network.

In summary, the 3D-printed elements created via the DIW process contain unique patterned and interconnected pore network. The presence of such connected network may offer the opportunity to control the mechanical response of the brittle elements by changing the pattern (orientation) of the region of high porosity. Specifically, the locally weaker regions may facilitate the formation and spread of the cracks and microcracks, thus postpone or even prevent formation or coalescence of a single crack, and resulting brittle behavior. The question remains how to achieve isotropic mechanical response and to ensure the durability of elements containing preferentially oriented network of pores.

## 4.5 Acknowledgments

I gratefully acknowledge the generous support of this research by the National Science Foundation (CMMI Grant 1562927). I would also like to thank the BASF chemicals company for providing materials. I would also like to thank the 2017 Major Multi-User Equipment Program, offered by the Office of the Executive Vice President for Research at Purdue University, for supporting the acquisition of the X-ray microscope (micro-CT) used in data reviewed in this research.

## 4.6 References

- [1] V. Mechtcherine, F.P. Bos, A. Perrot, W.R. Leal, V.N. Nerella, S. Fataei, R.J.M. Wolfs, M. Sonebi, N. Roussel, Cement and Concrete Research Extrusion-based additive manufacturing with cement-based materials – Production steps , processes , and their underlying physics : A review, *Cem. Concr. Res.* 132 (2020) 106037. doi:10.1016/j.cemconres.2020.106037.
- [2] T. Wangler, N. Roussel, F.P. Bos, T.A.M. Salet, R.J. Flatt, Cement and Concrete Research Digital Concrete : A Review, 123 (2019). doi:10.1016/j.cemconres.2019.105780.
- [3] T. Wangler, R.J. Flatt, First RILEM International Conference on Concrete and Digital Fabrication – Digital Concrete, 2018.
- [4] B.N. Sanjayan, Jay G., Ali Nazari, ed., 3D Concrete Printing Technology: Construction and Building Applications, Butterworth-Heinemann, 2019.
- [5] S. Lim, R.A. Buswell, T.T. Le, S.A. Austin, A.G.F. Gibb, T. Thorpe, Developments in construction-scale additive manufacturing processes, *Autom. Constr.* 21 (2012) 262–268. doi:10.1016/j.autcon.2011.06.010.
- [6] J.D. Silva, W.R. Leal de, S.Z. Jones, 3D printing using concrete extrusion: a roadmap for research, *Cem. Concr. Res.* (2018) (this issue). doi:10.1016/j.cemconres.2018.05.006.
- [7] M. Moini, J. Olek, B. Magee, P. Zavattieri, J. Youngblood, Additive Manufacturing and Characterization of Architected Cement-based Materials via X-ray Micro-Computed Tomography, in: 1st Rilem Int. Conf. Concr. Digit. Fabr., 2018.

- [8] Y.W.D. Tay, G.H.A. Ting, Y. Qian, B. Panda, L. He, M.J. Tan, Time gap effect on bond strength of 3D-printed concrete, *Virtual Phys. Prototyp.* 0 (2018) 1–10. doi:10.1080/17452759.2018.1500420.
- [9] J. Van Der Putten, *The Effect of Print Parameters on the ( Micro ) structure of 3D Printed Cementitious Materials*, Springer International Publishing, 2019. doi:10.1007/978-3-319-99519-9.
- [10] T. Marchment, J. Sanjayan, M. Xia, Method of enhancing interlayer bond strength in construction scale 3D printing with mortar by effective bond area amplification, *Mater. Des.* 169 (2019) 107684. doi:10.1016/j.matdes.2019.107684.
- [11] ASTM C150 – Standard Specification for Portland Cement (2017), (n.d.).
- [12] A.Y.W. T. Kanungo, D.M. Mount, N.S. Netanyahu, C. Piatko, R. Silverman, An Efficient K-means Clustering Algorithm: Analysis and Implementation, *IEEE Trans. Pattern Anal. Mach. Intell.* 24 (2002) 411–426.
- [13] B. Münch, L.H.J. Martin, A. Leemann, Segmentation of elemental EDS maps by means of multiple clustering combined with phase identification, *J. Microsc.* 260 (2015) 411–426. doi:10.1111/jmi.12309.
- [14] No Title, (n.d.). <https://imagej.net/Xlib>.
- [15] C.A. Schneider, W.S. Rasband, K.W. Eliceiri, NIH Image to ImageJ: 25 years of image analysis, *Nat. Methods.* 9 (2012) 671–675. doi:10.1038/nmeth.2089.
- [16] M. Choi, N. Roussel, Y. Kim, J. Kim, Lubrication layer properties during concrete pumping, *Cem. Concr. Res.* 45 (2013) 69–78. doi:10.1016/j.cemconres.2012.11.001.
- [17] H. Manzano, J.S. Dolado, A. Ayuela, Elastic properties of the main species present in Portland cement pastes, *Acta Mater.* 57 (2009) 1666–1674. doi:10.1016/j.actamat.2008.12.007.
- [18] K.L. Scrivener, Backscattered electron imaging of cementitious microstructures: Understanding and quantification, *Cem. Concr. Compos.* 26 (2004) 935–945. doi:10.1016/j.cemconcomp.2004.02.029.

## 5. ADDITIVE MANUFACTURING AND PERFORMANCE OF ARCHITECTURED CEMENT-BASED MATERIALS

This chapter contains work that was originally published in the *Advanced Materials Journal* as “Moini, Mohamadreza, Jan Olek, Jeffrey P. Youngblood, Bryan Magee, and Pablo D. Zavattieri. *Additive Manufacturing and Performance of Architected Cement-Based Materials. Advanced Materials* 30, no. 43 (2018): 1802123.” The original article has been reproduced in this chapter with permission from the publisher with partial modifications to include the supplemental information of the published article. A paragraph is added to the end of the manuscript to further elaborate on work-of-failure. The original article has also been modified for dissertation formatting purposes. Moreover, this chapter contains experimental data collected by Mohamadreza Moini. Data conceptualization was a collaborative effort with co-authors, Jan Olek, Jeffrey P. Youngblood, B. Magee, and Pablo D. Zavattieri. The manuscript was written by Mohamadreza Moini and Jan Olek, Jeffrey P. Youngblood, B. Magee, and Pablo D. Zavattieri provided editing.

### Abstract

There is an increasing interest in hierarchical design and additive manufacturing (AM) of cement-based materials. However, the brittle behavior of these materials and the presence of interfaces from the AM process currently present a major challenge. Contrary to the commonly adopted approach in AM of cement-based materials to eliminate the interfaces in 3D-printed hardened cement paste (hcp) elements, this work focuses on harnessing the heterogeneous interfaces by employing novel architectures (based on bioinspired Bouligand structures). These architectures were found to generate unique damage mechanisms which allow inherently brittle hcp materials to attain flaw-tolerant properties and novel performance characteristics. It is hypothesized that combining heterogeneous interfaces with carefully designed architectures promotes such damage mechanisms as, among others, interfacial microcracking and crack twisting. This, in turn, leads to damage delocalization in brittle 3D-printed architected hcp and therefore results in quasi-brittle behavior, enhanced fracture and damage tolerance, and unique load-displacement response, all without sacrificing strength. It was further found that in addition to delocalization of the cracks, the Bouligand architectures can also enhance work of failure and

inelastic deflection of the architected hcp elements by over 50% (when compared to traditionally cast elements from the same materials).

**Keywords:** Architected materials, Direct-ink-writing, Hardened cement paste, Interfaces, Mechanical response

## 5.1 Manuscript

There is a rising interest in hierarchical design and additive manufacturing (AM) of architected materials due to their ability to achieve unique and novel performance characteristics [1-8]. AM allows for engineering and fabrication of a vast array of metallic, ceramic, polymeric, composite, and hydrogel materials into complex solid and cellular structures and assists us in the understanding of the structure-property relationship [9-23]. It has been established that AM of metallic [9,10], polymeric [11-13], hydrogel [14], and ceramic [15] materials introduces microstructural heterogeneities, such as porosity and interfaces, which can result in anisotropy in the mechanical response of the elements. For instance, in case of ceramic and metallic materials, the resulting anisotropic mechanical properties are demonstrated to be similar, lower, or higher, compared to the conventionally cast counterparts and depending on the printing directions, the type of applied AM techniques and mechanical property of interest [9-14]. Currently, there are two approaches towards enhancement of the mechanical response of additively manufactured materials: a) elimination of detrimental heterogeneities such as porosities and interfaces present in fabricated metallic [9,10], ceramic [15], and hydrogel materials [14] via optimizing the printing parameters in order to achieve performance comparable to cast counterpart and; b) incorporation of multi-scale [13], hierarchical [16], and bioinspired [17] design principles over a broad range of architectures of fabricated materials, from nano [18] to micro [19,20] in order to engineer the mechanical properties [19], to significantly enhance the strength and tensile performance [13], load-bearing capacity, compliancy, and impact resistance [16], and to overcome the brittleness and flaw-sensitivity limitations of these materials [18,20]. Similar to the trends observed in additively manufactured materials [9-14], the presence of weak interface is considered detrimental for the overall mechanical performance of additively manufactured cement-based materials, and current research efforts focus mostly on eliminating or strengthening the AM-induced interfaces as a mean to minimize their effect on the overall strength, bearing capacity to improve stress transfer across the interfaces in 3D-printed elements [24-28]. Contrary to the common approach that suggests elimination of the

processing-induced interfaces in various materials <sup>[10,11,15]</sup>, we present a novel approach that combines harnessing the properties of heterogeneous interfaces with the design of materials' architecture that can promote favorable damage mechanisms, allows for achievement of flaw tolerance and unique load-displacement response, and enhances the mechanical response in brittle cement-based materials. The focus of this work is on 3D-printing of brittle cement-based materials, in which the ability to control the internal architecture of the structure at the macroscopic level (i.e., mm scale) may play a significant role by enabling novel performance characteristics, such as a quasi-brittle mechanical behavior, fracture and damage tolerance, unique load-displacement response, and enhanced flexural strength. Materials with such enhanced properties may impact design approaches, processes, and products in several industries <sup>[29,30]</sup>.

Despite recent works on processing <sup>[31-33]</sup>, and characterization of mechanical performance <sup>[24-28]</sup> of 3D-printed cement-based materials, as well as earlier works on microstructural aspects of fracture properties of hcp, <sup>[34-36]</sup> there are only limited studies that highlight control of the mechanical behavior through the architectural design of the materials <sup>[37,38]</sup>. Due to its intrinsic properties, the cast hardened cement paste (hcp) does not exhibit typical toughening mechanisms, e.g., crack branching, observed in other materials. <sup>[36,39-41]</sup> Correspondingly, cast cement paste behaves as a brittle material and does not show non-linear post-peak load-displacement behavior <sup>[42]</sup>. However, existing studies demonstrated that directionality of response, as enabled by controlling the internal architecture of the elements, can play a part in spreading of the damage, and may improve the overall inelastic response of composite materials, specifically brittle ceramics and compliant organic materials <sup>[43-50]</sup>. In this work, the mechanical response of 3D-printed cement paste elements with specific architectures, along with the associated damage mechanisms, have been investigated by examining the behavior of both, the individual filaments (i.e., layers of deposited material) and the interfaces between the filaments.

Many of the internal architectures that can be fabricated via 3D-printing are either not possible, or are extremely challenging to achieve, while using conventional casting methods. To illustrate this point, this chapter presents several elements with various materials architecture achieved by 3D-printing of the ordinary portland cement paste using the direct-ink-writing (DIW) method. These architectures included: a compliant structure with honeycomb architecture (**Figure 5.1a**), a cellular sandwich panel prism with solid top and bottom layers (**Figure 5.1b**), a 'Bouligand' architecture with helicoidal alignment of filaments at pitch angles  $\gamma = 2^\circ$  and  $45^\circ$ , (**Figures 5.1c,d**).

The 3D rendition of the design of Bouligand architecture with  $\gamma = 45^\circ$  is shown in **Figure 5.1e**, whereas 3D rendition of the entire volume of Bouligand architecture with  $\gamma = 45^\circ$  generated using X-ray Micro-CT is shown in **Figure 5.1f**.

When subjected to cycling loading, a compliant structure with honeycomb architecture (similar to that illustrated in **Figure 5.1f**) displayed bi-linear stress-strain behavior characterized by two discrete values of moduli of elasticity (see **Figure 5.S1** in Supporting Information).

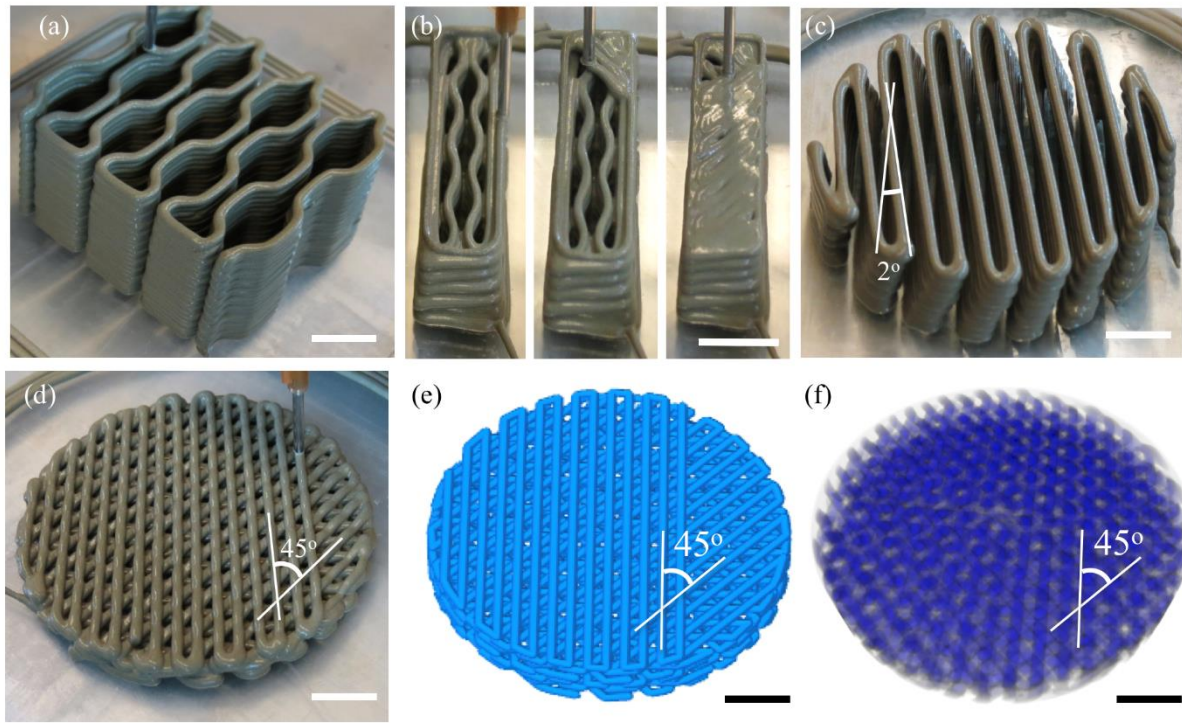


Figure 5.1. Various 3D printed architectures of hardened cement paste (hcp) elements; a) Compliant structure with honeycomb architecture; b) cellular sandwich panel prism with solid top and bottom layers; c-d) Bouligand architecture with, respectively, pitch angles  $\gamma = 2^\circ$  and  $45^\circ$ ; e) 3D rendition of the design of Bouligand architecture with  $\gamma = 45^\circ$  and; f) 3D rendition of the entire volume of Bouligand architecture with  $\gamma = 45^\circ$  from X-ray micro-CT. All scale bars are 10.0 mm long.

The values of modulus of rupture (MOR) of printed solid prisms with various filament orientations (i.e.,  $0^\circ$ ,  $45^\circ$ , and  $90^\circ$  with respect to X-axis, **Figure 5.2a**) were determined using the three-point-bending (3PB) test (**Figure 5.52b**). A comparison of average values of specific MOR for printed and cast specimens (**Figure 5.2c**) reveals that they were not statistically different (i.e.,

at the 95% confidence level  $p \geq 0.05$  for all printed specimens when compared to cast specimens). This implies that the mechanical response of all three of the printed prisms was independent of the orientation of the filament, and the specimen processing method (i.e., printed vs. cast). Since there are some observable variations in crack patterns of specimens with different filament orientations (**Figures 5.2d-m**), the lack of statistically discernible changes in the values of specific MOR (despite the presence of such differences in work of failure (WOF) values of printed and cast specimens shown in **Figure 5.3c**) may simply imply that the 3PB test is not capable of adequately capturing the microscopic level fracture response. However, the 3PB test can be used to characterize the strength of the materials (i.e., tensile strength of the individual filaments) and the interfacial strength. The strength of the materials reaches a plateau as the thickness of both cast, and the 3D-printed prisms with  $0^\circ$  filament orientations increases from 1 mm (i.e., 1 layer) to 12 mm (i.e., 12 layers) and as shown in Supporting Information (**Figure 5.S2**). The strength of the materials values are shown in **Figure 5.2c** are the average values from the plateau shown in **Figure 5.S2**. The interfacial strength was estimated via 3PB test of prisms with 12 mm thickness and  $90^\circ$  filament orientation and was found to be statistically similar to materials strength.

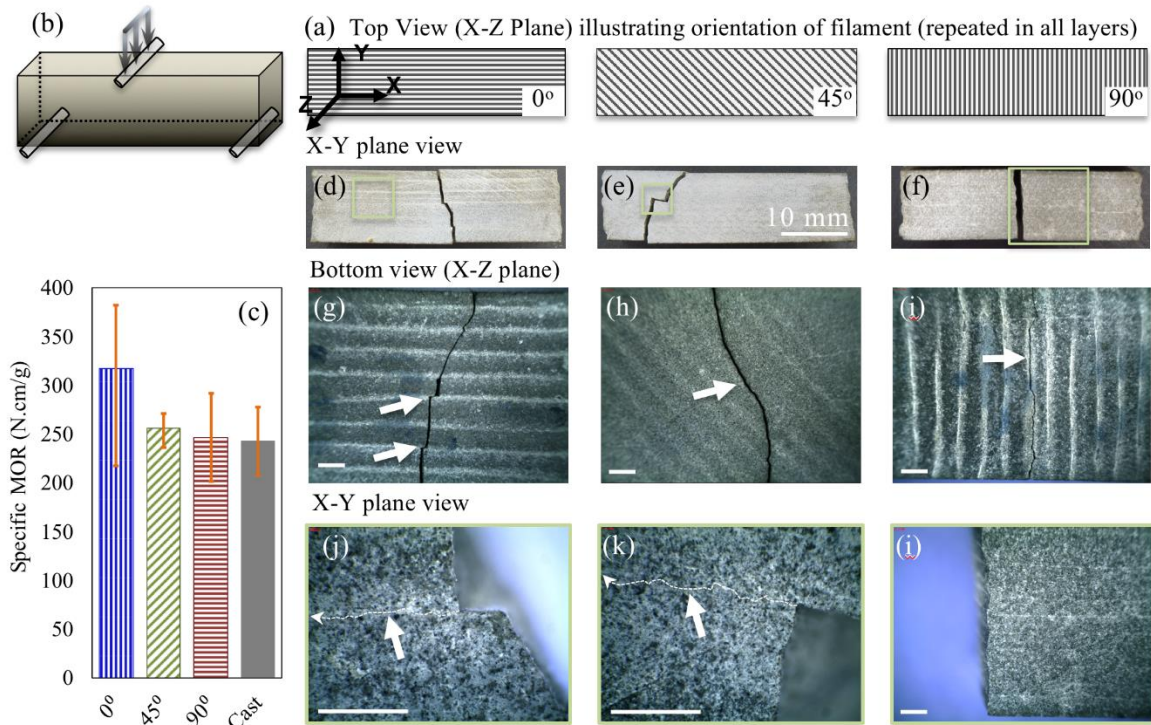


Figure 5.2. Mechanical response of 3D printed solid prisms with various architectures tested in 3PB; a) Schematic of the top face (X-Z plane) of the specimens showing orientation of the filaments; b) Schematic of the 3PB test; c) Specific modulus of rupture of 3D printed and cast elements; d-f) Post-failure images of specimens with 0°, 45° and 90° filament orientation illustrating crack paths (as viewed along Z axis); g-i) Crack paths on the bottom face of specimens (as viewed along the Y axis); j-k) micro-cracks along the interfaces in prisms with 0° and 45° filament orientations (viewed in X-Y plane, along Z axis) and; l) uncracked interfaces in prism 90° with filament orientation (viewed in the X-Y plane along the Z-axis. Unless indicated, all scale bars are 1.50 mm long.

Previous research indicated that 3D-printed cement-based elements exhibited zones of weakness at the interfaces between individual filaments [24-28], a phenomenon not commonly observed in conventionally cast hcp. The heterogeneous characteristics of the interfacial regions (IRs) in the 3D-printed solid prism (with 0° filament orientation) were characterized using X-ray micro-computed tomography (Micro-CT) and shown in Supporting Information (**Figure 5.S3a,b**). The heterogeneous IRs demonstrated a porous characteristic in the solid 3D-printed elements (see **Figure 5.S3** and video 19 in Supporting Information). The influence of these pronounced interfaces on the overall crack paths, and on the associated micro-cracking, has been observed to be unique for each of the 0° and 45° prisms used in this study. Specifically, the crack paths in

specimens with these two architectures intercepted the filaments (**Figures 5.2d,e**) whereas the crack path was parallel to the filament in the prisms with the third type of architecture (i.e., the one with 90° filament orientation). When the first two types of prisms (i.e., 0° and 45° filament orientations) were examined microscopically, the crack path was observed to be partially deflected to the heterogeneous interface along the layered filaments (i.e., it was parallel to the X direction). This partial deflection resulted in somewhat staggered crack pattern (**Figures 5.2d,e,g,h**). Furthermore, examination of **Figures 5.2j,k** revealed the development of microcracking along the interface between two filaments (i.e., in the X-Z plane) at the same locations where partial deflections of the crack path were observed. Micro-CT characterization of a prism with 0° filament orientation at two magnifications further elucidated the presence of micro-cracking at the interfacial regions near the fractured plane and is provided in Supporting Information (**Figure 5.S4**). In contrast, not such microcracking was observed along the X-Z plane interfaces of the prisms with 90° filament orientation (**Figure 5.2i**). This particular prism failed due to the formation of a single, predominantly unidirectional crack along the interfaces in the Y-Z plane (**Figure 5.2i**).

Overall, the microscopical comparison of crack paths in these three prism architectures indicates the presence of heterogeneous interfaces in the 3D-printed elements and the micro-CT examination of the prism with 0° filament orientation revealed the heterogeneous and porous characteristics of the interfacial regions (IRs) as provided in **Figure 5.S3a,b**. However, these observations also suggest that the crack paths in 3D-printed elements could be controlled by varying the orientation of the filaments. If such damage mechanisms are combined with architectures that promote local hardening by guiding cracks and promoting multiple site nucleation, then delocalization can be attained <sup>[54]</sup>. In other words, the implication of “engineering” the architecture of the 3D-printed elements enables mitigation of catastrophic failure that is not attainable in cast elements.

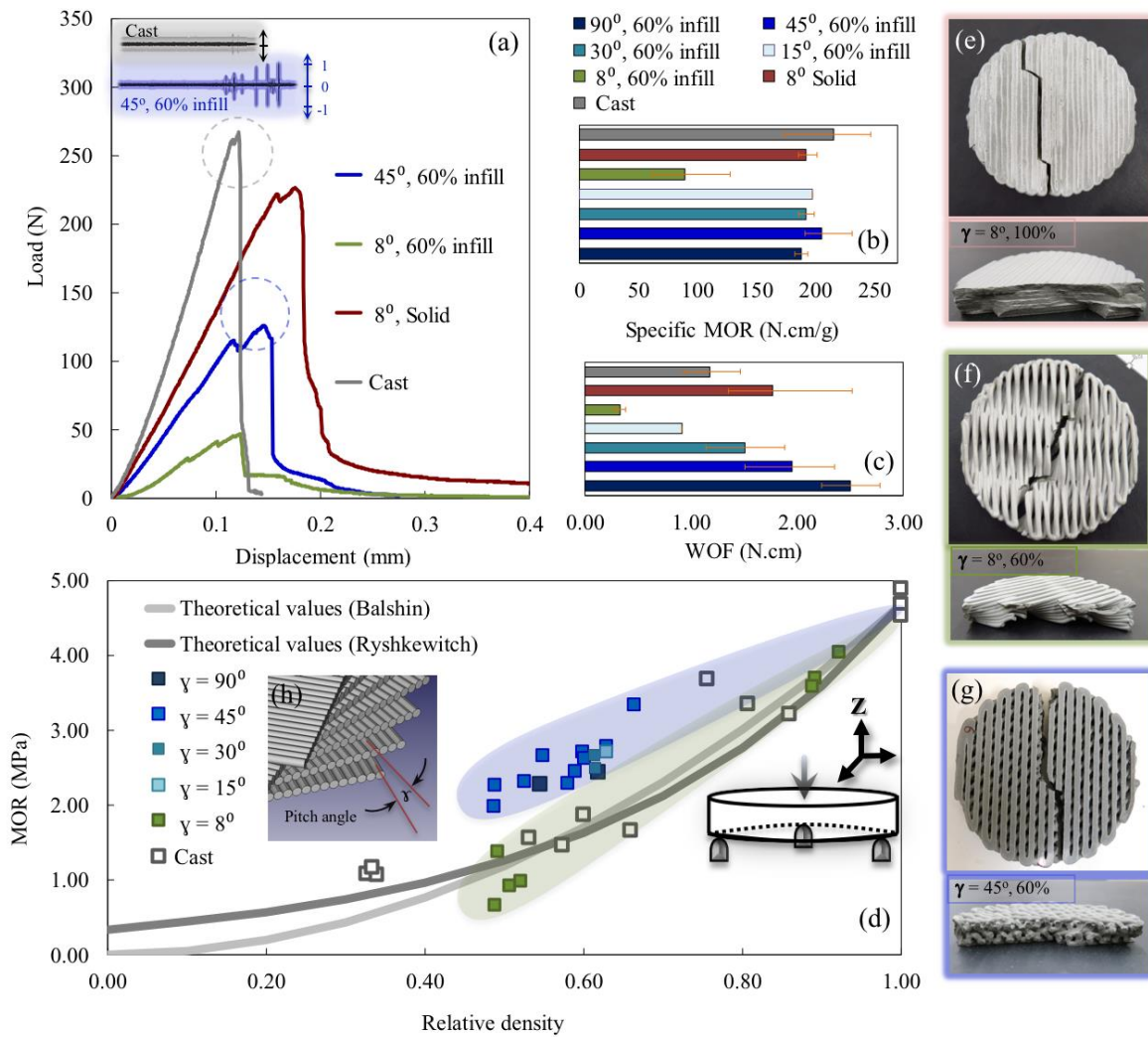


Figure 5.3. Mechanical response of Bouligand architecture using ball-on-three-balls test; a) Load-displacement for printed and cast disc specimens, including screenshot of acoustic spectrum recorded during testing; b) Specific modulus of rupture; c) work of failure, and d) Modulus of rupture (MOR) versus relative density for Bouligand architectures with varying pitch angles ( $8^\circ$ ,  $15^\circ$ ,  $30^\circ$ ,  $45^\circ$ ,  $90^\circ$ ) and percentages of infill (60% and 100%) compared to MOR of cast control discs; e-g) Views of bottom faces of discs with different Bouligand architecture; h) Schematic of Bouligand architecture with helicoidal alignment of filaments.

The Bouligand architectures utilized here have been previously reported to introduce damage mechanisms that increase the toughness and energy absorption capacity.<sup>[51-54]</sup> These architectures have found applications in engineering materials and offer enhanced fracture properties by enabling crack propagation in a stepwise pattern, crack redirection, branching, and prevention of catastrophic failure in various biological organisms such as lobster, crab, and mantis

shrimp <sup>[51-56]</sup>. Previous research has shown that these Bouligand architectures, found in the endocuticles of arthropods (such as mantis shrimp), tend to grow cracks in twisted patterns following the direction of the fiber.<sup>[51]</sup> These twisting patterns have been found to be responsible for increasing toughness <sup>[53]</sup> and promote the spread of the damage <sup>[54]</sup>.

In naturally occurring fibrous Bouligand architectures, a competition between interfacial failure (i.e., the separation between fibers) and solid failure (i.e., fiber fracture) of materials, is anticipated to be a trade-off between small and large pitch angles <sup>[51-56]</sup>. While small pitch angles facilitate the crack to grow through the interface, they also allow local softening <sup>[51-56]</sup>. However, this interfacial failure can be controlled by providing a crack path that leads to local hardening (e.g., such as crack twisting). This enables delocalization and spread of the damage to neighboring regions. In contrast, large pitch angles may lead to crack growth through the solid materials (e.g., biomineral in case of arthropods) and hinder the twisting or spread of the crack at the interface. These competing mechanisms can be controlled with the pitch angle as a design variable (among other material properties). This competition is demonstrated in this chapter by focusing on the analysis of the specimens with small pitch angle (e.g.,  $\gamma = 8^\circ$ ) and the large pitch angles (e.g.,  $\gamma = 45^\circ$  and  $90^\circ$ ).

To further investigate the structure-performance relationships, elements with several Bouligand architectures were 3D-printed by varying pitch angles ( $\gamma = 8^\circ, 15^\circ, 30^\circ, 45^\circ, 90^\circ$ ) and infill percentages (60% and 100%, i.e., cellular and solid). The Ball-on-three-Ball mechanical testing (B3B) was performed on these elements for determination of specific strength (MOR), work of failure (WOF), and documenting load-displacement behavior.

The results presented in **Figure 5.3a** illustrate that deflections at maximum load of elements with Bouligand architectures were consistently higher than the deflections at maximum load of the cast elements. Specifically, the observed increases in the maximum load deflections were 5%, 25% and 50% for architectures with  $\gamma = 8^\circ$  (60% infill),  $\gamma = 45^\circ$  (60% infill), and  $\gamma = 8^\circ$  (solid, i.e., 100% infill), respectively. It should also be noted that these Bouligand architectures have achieved higher deflection while having relative densities (i.e., the density of each specimen relative to the average of the conventional cast solid) lower than cast specimens.

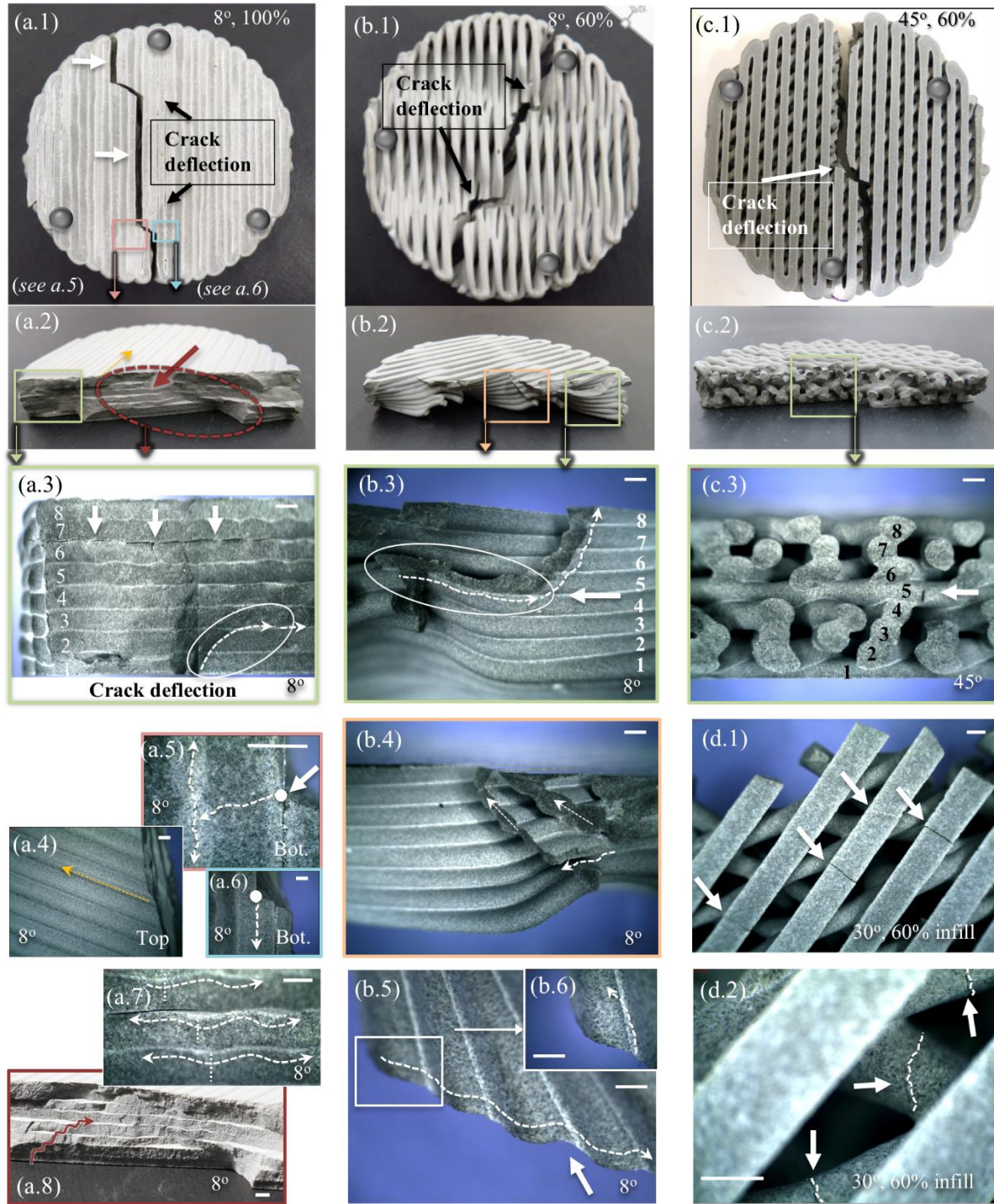


Figure 5.4. Crack paths and fracture patterns of various 3D printed Bouligand architectures; a1-a8)  $\gamma = 8^\circ$ , 100% infill; b1-b6)  $\gamma = 8^\circ$ , 60% infill; c1-c3)  $\gamma = 45^\circ$ , 60% infill and; d1-d2)  $\gamma = 30^\circ$ , 60% infill after B3B test. All scale bars are 1.0 mm long.

Similar to the observations from the prisms study presented above, the presence of the heterogeneous interface and the deflection of the crack path into the interface and presence of micro-cracks in the interfaces are also of particular importance for the printed disc structures. The heterogeneous characteristics of the IRs in the 3D-printed solid Bouligand architecture discs (with  $\gamma = 8^\circ$ ) were characterized using X-ray micro-CT and are provided in Supporting Information (**Figure 5.S3c,d** and Video 5.S10). These heterogeneous IRs displayed porous characteristics similar to those found in solid prisms with  $0^\circ$  filament orientation. The identified porous IRs found in the microstructure of 3D-printed materials (in both solid prism and solid Bouligand architecture, **Figure 5.S3**), can enable the spread of the damage in the solid structure by localization of micro-cracks. In cellular structures, fracture of sacrificial links between filaments without sacrificing the integrity of the structure can provide the spread of the damage in the structure and tolerance to fracture. The damage and fracture process of filaments in pre- and post-peak regions are additionally captured with acoustic recording in the studied Bouligand architectures. The screenshot of the acoustic recording of the fracture process during testing of  $\gamma = 45^\circ$  disc and the cast disc is also illustrated in **Figure 5.3a**. The screenshot of the acoustic recordings qualitatively describes the propagation of multiple cracks in the pre- and post-peak regions of the Bouligand structure. The major peaks of the acoustic graph match the local maximum loads. This detected damage propagation is distinguishably different from the brittle fracture of cast discs shown in **Figure 5.3a**.

In terms of strength, the majority of Bouligand structures ( $\gamma = 15^\circ, 30^\circ, 45^\circ, 90^\circ$ ), except  $\gamma = 8^\circ$  with 60% infill, are statistically similar in average specific values of MOR when compared to cast structures (**Figure 5.3b**). This equivalent performance includes the solid specimen with the small pitch angle of  $\gamma = 8^\circ$  and 100% infill.

The WOF was assessed for all Bouligand architectures, and an increase in WOF was observed as  $\gamma$  increased from  $8^\circ$  to  $90^\circ$  for 60% infill structures (**Figure 5.3c**). The observed pattern is consistent with previous studies on composite materials with the Bouligand architecture, suggesting increased WOF with the increase in rotation angle <sup>[52-54]</sup>. **Figure 5.3c** describes how  $\gamma$  or infill percentage can play a role in the fracture properties of materials. The solid structures with  $\gamma = 8^\circ$  demonstrated elevated WOF compared to its identical  $\gamma$  at lower density (60% infill). The solid structures with  $\gamma = 8^\circ$  show a counter-clockwise orientation of the fractured plane following the right-hand pattern in consecutive layers (positive counter-clockwise  $\gamma$ ) indicating subtle

twisting of the fracture plane across the height of the specimen. The fracture properties of Bouligand architectures studied here indicates the ability to control the WOF by controlling the pitch angle and relative density in brittle materials. The detailed comparison of specific MOR and WOF between Bouligand architectures and monolithic cast hcp counterparts is provided in Supporting Information (**Figure 5.S5**). It was demonstrated that most of Bouligand architectures attained specific MOR similar to that of the cast elements, while statistically significant enhancement in WOF of both solid ( $\gamma = 8^\circ$ ) and cellular ( $\gamma = 90^\circ, 45^\circ$ ) architectures was observed when compared to values recorded for cast elements (**Figure S5b**).

The performance of Bouligand structures (in terms of MOR with respect to their relative density) was assessed for various  $\gamma$  values and compared to the performance of the cast cellular counterparts (see Experimental Section for sample preparation description) over a broad range of porosities (**Figure 5.3d**). Apparent from **Figure 5.3d**, and benchmarked against theoretical curve and values of MOR for hardened cast cellular hcp <sup>[57]</sup>, is the emergence of a distinct group of printed Bouligand architectures with  $\gamma = 15^\circ$  to  $90^\circ$  (outlined in blue in **Figure 5.3d**) that consistently out-performs conventionally cast specimens across the relative density range considered (0.5-0.65). When the average values of MOR for the Bouligand architectures with  $\gamma = 15^\circ, 30^\circ, 45^\circ, 90^\circ$  (as outlined in blue in **Figure 5.3d**) were compared with the cellular cast specimens (i.e., specimens with similar relative density range, between 0.50 to 0.65 as shown in **Figure 5.3d**), a statistically significant enhancement in favor of Bouligand architecture specimens was found. When a similar comparison was performed between Bouligand architecture specimens with  $\gamma = 8^\circ$  and cellular cast specimens, no statistically significant difference in values of Specific MOR were found. The comparisons of MOR in **Figure 5.3d** demonstrates that Bouligand architectures can have at least similar (in case of  $\gamma = 8^\circ$ ) or significantly improved (in cases of  $\gamma = 15^\circ, 30^\circ, 45^\circ, 90^\circ$ ) MOR compared to their cellular cast hcp counterparts within the same range of densities. This gives a clear indication that significantly improved performance is attainable in most 3D-printed Bouligand architectures relative to the conventionally cast specimen with equivalent density, reflecting the unique ability of element's architecture to enhance mechanical properties. (**Figures 5.3d**). It must be noted that naturally-occurring architected materials typically exhibit improved toughening, in many cases an order of magnitude higher, compared to monolithic counterparts <sup>[44,58-60]</sup>. Natural materials achieve this improvement, without significantly sacrificing other mechanical properties such as strength and stiffness <sup>[44,58-60]</sup>. The mechanisms that

lead to this improvement have been attributed to the composite effect of minerals with soft materials combined with the hierarchical architecture that results in triggering controlled failure through the interface and delocalization of cracks [44,58]. In turn, this delocalization leads to improved energy dissipation over large volumes that contributes to the toughness of the materials [44]. In our work, the improvements in mechanical properties demonstrate that some of these mechanisms can be reproduced by controlling the architecture and incorporating the heterogeneous interface in the 3D-printed hcp materials. However, the size of specimens used here, when compared to the features of their architecture (e.g., the height and the width of the filament) may be too small to capture the same level of increase as that observed in small increase in toughness with respect to the monolithic (i.e., cast) hcp specimens. The mechanical response of the Bouligand architecture specimens studied here suggest that an increase in toughness is attainable and that the architecture can assist in achieving similar failure mechanisms that were previously reported for this architecture [51-54,56]. However, increase in toughness will occur mostly in the form of spread of the damage and delocalization of cracks are expected to take place in specimens of larger volumes.

Bouligand architectures were further studied for identification of the fracture patterns, crack paths, and micro-cracks using optical microscopy (**Figure 5.4**). A variety of fracture paths and crack patterns were observed at the bottoms (**Figures 5.4a.1-c.1**) and at the cross-sections of Bouligand architectures (**Figures 5.4a.2-c.2**). In specimens with large pitch angles, such as  $\gamma = 45^\circ$  (and 60% infill, the crack path appears to shear the filaments (**Figure 5.4c2,c3**), whereas it advances at the interfaces between adjacent filaments in specimens with small pitch angle  $\gamma = 8^\circ$  (in both cases 60% and 100% infill, **Figures 5.4a.2,b.3**). The crack path for the  $\gamma = 45^\circ$ , resulted in shear failure in the filaments typical in Bouligand structures with large pitch angles (**Figure 5.4c2,c3**). However, the filaments in the layers parallel to the main failure plane remained intact (in layer 1 and layer 5, **Figures 5.4c.3**). In contrast to the specimen with large pitch angle architecture ( $\gamma = 45^\circ$ , **Figures 5.4c.3**), the horizontal propagation of the crack paths at the interfaces (between layer 4 and 5) is observed for specimens with small pitch angle ( $\gamma = 8^\circ$ ) and 60% infill as demonstrated in **Figures 5.4b.3,b.4**. In the solid structures with small pitch angle ( $\gamma = 8^\circ$ ), the micro-cracks propagate at the interface (between layers 6 and 7) and between layers 2 and 3 near the crack divergence points at the cross-section shown in **Figure 5.4a.3**. Advancement of the micro-crack at the interface in the solid specimens with  $\gamma = 8^\circ$  is further accompanied by

development of multiple parallel micro-cracks throughout the top (**Figures 5.4a.4**) and bottom layers (**Figures 5.4a.5,a.6**). Also, a staggered fractured pattern is observed in the main failure plane (**Figure 5.4a.2,a.8**). Micro-CT characterization of a solid Bouligand architecture with  $\gamma = 8^\circ$ , further elucidated crack advancement and micro-cracking at the interface as illustrated in **Figure 5.S6** and **Videos 5.S12 to 5.S14** in Supporting Information). The two interfacial damage mechanisms (i.e., horizontal propagation of the crack and micro-crack propagation at the interface) for specimens with small pitch angles are of great interest as they can promote controlled crack growth and local hardening. In contrast, Micro-CT characterization of a cellular Bouligand architecture with large pitch angle ( $\gamma = 45^\circ$ ) demonstrated the shear failure of the filaments (**Figure 5.S7a,b**, and **Videos 5.S15-S18**). The contrast between damage mechanism in this large pitch angle is further elucidated in **Figure 5.S7c,d** comparing it with the solid Bouligand architecture with small pitch angle  $\gamma = 8^\circ$ . The shear failure of the filaments at large pitch angles are in accordance with previous research findings on damage mechanisms in composite Bouligand architectures that present solid failures at such large pitch angles <sup>[51-54]</sup>. The WOF for solid structures with  $\gamma = 8^\circ$  was higher than that the conventionally cast discs (**Figure 5.3c**); may be attributed to toughening and damage mechanisms such as observed micro-cracking advancement at the heterogeneous interfaces.

Micro-cracking of other type was observed in the bridging links between the filaments in Bouligand architectures in  $\gamma = 30^\circ$  structures. In this case, multiple parallel micro-cracks were observed near the fractured plane of the specimens at the bottom of layers 1, 2 and 3 (**Figures 5.4d.1,d.2**). These parallel micro-cracks are spaced equally from the fracture edge in the very bottom layer (**Figure 5.4d.1**) and appear twisting in the subsequent bottom layers 2 and 3 at the bridging links (**Figure 5.4d.2**).

A similar sinusoidal fractured pattern is observed in the Bouligand architecture with small pitch angle  $\gamma = 8^\circ$  with both 60% infill and 100% infill (**Figures 5.4a.7,b.6**). It is noteworthy that in the 60% infill case, the micro-crack advancement is also observed at the interface (**Figure 5.4b.6**).

Overall, in Bouligand architectures, the crack deflection at the interface are commonly observed for smaller pitch angles ( $\gamma = 8^\circ$  with 60% infill and 100% solid, **Figures 5.4b.3,b.4,a.1**). The micro-crack advancement at the interface is also observed in small pitch angle (**Figures 5.5a.3-a.6,b.5**) indicating heterogeneous properties of the interface. The presence of this

heterogeneous interface, not only allows for crack path to follow the interface but also for initiation of numerous micro-cracks. Acknowledging this possibility, control of the architecture (via control of the pitch angle) and the properties of the interface can be combined to promote crack initiation and interfacial damage mechanisms and to allow for controlled crack growth and for an increased threshold to crack initiation, initiation toughness, inelastic deformation, and WOF (**Figure 5.3c**).

As reported earlier, Bouligand architectures are known to present competing interfacial and solid damage mechanisms corresponding to small and large pitch angles, respectively [53,54]. The small pitch angles allow for crack growth at the interface and for control of the crack path, whereas large pitch angles facilitate crack advancement through the solid material. The damage mechanisms for specimens with small pitch angle ( $\gamma = 8^\circ$ ) solid (100% infill) and cellular (60% infill) Bouligand architectures used in this study, demonstrate that the interfaces promote damage mechanism such as crack advancement at the interface and micro-cracking as shown in **Figure 5.a2-a8** and **Figure 5.b3-6**, respectively, as well as **Figure 5.S7c,d**. In contrast, the damage mechanisms for specimens with large pitch angles ( $\gamma = 90^\circ$  and  $45^\circ$ ), involves a dominant crack growth through the solid filaments as demonstrated in **Figure 5.c2,3** and **Figure 5.S7a,b**. The mechanisms demonstrated in solid and cellular Bouligand architectures with a small pitch angle of  $8^\circ$ , can allow for achieving flaw-tolerant behavior in a larger volume. We therefore, surmise that an optimum architecture could be obtained with a Bouligand structure with moderate pitch angles. Such angles will be large enough to promote local hardening in the material, and therefore, allow multiple site crack nucleation, and small enough to avoid advancement of one dominant crack through the filaments

The fracture behavior of hcp commonly exhibits brittle and unstable crack propagation [24]. Overall, in 3D-printed prisms with  $0^\circ$  and  $45^\circ$  filament orientations, horizontal deflection of crack is observed at the interface, followed by advancement of micro-cracks at the interface between filaments (**Figures 5.2g,h**, **Figure 5.S4**). This crack deflection and the subsequent micro-crack induction, suggests the possibility of the increased spread of the damage in the design of these architected materials. In  $90^\circ$  prisms, no micro-crack or crack deflection at the interface is observed. However, a remarkable observation, in this case, is that the main crack occurs at the interface between the filaments in the mid-span of the specimens through the entire cross-section (**Figures 5.2i**). Thus, the interface between layers can be utilized in an architecture in which the micro-cracks can be advanced in multi-layers and create a fracture toughening mechanism [44,45].

More broadly, in both types of solid prisms and Bouligand architectures studied in this work, micro-crack advancement along the interface is observed. In most cases, the initiated micro-cracks in solid prisms (**Figure 5.2j,k**, **Figure 5.S4**) and solid Bouligand structures (**Figures 5.4a.3-a.6**, **Figure 5.S6**) spread to the edges of the specimen. Moreover, these interfacial micro-cracks are straight on a macroscopic scale, and follow the architectural pattern of the interfaces, both in prisms (**Figures 5.2j,k**, **Figure 5.S4b,c**) and Bouligand architectures (**Figure 5.S6c,d**). In contrast, in 3D-printed hcp we demonstrate that the properties of the interface between the filaments can be designed to act as a crack trap leading to multiple crack initiation sites across filaments, and eventually define the overall response of the 3D-printed architected hcp materials under loading.

The periodic crack patterns found in bridging elements near the failure plane in the 30° Bouligand architecture signifies that architecture of the material can allow for induction of cracks through sacrificial links without compromising the integrity of the structure. The failure of the sacrificial links does not necessarily decrease the strength (**Figure 5.3b**). However, it can contribute to the spread of damage due to the improved initiation toughness<sup>[45]</sup>. Such architectures, despite the brittle nature of their base materials, can experience localized damage triggered by failure of sacrificial links (**Figures 5.4d.1,d.2**) and yet be able to tolerate micro-cracks in each link. These micro-cracks can contribute to an increase in the overall inelastic deformation and toughening of the material without resulting in an abrupt macroscopic failure of the structure. Further understanding of such critical architectural parameters and interfacial properties can help in the design of flaw-tolerant brittle architected materials.

In summary, the results presented in this paper demonstrate damage mechanisms that can allow brittle hcp materials to obtain flaw-tolerant properties. These damage mechanisms include crack growth at the interfaces, and interfacial microcracking. Other mechanisms, such as crack twisting, previously reported in naturally-occurring materials and synthetic Bouligand architecture,<sup>[44,45]</sup> are a product of the interplay between interface properties and architecture. It was found that the presence of heterogeneous interface in 3D-printed hcp elements, facilitates damage mechanisms such as interfacial cracking and micro-cracking and the delocalization of the damage. This delocalization can be energetically favorable, and allow for energy dissipation and promote toughening and flaw-tolerance properties. These mechanisms can be controlled via AM and design of the architecture of hcp materials and can play a role in tuning of the damage mechanisms and in enhancing work of failure, strength and overall inelastic response of brittle materials. It was

found that Bouligand architectures demonstrated elevated improvement from the typical strength-porosity relationship, classically known for brittle hcp materials. In turns, the Bouligand architectures showed improvements of the work of failure by more than 50% exhibiting the controlled spread of damage without sacrificing the strength.

Two competing damage mechanisms were observed in Bouligand architectures used in this study. Specifically, it was found that in hcp elements with Bouligand architecture, the use of small pitch angles ( $8^\circ$ ) will facilitate interfacial crack growth through the interface and promote interfacial micro-cracking, where the use of larger pitch angles ( $90^\circ$  and  $45^\circ$ ) will result in a dominant crack growth through the solid filaments (**Figure 5.S7**).

The heterogeneous characteristics of the interfacial regions in the solid 3D-printed prism and Bouligand architecture specimens was characterized using micro-CT (results are provide in **Figure 5.S3** in Supporting Information). It was demonstrated that the presence of a porous IRs could promote damage mechanisms such as crack advancement and micro-cracking in these regions. These mechanisms can allow for crack initiation and for controlled crack growth, followed by local hardening mechanism (e.g., crack twisting).

We have demonstrated that AM and control of the architecture of the elements, can lead to novel behaviors of cement-based materials. These behaviors, observed in compliant design (**Figure 5.S1**), prisms and Bouligand architectures, demonstrate new potential for engineering performance of cement-based materials. Architectures such as compliant design demonstrated bilinear stress-strain behavior, not attainable in cast elements, and thus can provides the ability to customize stress-strain behavior as applicable.

Processing-induced weak interfaces are commonly considered to constitute defects in AM of cementitious materials and are therefore avoided. In Bouligand architectures, we demonstrated that such heterogeneous interfaces exist and are not necessarily detrimental to the overall performance, rather they can provide mechanisms that can lead to novel responses such as an increased deflection, enhanced WOF, and a variety of damage mechanisms. It must be noted that the development of these enhanced properties certainly depends on the ability of the material to spread the damage over larger volumes. Indeed, the mechanisms analyzed in this work can be applied to other specimen sizes and can be used in the architectural design of brittle materials.

To further explore opportunities provided by architected cement paste materials, a fundamental understanding of the intertwined relationships between processing-induced

heterogeneities, interfacial strength, ink properties (cement hydration, rheology, chemistry, and formulation), architectural parameters (such as pitch angle and infill percentage), and microstructural characteristics of the filaments and interfaces must be developed to fine tune the performance of resulting elements. Further understanding of the architectural parameters and interfacial properties, can result in the design of flaw-tolerant architected materials with a brittle base, such as hardened cement paste.

It must be noted that in brittle cast hcp elements, only a small portion of work-of-failure calculated from the area under the curve represents the actual energy dissipated by the fracture process, mainly due to the dynamic nature of fracture (i.e., snap-through behavior) in those elements. The rest of the area is the elastic energy that is stored in the element which is suddenly released as wave propagation, sound, heat, etc. In contrast, in architected elements, the observed softening indicates little dynamic phenomena, and therefore, it is more plausible that the majority of the area under the curve represents the work-of-failure after the crack is initiated. In other words, a large portion of reported work-of-failure in architected elements can be conceived as inelastic as there are little dynamic effects during the fracture process. If only the portion of the amount of energy after the crack is initiated were to be considered, the cast elements would even have a smaller work-of-failure compared to architected hcp elements. Therefore, if only the energy dissipated by the actual fracture process is considered, architected elements would represent an even greater improvement in toughness. In the future, measurement of fracture toughness can assist with a better estimate of the portion of reported work-of-failure, that dissipates the energy in the actual fracture process.

## 5.2 Experimental Section

**Cementitious Ink Formulation:** An iterative trial and error ink design procedure is used to identify cement inks suitable for the DIW process. The ink with proper flow properties that can overcome processing challenges, such as flocculation, bleeding, and which could ensure in suitable shape holding properties was designed. The final ink used constituted the sub 150  $\mu\text{m}$  fraction of commercially available Type I cement (Buzzi Unicem USA) in accordance with ASTM C150<sup>[61]</sup>, deionized water, and both high range water reducing admixture (HRWRA-MasterGlenium 7700) and viscosity modifying admixtures (VMA-MasterMatrix 362) in accordance with ASTM C494

<sup>[62]</sup> and the findings of previous study <sup>[63]</sup>. For each 250 g of cement, the mix comprised 65.2, 1.1 and 3 g of deionized water, HRWRA, and VMA, respectively.

**Mixing Procedure:** A Twister Evolution Venturi vacuum mixer is used to mix the ingredients and to eliminate the entrapped air. First, admixtures are added and dispersed in water and pre-mixed with cement for 25 s, followed by mixing at 400 rpm for 90 seconds at 70% vacuum. This was followed by mixing (for another 90s) and then finally at 400 rpm at 100% vacuum. This procedure was applied in preparing the cement paste ink for 3D-printed and cast specimen.

**Ink Rheology:** Rheological properties of the ink are characterized using a Malvern Bohlin Gemini HR rheometer with 40 mm parallel plates (with the serrated surface to minimize the slippage during the tests). A solvent trap was used to avoid evaporation during the test. The rheological protocol used, and the yield stress and viscosity versus shear rates are presented in the Supporting Information (**Figure 5.S8**). The shear rate at the nozzle is calculated in Supporting Information, and the corresponding viscosity of the ink is estimated and provided at this rate (**Figure S8b**).

Rheological properties of the ink were characterized using a Malvern Bohlin Gemini HR rheometer equipped with 40 mm parallel plates (with the serrated surface to minimize the slippage during the tests). A solvent trap was used to avoid water evaporation during the test. The rheological protocol used, and the values of the yield stress and viscosity versus shear rates are presented in **Figure 5.S8** (Supporting Information). The shear rate at the nozzle was calculated using previously developed equations <sup>[64,65]</sup> (see details in the Supporting Information) and the corresponding viscosity of the ink was estimated and provided at this rate (**Figure 5.S8b**, Supporting Information).

**3D-Printing:** A bespoke system is developed by merging a 3D printer typically used for printing thermoplastics (Ultimaker 2 Extended+) with a stepper motor-driven extrusion system (Structur3d Discov3ry Paste Extruder) capable of applying desirable extrusion rates to mounted 75 mL ink-charged syringes. The 3D printer hardware is modified by mounting a lightweight aluminum nozzle holder on the gantry for nozzle placement. The printer and extrusion system are connected through standard luer locks and polyethylene tubing. Slicer-generated g-code command included X,Y, Z point cloud coordinates, E (extrusion), and F (printing speed) commands specific to each design. A nozzle with an internal diameter of 1.36 mm, a layer thickness of 1 mm, and a printing speed of 250 mm min<sup>-1</sup> is used throughout. The resulting filaments have a nominal width

of 1.63 mm and a height of 1 mm. The nominal width is calculated by multiplying internal nozzle diameter by a factor of 1.20 to account for die-swell effect. Specimens are transferred to a curing chamber with a relative humidity of  $93 \pm 1$  % (using potassium nitrate) at 25 °C immediately after printing or casting. The specimens were cast and printed in the lab environment at  $18 \pm 3$  °C and  $45 \pm 5$  % relative humidity. During casting, the paste was carefully poured into the mold to ensure no additional entrapped air is introduced during casting.

**Characterization:** The modulus of rupture and flexural strength and modulus-of-rupture (MOR), is used to characterize the mechanical properties of the specimens. These properties were determined using uniaxial three-point bending (3PB) testing of prism specimens and multi-axial ball-on-three-ball (B3B) testing of disc-shaped specimens. For 3PB testing, prisms are designed to have final dimensions of 12 x 12 x 40 mm, with surfaces being ground flat prior to testing to ensure acceptable tolerances and good contact with test support plates <sup>[66]</sup>. MOR is calculated based on the measured dimensions of each specimen. B3B testing was selected for determination of the flexural strength of disc specimens due to its high sensitivity to internal defects and insensitivity to outer and surface imperfections <sup>[67,68]</sup>. A load is applied via a central ball on the top face of a round, disc-shaped specimen of 55 mm diameter and 8 mm thickness supported underneath by three equally sized, equidistantly spaced balls placed on a 50 mm diameter circle <sup>[69]</sup>. Bouligand structure discs are aligned to ensure that bottom filament orientation is aligned with the maximum stress field. A stereo microphone device (Zoom iQ6) with customizable stereo width is used to capture crack noise.

Force and displacement for both tests are measured using a 10 kN capacity test rig (MTS insight 10). All reported data is an average of at least two separate results. The relative densities of specimens were calculated from measured mass and volume of each specimen divided by the average mass of conventionally cast ‘solid’ specimens. Specific MOR is calculated by dividing the MOR value for each specimen by its relative density. WOF is calculated by integrating the entire areas under load-displacement curves. The specific WOF was calculated by dividing the WOF value for each specimen by its relative density. Although the first crack occurs at the first drop in the load-displacement curve, the WOF based on the entire area under the load-displacement curve. Two theoretical relationships between porosity and strength for brittle materials are presented in **Figure 5.3d** and describe the strength-porosity relationship of lightweight cellular structures based on the strength of a control specimen with zero porosity <sup>[57,70,71]</sup>. All specimens

are tested at the age of 3 days ( $72 \pm 2$  hours). Aluminum powder and variations of water/cement ratios are used to cast lightweight cellular specimens.

**X-ray micro-CT characterization:** An X-ray microscope (XRM), Zeiss Xradia 510 Versa which allows for an increase in the resolution of scans through dual-stage magnification process was utilized. In the first stage (i.e., 0.4X scan), the field of view (FOV), desirable to scan the entire volume of the specimens was established via geometric magnification process, which involved setting distances between the source, detector, and specimen (as in conventional micro-CTs)<sup>[72,73]</sup>. In a second stage (4X scan), additional optical magnification was enabled at the detector system through objective lenses. The detector is equipped with scintillator and objective lens which converts X-rays to light rays and thus allows for optical magnification and higher resolution. The 0.4X scans were performed for a solid Bouligand architecture with  $\gamma = 8^\circ$ , a solid prism specimen with  $0^\circ$  filament orientation, and a cellular Bouligand architecture specimen with  $\gamma = 8^\circ$ . Using this magnification allowed a large FOV and thus facilitated to scan the entire specimens (55.1  $\mu\text{m}$ , 37.2  $\mu\text{m}$ , and 46.8  $\mu\text{m}$  pixel size, respectively). For the solid prism, this was followed by a 4X scan, allowing higher resolution (4.42  $\mu\text{m}$  pixel size) at the region of interest near the main crack (ROI). The beam energies of 150 KeV, 140 KeV, 90 KeV, 100 KeV, the power levels of 10 W, 10 W, 8 W, and 9 W, and exposure times of 4 s, 2 s, 4 s, and 14 s were used for 0.4X scans of the solid Bouligand architecture with  $\gamma = 8^\circ$  and  $45^\circ$ , and the 0.4X and 4X scans of the solid prism specimens with  $0^\circ$  filament, respectively. Dragonfly software was used for post-processing of the data.

### 5.3 Appendix

Supporting Information is available from the Wiley Online Library or from the author.

### 5.4 Acknowledgments

The authors gratefully acknowledge generous support from the National Science Foundation (CMMI 1562927) of this research. The authors would also like to thank the BASF chemicals company for providing materials.

## 5.5 Supporting Information: Additive Manufacturing and Performance of Architected Cement-based Materials

### Compliant Architecture (Figure 5.S1)

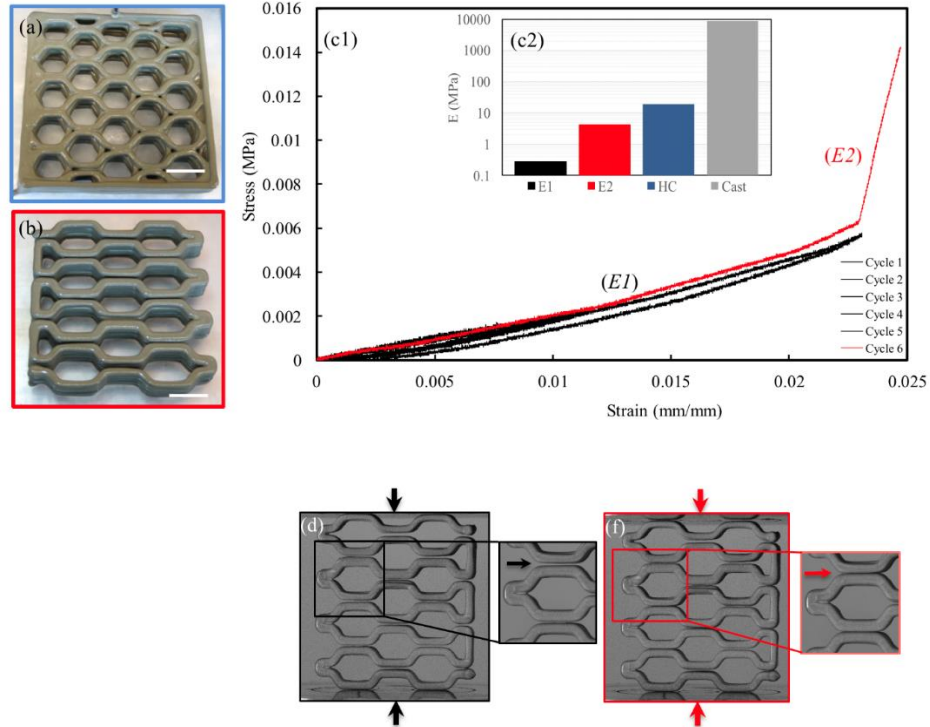


Figure 5.S1. a) Closed cell honeycomb structure, b) Compliant structure with honeycomb architecture, c1) Bilinear stress-strain behavior of compliant structure (b), including five primary linear strain recovery (Cycles 1-5) and secondary response (Cycle 6) before and after filament's contact, c2) Comparison of moduli of elasticity ( $E1, E2$ ) of compliant structure (b2) with closed cell honeycomb (a) and cast, d) Compliant structure in cyclic loading (cycles 1-5) in which filaments do not make contact and, f) Compliant structure (in cycle 6) where filaments make contact. All scale bars are 10 mm long.

A honeycomb architecture with close cell (**Figure 5.S1a**) and open cell (compliant) design (**Figure 5.S1b**) is demonstrated. The compliant structure can demonstrate bilinear stress-strain behavior, including a primary linear strain recovery ( $E1$ ) at strains below which the layered filaments make contact (cycles 1-5 in **Figure 5.S1c1**) and a secondary linear response above strains ( $E2$ ) at which the filament's contact take place (cycles 6 in **Figure 5.S1c1**). As can be seen, the jointless compliant structure shown exhibits two discrete moduli ( $E1, E2$ ) depending on whether the filaments have made contact (**Figure 5.S1d,e**) or not (**Figure 5.S1f,g**). In contrast, the closed

cell honeycomb architecture (HC) and cast element exhibit only one value of modulus (**Figure 5.S1c2**).

This dual response of the honeycomb structure can be likely customized to other types of structures by suitable design of the architecture, selection of spacing between filaments, and changes in material properties. The strain at failure of the cast hardened cement paste element is of about 0.008. This is in the general range reported for typical hardened cement paste [39]. In contrast, the strain at failure observed in the compliant structure was much higher (as high as 0.025 in the bi-linear region).

### ***Characterization of Material Strength (i.e., filament strength) and Interfacial Strength (Figure 5.S2)***

The strength of a single filament and the interfacial strength was estimated using 3-Point-Bending (3PB) test on prism printed and cast specimen. To obtain material tensile strength, an experiment with specimens of varying thickness was designed. Cast specimen with 10 mm width and 1, 2, 5, and 12 mm thickness were made and tested in 3PB, and the specific MOR was obtained (as outlined in grey in **Figure 5.S2**). Similarly, printed specimen with 10 mm width and 1, 2, 5, and 12 mm thickness (corresponding to 1, 2, 5, and 12 layers) and 0° filament orientation were fabricated and tested in 3PB, and the specific MOR was obtained (as outlined in blue in **Figure 5.S2**). As the thickness of specimens increases, this specific MOR as reported in **Figure 5.S2a** reaches a plateau for the specimens with a thickness greater than 5 mm. As the bottom layers remain in tension, the average tensile strength of a single filament is assumed to be the average strength of the prisms at the plateau.

To obtain interfacial strength, prisms with 10 mm width, 12 mm thickness and 90° filament orientation was fabricated. The specimens were tested in 3PB, and specific MOR was obtained. An evident cleavage, parallel to the filaments (as shown in **Figure 5.S2e** in XY plane), was observed in the fractured prisms with 90° filament orientation. The interfacial strength is assumed to be the average strength of the element with 90° filament orientation.

The average value for interfacial strength as estimated from the 12 mm thick prism with 90° filament orientation is found to be  $246.4 \pm 49.1$ . The average filament strength as estimated from the 12 mm thick prism with 0° filament orientation and the cast is found to be  $317.2 \pm 95.5$  and  $243.1 \pm 73.6$ , respectively (as outlined in green rectangle in **Figure 5.S2a**. It must be noted that the

specimens with 12 mm layer height and  $0^\circ$  and  $90^\circ$  filament orientations in **Figure 5.S2** are also presented in **Figure 5.2a**, and is deployed here to provide the interfacial strength and filament strength.

Although the estimated average value of interfacial strength is lower than the tensile strength of the materials, when the estimated strength of the filament and the interface are compared, no statistically significant difference was found.

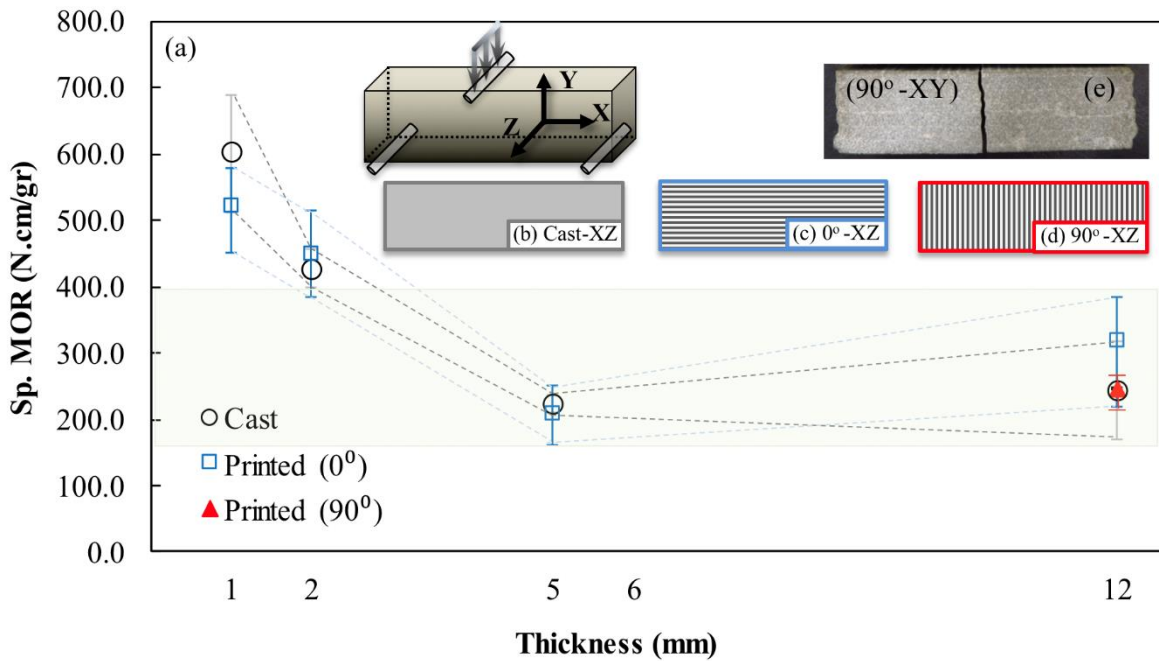


Figure 5.S2. a) Specific MOR vs. prism thickness for cast specimen (schematically shown in grey (b)), printed prism with  $0^\circ$  filament orientation specimens (schematically shown in blue (c)); and the Specific MOR of the prism with  $90^\circ$  filament orientation specimens (schematically shown in red (d)). Dash lines present limits corresponding to the minimum and maximum values of error bars in cast (grey) and printed prisms with  $0^\circ$  (in blue).

**Micro-CT Characterization of the interface in Solid Bouligand Architectures (with  $\gamma = 8^\circ$  and 100% infill) and in Solid Prism (with  $0^\circ$  filament orientation, Figure 5.S3)**

To investigate the characteristics of the interface, the microstructure of solid hardened cement paste Bouligand architecture disc with  $\gamma = 8^\circ$  (**Figure 5.S3a,b**) and solid prism specimen with  $0^\circ$  filament orientation (**Figure 5.S3c,d**) was characterized using micro-CT. In micro-CT

images of hcp, darker intensities represent pores filled with air or water, with greyscale intensities corresponding to hydrated cement paste products <sup>[72]</sup>.

The horizontal slices (C1,T1) shown in cross-sectional (H9) view in **Figure 5.S3c**, corresponds to the ‘core’ (i.e., through the interface) and ‘interfacial regions’ (IRs) of the filaments as indicated in plan view (**Figure 5.S6d**) for the solid Bouligand architecture with  $\gamma = 8^\circ$ . Similarly, The horizontal slices (C2,T2) shown in cross-sectional (H8) view in **Figure 5.S6a**, corresponds to the core (i.e., through the interface) and interfacial regions (IRs) of the filaments as indicated in plan view (**Figure 5.S6b**) for the solid Bouligand architecture with  $\gamma = 8^\circ$ . Analysis of **Figures 5.S6b,d** indicates that porosity (appearing in these figures as darker regions within the hardened cementitious matrix as indicated by arrows) are only present in the images representing slices (T1, T2) through the interface (i.e., they are absent from images representing slices through the cores, C1 and C2). The typical horizontal slices of C1, C2, T1, T2 demonstrate the homogeneous characteristics of the microstructure along the cores (C1, C2), compared to the heterogeneous characteristics of the microstructure along the IRs where interfacial porosity is present (T1, T2).

The observation interfacial porosity is typical in IRs and the cores in both prism and disc elements and was made possible due to the differences in the gray level intensities between the signals from the core sections and interfaces of the filaments in the micro-CT. Application of micro-CT characterization technique for 3D-printed solid Bouligand architecture and prism demonstrates the presence of the processing-induced interfacial heterogeneities and that it can follow the architectural pattern. While these heterogeneities can give rise in anisotropic properties and mechanical response of architected hcp elements, they are utilized in this chapter, to allow the spread of the damage through this heterogeneous network of IRs. Fine-tuning of the interfacial strength via optimization of processing and printing parameters, environmental conditions can allow better control of the mechanical response of the elements. The equivalent strength of the hcp filament and the interface found in **Figure 5.S2** can be of considerable prominence. The interfacial strength, due to its equivalence to filaments strength would not sacrifice the overall strength of the element and therefore allows 3D-printed prisms to obtain similar MOR compared to cast counterparts as discussed in **Figure 5.2a**.

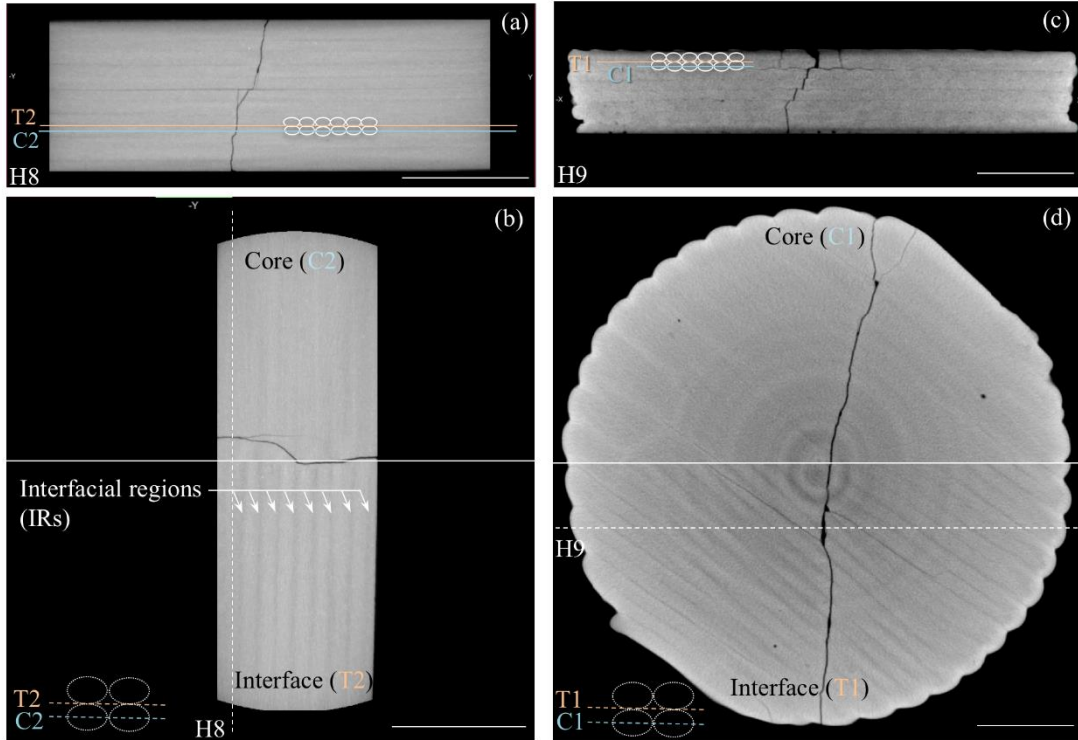


Figure 5.S3. X-ray micro CT image of the microstructure of the core (i.e. through the center) and interfacial regions (collected during 4X scan) of a solid prism with  $0^\circ$  filament orientation in, a) cross-sectional view and, b) plan view and, a solid Bouligand architecture with  $\gamma = 8^\circ$  in, c) cross-sectional view and, d) plan view; and All scale bars are 10 mm long.

#### ***Micro-CT Characterization of the Prism (with $0^\circ$ filament orientation, Figure 5.S4)***

To investigate the role of the interface in damage mechanisms, the microstructural of a solid hardened cement paste prism with  $0^\circ$  filament orientation (**Figure 5.S4a,b1,b2,c,d**) was characterized using micro-CT (in both 0.4X and 4X scan), and damage in the prism was assessed. The 3D rendition of the interior of the solid prism in 0.4X scan of the entire prism and the volume of the region of interest (ROI) near the main crack of the prism in the 4X scan is illustrated in **Figure 5.4Sa.1** and **Figure 5.4Sa.2**, respectively.

Micro-cracking at the interfacial regions in the cross-section of the prism (H6) near the main crack (as shown in **Figure 5.S4b1**) is illustrated in **Figure 5.S4b2** in a 0.4X CT. As outlined in the dashed white rectangle and pointed out with arrows, the micro-cracking demonstrated from the tip of the main crack through the interface and is propagated along the horizontal and vertical IRs.

The Micro-CT of the ROI in the 4X scan reveals further information about propagation of micro-cracks along the IRs (**Figure 5.S4c,d**). The slice (H7) shown in **Figure 5.S4d**, corresponds

to the cross-section of the ROI in XZ plane (**Figure 5.S54**). The hairline micro-cracking at the IRs (appearing thin hairline dark regions) was observed to be present near a micro-crack and to propagate at the horizontal and vertical IRs as shown by the arrows in **Figure 5.S4c**.

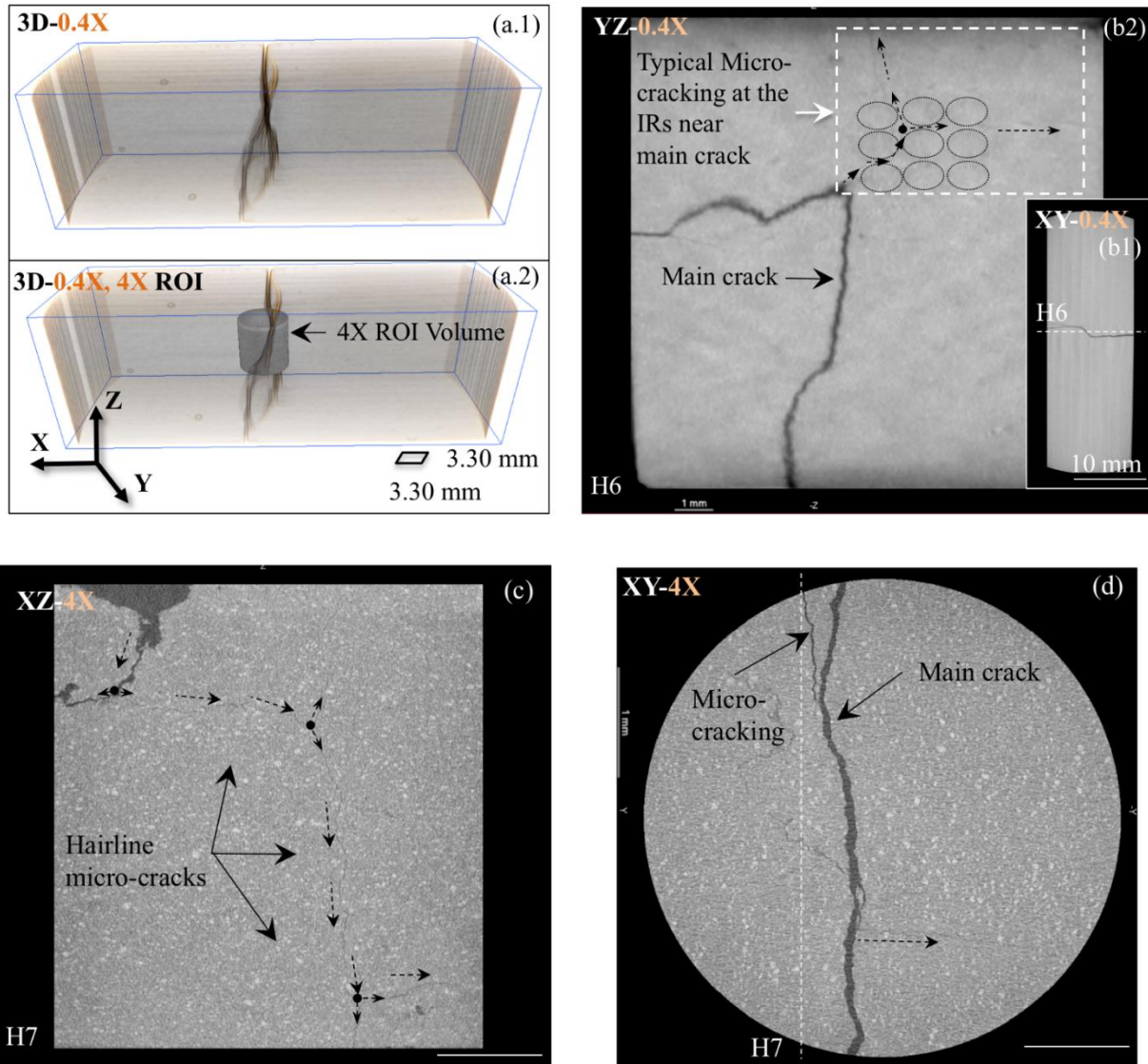


Figure 5.S4. X-ray micro-CT images of the microstructure of post-fracture solid prim specimen with  $0^\circ$  filament orientation collected during 0.4X scan: a.1) 3D rendition of the entire volume of specimen in 0.4X scan and corresponding volume of the region of interest (ROI) in the 4X scan, a.2) 3D rendition of the entire volume of specimen including the cylindrical region of interest (ROI) for 4X scan, b.1) 2D image of the cross-section in YZ plane in 0.4X scan, b.2) 2D image of the cross-section in XY plane in 0.4X scan, c) 2D images in the XZ plane in 4X scan and, d) 2D images in the XY plane in 4X scan. Unless indicated, all scale bars are 1 mm.

***Comparison of Strength and Work of failure (WOF) between Bouligand Architecture and Cast Specimens (Figure 5.S5)***

The mechanical properties (MOR and WOF) of solid and cellular Bouligand architectures versus cast counterparts presented in **Figure 5.2c**, is further elucidated in **Figure 5.S5a,b**. In terms of work of fracture, when the average WOF of cellular Bouligand architectures specimens of pitch angles  $\gamma = 90^\circ, 45^\circ$ , and solid Bouligand architectures specimens of  $\gamma = 8^\circ$  (as outlined in the light blue in **Figure 5.S5a**) were compared with that of solid cast specimens (as outlined in the light grey in **Figure 5.S5a**), a statistically significant enhancement of the Bouligand architectures was found. This significant enhancement indicates that both solid ( $\gamma = 8^\circ$ ) and cellular ( $\gamma = 90^\circ, 45^\circ$ ) architectures can provide significantly enhanced work of failure compared to cast elements.

In terms of strength, when the average Specific MOR of Bouligand architectures specimens with various pitch angles including  $\gamma = 15^\circ, 30^\circ, 45^\circ, 90^\circ$  (i.e., cases where  $\gamma \geq 15^\circ$  as outlined in the light blue in **Figure 5.S5b**) were compared with that of solid cast specimens (as outlined in the light grey in **Figure 5.S5b**), no statistically significant loss of Specific MOR was found. This demonstrates that most cases of Bouligand architectures (where  $\gamma \geq 15^\circ$ ) could maintain specific MOR compared to cast elements.

Although larger pitch angles do not exhibit interfacial damage mechanisms and rather show cracking through the filament, the enhanced WOF in cellular cases where  $\gamma \geq 45^\circ$  and solid case with  $\gamma = 8^\circ$ , demonstrates that larger pitch angles allow for solid failure in the filaments and on itself can provide higher fracture properties as a promising architected structure. The comparison of strength and work of failure between Bouligand architectures and monolithic cast hcp specimen provides supporting evidence that architected hcp can provide significant enhancement without compromising the strength. We surmise that low pitch angles, that allow crack propagation along the interfaces leading to twisting crack patterns, will be more efficient for larger specimens where delocalization can be promoted.

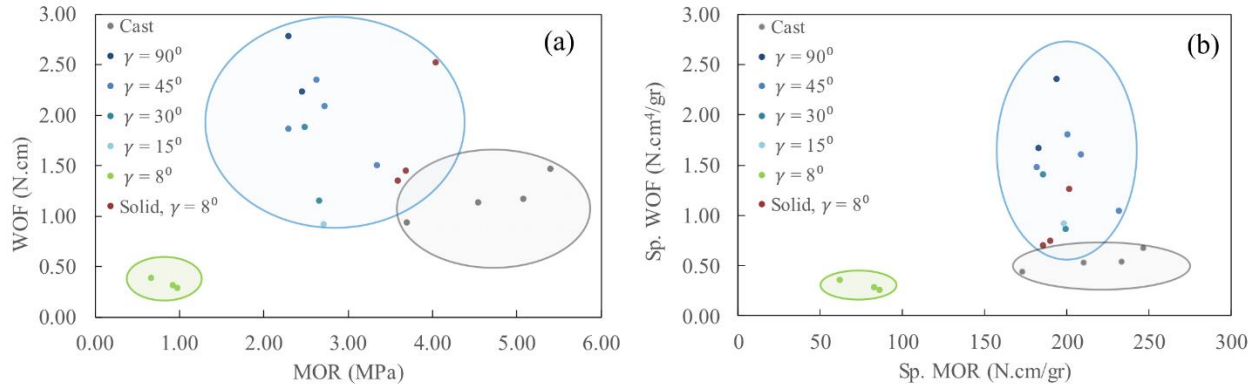


Figure 5.S5. a) Specific WOF vs. Specific MOR and, b) WOF vs. MOR of the cast specimens (outlined in grey), Bouligand architecture specimens with varying pitch angles  $\gamma = 8^\circ$  (solid),  $15^\circ$ ,  $30^\circ$ ,  $45^\circ$ ,  $90^\circ$  (outlined in blue), and solid Bouligand architecture specimens with 60% infill and pitch angles  $\gamma = 8^\circ$  (outlined in green)

***Micro-CT Characterization of Solid Bouligand Architecture (with  $\gamma = 8^\circ$  and 100% infill, Figure 5.S6)***

To investigate the role of the interface in damage mechanisms, the microstructure of a solid hardened cement paste Bouligand architecture disc (**Figure 5.S6a,b,c,d**) was characterized using micro-CT (in 0.4X magnification) and the interfacial damage mechanisms were investigated. These mechanisms are illustrated in **Figure 5.S6b,c,d** for XY, XZ, YZ planes and in **Figure 5.S6a** for 3D rendition of the interior of the solid Bouligand architecture. In micro-CT images of fractured hcp, cracks, micro-cracks and voids correspond to darker greyscale intensities [72].

The slices (H1 to H5 in XZ plane in **Figure 5.S6c**, and K1 to K5 in YZ plane in **Figure 5.S6d**) shown in the XY plane in **Figure 5.S6b**, corresponds to the cross-section of the solid Bouligand architecture with  $\gamma = 8^\circ$  in XZ (**Figure 5.S6c**) and YZ planes (**Figure 5.S6d**), respectively. Micro-cracking at the IRs (appearing darker regions near the main crack) was observed between the layers 6 and 7 (H1, to H3, K1 to K5), layers 4 and 5 (H2 to H5), and layers 3 and 4 (H4, H5) as depicted in **Figure 5.S6c,d** and pointed out by arrows. This micro-cracking is typically spread in both directions throughout the IRs. Moreover, crack advancement at the interfacial regions (appearing dark regions with broader width than micro-cracks) was observed between layers 3 and 4 (H4, H5, K1 to K3) and layers 4 and 5 (K4) as depicted in **Figure 5.S6c,d**, and the orange layer numbers. The cracking advancement through the interface was resulted in

crack staggering (as shown in **Figure 5.S6a.2**) and accompanied by micro-cracking at the interface. It is surmised that the characteristics of porous IRs (as discussed in **Figure 5.S3c,d**), favors the growth along the interfaces. Although an equivalent interfacial and materials strength was found (**Figure 5.S2**), the micro-cracking and crack advancement through the interface can be attributed to its porous characteristics and lower strength and toughness at a smaller scale (i.e. that macroscopic scale).

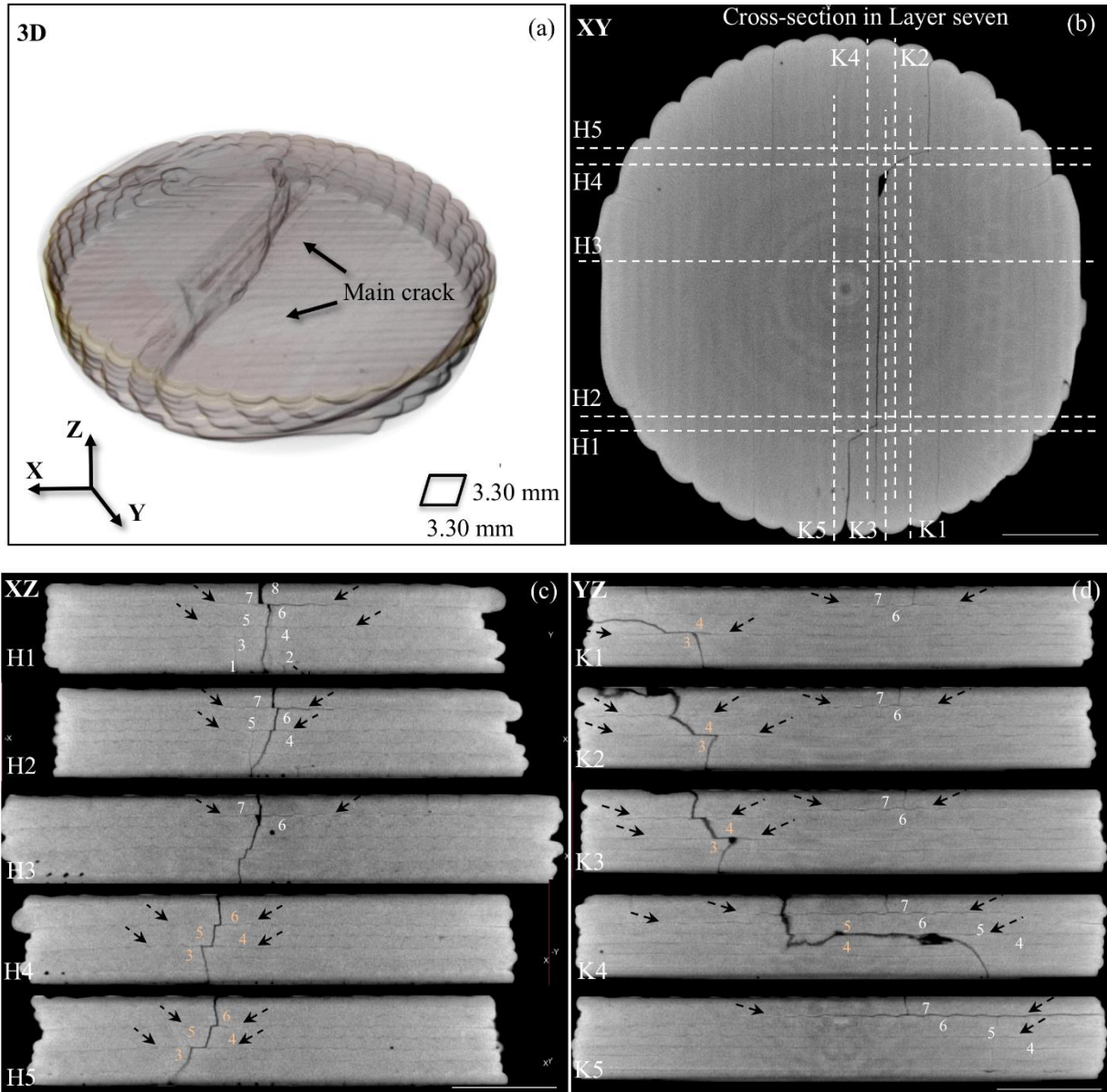


Figure 5.S6. X-ray micro-CT images of the microstructure of post-fracture solid Bouligand architecture with  $\gamma = 8^\circ$  specimen collected during 4X scan: a) 3D rendition of the entire volume of specimen, b) 2D image of the cross-section in layer seven in XY plane, c) 2D images in the XZ plane d) 2D images in the YZ plane. Unless indicated, all scale bars are 10 mm long.

The spread of the damage observed in this Bouligand element here using micro-CT (similar to those observed in **Figure 5.4a3-a8** using optical microscopy), alludes on the role of the interface in control of the crack growth. In turns, Bouligand architectures will lead to crack twisting. When the crack front aligns towards the plane perpendicular to the load direction, due to local twisting, a local hardening effect can take place which precludes further growth of the crack, and therefore

promotes initiation and growth in other neighboring sites. This delocalization helps the spread of the damage in larger volumes and can lead to flaw-tolerant behaviors.

### ***Determination of Extrusion Rate of Cementitious Ink***

The shear rate of the cementitious ink during extrusion at the tip of the nozzle was determined using following equation [70,71]:

$$\dot{\gamma} = \frac{4Q}{\pi r^3} \quad (S1)$$

Where  $Q$ , is the volumetric flow rate during extrusion at the tip of the nozzle with internal radius  $r$  equal to 0.68 mm. The value of flow rate was determined by measuring the mass of extruded materials over a specified time period and calculating the volumetric flow rate based on the density of extruded paste. The paste was extruded over 15 minutes and the mass of was measured as 8.86 g. The density of the extruded paste was separately determined as  $2.28 \pm 0.06 \text{ g cm}^{-3}$ . The flow rate is calculated as  $4.62 \text{ mm}^3 \text{ s}^{-1}$ . The strain rates during extrusion were then calculated based on equation 1, resulting in  $\dot{\gamma}$  equal to  $18.70 \text{ s}^{-1}$ . The corresponding viscosity of the cementitious ink at this shear rate can be determined at this sheared.

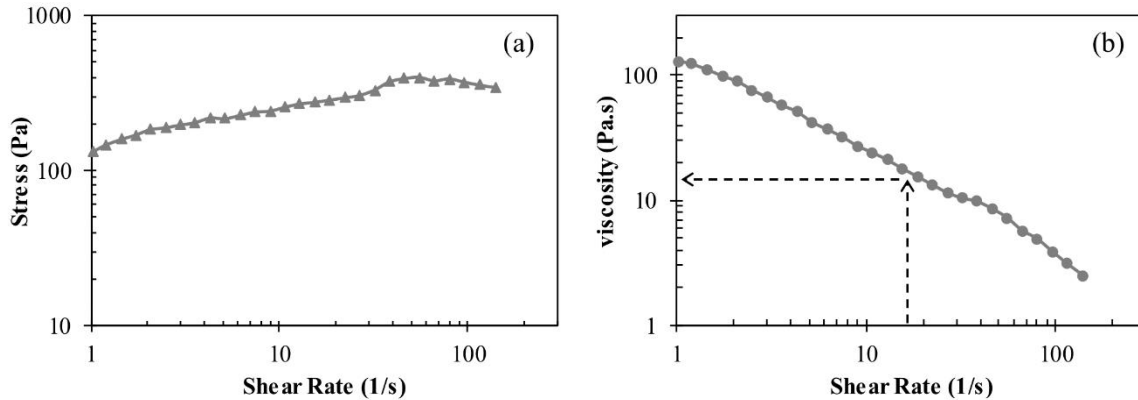


Figure 5.S7. a) Shear stress and, b) viscosity as function of shear rate of the cementitious ink

***Comparison of Competing Mechanisms in Bouligand architectures with small ( $\gamma = 8^\circ$ ) and large ( $\gamma = 45^\circ$ ) pitch angles demonstrated in 3D rendition upon Micro-CT processing (Figure 5.S7)***

The Micro-CT characterization of a cellular Bouligand architecture with large pitch angle  $\gamma = 45^\circ$  is compared with that of small solid pitch angle ( $\gamma = 8^\circ$ ) in order to evaluate the damage mechanisms in small and large pitch angles (**Figure 5.S8**, Videos S15-S18). The shear failure of the filaments at this large pitch angle (**Figure 5.S7a,b**, and **Videos 5.S15-S18**) demonstrates the crack propagation through the filament. In contrast (as discussed in Figure S6), the interfacial damage mechanisms are present at the small pitch angle ( $\gamma = 8^\circ$ ) and crack twisting was allowed (**Figure 5.S7c,d**). Comparison of the small and large pitch angles demonstrate the capacity of small pitch angle to promote damage and flaw-tolerant behavior.

**Ink Rheological Properties: Yield Stress and Viscosity (Figure S8)**

The rheological behavior of cementitious ink is shown in **Figure 5.S8**. Stress and viscosity were obtained as a function of shear rate by measuring shear stress for controlled shear rates in ascending order at a fixed temperature of 23.6 °C (**Figure 5.S8a,b**). Shear rates were increased logarithmically from 1 s<sup>-1</sup> to 140 s<sup>-1</sup>. A water trap was used to minimize drying of the suspension during testing. The samples were pre-sheared each time at 50 s<sup>-1</sup> for 30 s and followed by a 10 s resting time during which no shear was applied. Three replicate tests were performed. The obtained stress and shear rate were fitted to Bingham model as follow to estimate the yield stress:

$$\tau = \tau_0 + \mu \dot{\gamma} \quad (S2)$$

where  $\tau$ ,  $\tau_0$ ,  $\mu$  and  $\dot{\gamma}$  are shear stress (Pa), yield stress (Pa), viscosity (Pa.s), and shear rate (s<sup>-1</sup>).

The average static yield stress of 143.0 Pa was found based on the fitted linear Bingham model. The viscosity of the ink corresponding to the shear rate of 18.70 s<sup>-1</sup> (calculated based on Equation 1) was determined by interpolating the data corresponding to **Figure 5.S8b**. An average viscosity of 15.9 Pa.s was found.

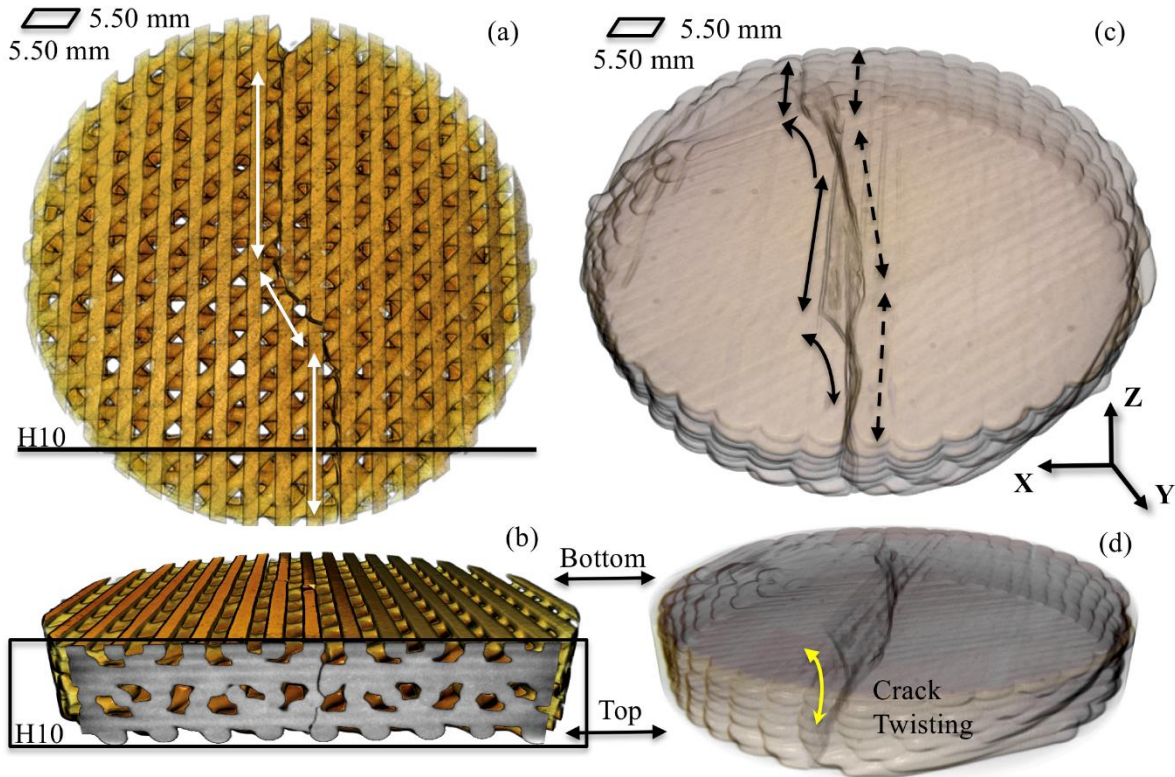


Figure 5.S8. X-ray micro-CT images of the microstructure of post-fracture Bouligand architectures collected during 4X scan: a,b) 3D rendition of the entire volume of specimen with 60% infill and  $\gamma = 45^\circ$  demonstrating crack path through the filaments: c,d) 3D rendition of the entire volume of specimen 100% infill and  $\gamma = 8^\circ$  demonstrating crack twisting through the cross section. Dash black arrows represent the crack path at the top and solid black arrows represent crack path at the bottom of the specimen.

### Videos 5.S1-S18

Video 5.S1-S4: Bouligand architecture with  $15^\circ$ ,  $30^\circ$ ,  $45^\circ$ ,  $90^\circ$  pitch angle

$15^\circ$ : <https://youtu.be/2nu2tPTiTbQ>

$30^\circ$ : <https://youtu.be/6UuSuF4Eiz0>

$45^\circ$ : [https://youtu.be/VwkH\\_8jyGBQ](https://youtu.be/VwkH_8jyGBQ)

$90^\circ$ : <https://youtu.be/0nTWdgNsxeU>

Video 5.S5,S6: Two typical compliant structure

[https://youtu.be/M2\\_U4e5p9TI](https://youtu.be/M2_U4e5p9TI)

<https://youtu.be/PNfEP1z2Se4>

Video 5.S7-S9: Sandwich panel beams with closed top and bottom face

<https://youtu.be/ahOkzXWCzSY>

<https://youtu.be/gjx-aQ9oEj4>

<https://youtu.be/q4qNOJmoIKk>

Video 5.S10: Grid structure

<https://youtu.be/8DW6l7EfkP4>

Video 5.S11: 3D rendition of solid Bouligand architecture with 8° pitch angle upon micro-CT processing

<https://youtu.be/nWq6YUegEKc>

Video 5.S12: XY view of the 2D slices of solid Bouligand architecture with 8° pitch angle upon micro-CT processing

<https://youtu.be/X8gBezIEfXw>

Video 5.S13: XZ view of the 2D slices of solid Bouligand architecture with 8° pitch angle upon micro-CT processing

[https://youtu.be/5u5EY\\_0tWV0](https://youtu.be/5u5EY_0tWV0)

Video 5.S14: YZ view of the 2D slices of solid Bouligand architecture with 8° pitch angle upon micro-CT processing

<https://youtu.be/7oshAJOi32A>

Video 5.S15: 3D rendition of the Cellular Bouligand architecture with 45° pitch angle upon micro-CT processing

<https://youtu.be/l2PIKQKpJjg>

Video 5.S16: XY view of the 2D slices of solid Bouligand architecture with 45° pitch angle upon micro-CT processing

<https://youtu.be/KlcFeBvGYas>

Video 5.S17: XZ view of the 2D slices of cellular Bouligand architecture with 45° pitch angle upon micro-CT processing

<https://youtu.be/0YXX4e-2pqA>

Video 5.S18: YZ view of the 2D slices of cellular Bouligand architecture with 45° pitch angle upon micro-CT processing

<https://youtu.be/ChQcDmeDHpc>

Video 5.S19: Processing-induced heterogeneities at the Interfacial Regions (IRs) of 3D-printed hardened cement paste upon X-ray Micro-CT Processing (Filament height is 1 mm)

<https://youtu.be/NhbKg2xOBd4>

## 5.6 References

- [1] U. G. Wegst, H. Bai, E. Saiz, A.P. Tomsia, R. O. Ritchie, *Nat. Mater.* 2015, *14*, 23.
- [2] E. B. Duoss, T.H. Weisgraber, K. Hearon, C. Zhu, W. Small, T.R. Metz, J.J. Vericella, H. D. Barth, J.D. Kuntz, R. S. Maxwell, C.M. Spadaccini, *Adv. Funct. Mater.* 2014, *24*, 4905.
- [3] J. P. Lewicki, J. N. Rodriguez, C. Zhu, M.A. Worsley, A.S. Wu, Y. Kanarska, J.D. Horn, E. B. Duoss, J. M. Ortega, W. Elmer, R. Hensleigh, 2017, *Sci. Rep.* 7, 43401.
- [4] B. G. Compton, J. A. Lewis, *Adv. Mater.* 2014, *26*, 5930.
- [5] K. T. Sullivan, C. Zhu, E. B. Duoss, A. E. Gash, D. B. Kolesky, J. D. Kuntz, J.A. Lewis, C.M. Spadaccini, *Adv. Mater.* 2016, *28*, 1934.
- [6] A.S. Gladman, E.A. Matsumoto, R. G. Nuzzo, L. Mahadevan, J. A. Lewis, *Nat. Mater.* 2016, *15*, 413.
- [7] C. Gosselin, R. Duballet, P. Roux, N. Gaudillière, J. Dirrenberger, P. Morel, *Mater. Des.* 2016, *100*, 102.
- [8] S. Bukkapatnam, J. Mander, S. Paal, ZJ. Pei, L. Zeng, *NSF Worksh. on Addit. Manuf. for Civ. Infr. Des. and Constr.*, Washington D.C., (July, 2017).
- [9] D. Ouyang, N. Li, L. Liu, *J. Alloys Compd.* 2018, *740*, 603.
- [10] D. Herzog, V. Seyda, E. Wycisk, C. Emmelmann, *Acta Mater.* 2016, *117*, 371.
- [11] J.R.C. Dizon, A.H. Espera, Q. Chen, R.C. Advincula, *Addit. Manuf.* 2017, *20*, 44.
- [12] J.T. Cantrell, S. Rohde, D. Damiani, R. Gurnani, L. DiSandro, J. Anton, A. Young, A. Jerez, D. Steinbach, C. Kroese, P.G. Ifju, *Rapid Prototyping J.* 2017, *23*, 811.
- [13] X. Zheng, W. Smith, J. Jackson, B. Moran, H. Cui, D. Chen, J. Ye, N. Fang, N. Rodriguez, T. Weisgraber, C.M. Spadaccini, *Nat. Mater.* 2016, *15*, 1100.
- [14] K. Christensen, B. Davis, Y. Jin, *Y. Mater. Sci. Eng. C*, 2018, *89*, 65.
- [15] M. DeVries, G. Subhash, A. Mcghee, P. Ifju, T. Jones, J. Zheng, V. Halls, *J. Eur. Ceram. Soc.* 2018, *38*, 3305.
- [16] G.X. Gu, M. Takaffoli, M.J. Buehler, *Adv. Mater.* 2017, *29*.

- [17] M. R. Mansouri, H. Montazerian, S. Schmauder, J. Kadkhodapour, *Compos. Struct.* 2018, *184*, 11.
- [18] L.R. Meza, D. Satyajit, J.R. Greer. *Sci.* 2014, *345*, 1322.
- [19] M. G. Rashed, M. Ashraf, R.A.W. Mines, P.J. Hazell, *Mater. Des.* 2016, *95*, 518.
- [20] J. Bauer, S. Hengsbach, I. Tesari, R. Schwaiger, O. Kraft, *Proc. Natl. Acad. Sci.* 2014, *111*, 2453.
- [21] C. Lv, X.C. Sun, H. Xia, Y.H. Yu, G. Wang, X.W. Cao, S.X. Li, Y.S. Wang, Q.D. Chen, Y.D. Yu, H.B. Sun, *Sens. Actuators, B*, 2018, *259*, 736.
- [22] A. Zolfagharian, A.Z. Kouzani, S.Y. Khoo, B. Nasri-Nasrabadi, A. Kaynak, *Sens. Actuators, A*. 2017, *265*, 94.
- [23] P.T. Smith, A. Basu, A. Saha, A. Nelson, *Polym.* 2018, DOI: 10.1016/j.polymer.2018.01.070.
- [24] P. Shakor, J. Sanjayan, A. Nazari, S. Nejadi, *Constr. Build. Mater.* 2017,*138*, 398.
- [25] B. Zareian, B. Khoshnevis, *Automat. Constr.* 2017, *83*, 212.
- [26] B. Panda, S. C. Paul, M. J. Tan, *Matter. Lett.* 2017, *209*, 146.
- [27] S. C. Paul, Y.W. D. Tay, B. Panda, M. J. Tan, *Arch. Civ. Mech. Eng.* 2018, *18*, 311.
- [28] T. T. Le, S. A. Austin, S. Lim, R. A. Buswell, R. Law, A. GF. Gibb, T. Thorpe, *Cement. Concrete. Res.* 2012, *42*, 558.
- [29] J. J. Biernacki, J. W. Bullard, G. Sant, K. Brown, F.P. Glasser, S. Jones, T. Ley, R. Livingston, L. Nicoleau, J. Olek, F. Sanchez, *J. Am. Ceram. Soc.* 2017, *100*, 2746.
- [30] W. Gao, Y. Zhang, D. Ramanujan, K. Ramani, Y. Chen, C.B. Williams, C.C. Wang, Y.C. Shin, S. Zhang, P.D. Zavattieri, *Comput. Aided Des.* 2015., *69*, 65.
- [31] B. Zareian, B. Khoshnevis, *Automat. Constr.* 2017, *81*, 112.
- [32] G. Franchin, P. Scanferla, L. Zeffiro, H. Elsayed, A. Baliello, G. Giacomello, M. Pasetto, P. Colombo, *J. of Eur. Ceram. Soc.* 2017, *37*, 2481.
- [33] A. Perrot, D. Rangeard, A. Pierre, *Mater. Struct.* 2016, *49*, 1213.
- [34] D. D. Higgins, J. E. Bailey, *J. Mater. Sci.* 1976, *11*,1995.
- [35] N. B. Eden, J. E. Bailey, *J. Mater. Sci.* 1984, *19*, 150.
- [36] L. J. Struble, P.E. Stutzman, E.R. Fuller, *J. Am. Ceram. Soc.*, 1989, *72*, 2295.
- [37] M. Hambach, D. Volkmer, *Cem. Concr. Compos.* 2017, *79*, 62.
- [38] P. Feng, X. Meng, J.F. Chen, L. Ye, *Constr. Build. Mater.* 2015, *93*, 486.

- [39] Harsh, S., Shen, Z. and Darwin, D., 1990.
- [40] T. Ficker, IOP Conf. Ser.: Mater. Sci. Eng. 2017, 1.
- [41] J.D. Birchall, A.J. Howard, K. Kendall, *Nature*, 1981, 289, 388.
- [42] V. C. Li, M. Maalej, Y.-M. Lim, in *Fracture of Brittle Disordered Materials: Concrete, Rock and Ceramics* (Eds: G. Baker, B. L. Karihaloo), CRC Press, New York, 2004, Part 2.
- [43] L.J. Gibson, M. F. Ashby. *Cellular solids: structure and properties*, Cambridge university press, 1999.
- [44] Y. Zhang, H. Yao, C. Ortiz, J. Xu, M. Dao, *J. Mech. Behav. Biomed. Mater.* 2012, 15, 70.
- [45] E. Lin, Y. Li, J.C. Weaver, C. Ortiz, M.C. Boyce, *J. of Mater. Res.* 2014, 29, 1867.
- [46] H. Ming-Yuan, J.W. Hutchinson, *Int. J. Solids Struct.* 1989, 25, 1053.
- [47] M.Y. He, A.G. Evans, J.W. Hutchinson, *Int. J. Solids Struct.* 1994, 31, 3443.
- [48] G. Noselli, V.S. Deshpande, N.A. Fleck, *Int. J. Fract.* 2013, 183, 241.
- [49] C. L. Salinas, E. E. de Obaldia, C. Jeong, J. Hernandez, P. Zavattieri, D. Kisailus, *J. Mech. Behav. Biomed. Mater.* 2017, 76, 58.
- [50] E. E. de Obaldia, C. Jeong, L.K. Grunfelderb, D. Kisailus, P. Zavattieri, *J. Mech. Behav. Biomed. Mater.* 2015, 48, 70.
- [51] J.C. Weaver, G.W. Milliron, A. Miserez, K. Evans-Lutterodt, S. Herrera, I. Gallana, W.J. Mershon, B. Swanson, P. Zavattieri, E. DiMasi, D. Kisailus, 2012 *Sci.* 336, 1275.
- [52] Suksangpanya, N., Doctoral Thesis, Purdue University, December, 2016.
- [53] N. Suksangpanya, N. A. Yaraghi, D. Kisailus, P. Zavattieri, *J. Mech. Behav. Biomed. Mater.* 2017, 76, 38.
- [54] N. Suksangpanya, N. A. Yaraghi, R. B. Pipes, D. Kisailus, P. Zavattieri, *Int. J. Solids Struct.* 2018, DOI: 10.1016/j.ijsolstr.2018.06.004
- [55] L.K. Grunfelder, N. Suksangpanya, C. Salinas, G. Milliron, N. Yaraghi, S. Herrera, K. Evans-Lutterodt, S.R. Nutt, P. Zavattieri, D. Kisailus, *Acta Biomater.* 2014, 10, 3997.
- [56] L.K. Grunfelder, S. Herrera, D. Kisailus, *Crustacean-Derived Biomimetic Components and Nanostructured Composites. Small*, 2014, 10, 3207.
- [57] Chen, X., Wu, S. and Zhou, J., *Constr. Build. Mater.* 2013, 40, 869.
- [58] E. Munch, M.E. Launey, D.H. Alsem, E. Saiz, A.P. Tomsia, R.O. Ritchie, *Sci.* 2008, 322, 1516.
- [59] S. W. Cranford, A. Tarakanova, N.M. Pugno, M.J. Buehler, *Nat.* 2012, 482, 72.

- [60] R.O. Ritchie, *Nat. Mater.*, 2011, *10*, 817.
- [61] ASTM C150 – 17, Standard Specification for Portland Cement.
- [62] ASTM C494 – 16, Standard Specification for Chemical Admixtures for Concrete.
- [63] M. Moini, *Master's thesis*, University of Wisconsin-Milwaukee, August, 2015.
- [64] L. Rueschhoff, W. Costakis, M. Michie, J. Youngblood, R. Trice, *Int. J. Appl. Ceram. Technol.* 2016, *13*, 821.
- [65] N. G. McCrum, C. P. Buckley, C. B. Bucknall, *Principles of Polymer Engineering*, Oxford University Press, New York 1997.
- [66] ASTM C1161 – 13, Standard Test Method for Flexural Strength of Advanced Ceramics at Ambient Temperature.
- [67] A. Börger, P. Supancic, R. Danzer, *J. of Eur. Ceram. Soc.* 2002, *22*, 1425.
- [68] A. Börger, P. Supancic, R. Danzer, *J. of Eur. Ceram. Soc.* 2004, *24*, 2917.
- [69] Y. Cao, P. Zavaterra, J. Youngblood, R. Moon, J. Weiss, *Cem. Concr. Compos.* 2015, *56*, 73.
- [70] J.S. Magdeski, *J. Univ. Chem. Technol. Metall.* 2010. *45*, 143.
- [71] L.F. Nielsen, *J. Am. Ceram. Soc.* 1990, *73*, 2684.
- [72] M. Moini, J. Olek, B. Magee, P. Zavattieri, J. Youngblood, 1<sup>st</sup> Rilem Int. Conf. on Concr. and Dig. Fab., Zurich, (September, 2018).
- [73] S. C. De Wolski, J. E. Bolander, E. N. Landis, 2014, *Exp. Mech.* *54*, 1227.

## **6. INFLUENCE OF INTERNAL ARCHITECTURES ON MECHANICAL RESPONSE AND FRACTURE BEHAVIOR OF 3D-PRINTED CEMENT-BASED ELEMENT UNDER COMPRESSIVE LOAD**

This chapter contains experimental data collected by Mohamadreza Moini. Fabian Rodriguez assisted with the fabrication of 3D-printed elements and conducting mechanical testing. Data conceptualization was a collaborative effort with Jan Olek, Jeffrey P. Youngblood, and Pablo D. Zavattieri. The manuscript was written by Mohamadreza Moini and the Jan Olek, Jeffrey P. Youngblood, and Pablo D. Zavattieri provided editing.

### **Highlights**

- Layer-wise 3D-printing and materials architecture determines the mechanical response and fracture behaviors.
- In lamellar architecture, nearly straight vertical cracks localized at the pre-existing weak interfaces were observed filaments.
- In Bouligand architecture, widespread helical delocalization of cracks into smaller microcracks was observed.
- Using Bouligand architecture allowed for higher energy dissipation capacities, maintaining a steady post-peak, and increase in inelastic deformation without sacrificing the strength.

### **Abstract**

Direct-ink-writing (DIW) is a 3D-printing process that provides the opportunity for patterning the materials' architecture in a layer-by-layer fashion. However, exploiting this opportunity requires establishing a fundamental understanding of the relationship between the materials' architecture and the resulting mechanical properties. Moreover, the role of the processing-induced interfaces on the fracture behavior of the architected elements is not well understood. This chapter investigates the compressive mechanical properties and fracture behaviors of 3-days old hardened cement paste (hcp) elements. Cubical cement paste elements were 3D-printed into two bio-inspired architectures known as 'lamellar' and 'Bouligand' using a DIW process. A lab-based X-ray microscope (XRM) was used to characterize the crack pattern of

lamellar, Bouligand, and reference cast hcp elements upon testing. The mechanical properties/response and the role of the processing-induced interfaces (between the filaments and layers) on fracture behaviors are discussed. The internal architecture and the presence of the interface were found to dictate and alter the overall mechanical response and fracture behaviors in brittle hcp materials. While no specific fracture pattern was observed in the cast element, specific fracture behavior of the lamellar element was dominated by interfacial cracking, aligned with the orientation of filaments, and the fracture behavior of Bouligand element was dominated by a distributed interfacial cracking, aligned with the helical orientation of filaments. Bouligand architecture can be used to improve both work-of-fracture properties and allow for crack delocalization by promoting the spread of the damage in 3D-printed hcp elements.

**Keywords:** Architected hardened cement paste, Interfaces, Fracture behavior, 3D-Printing

## 6.1 Introduction

There has been an exponential rise in the fabrication of brittle cement-based [1–5], geopolymeric [6–10], and ceramic [11–14] materials using 3D-printing technologies. Several studies have demonstrated that 3D-printing allows for purposeful control of the materials' architecture (i.e., the purposeful arrangement of internal geometries of materials) and potential enhancement of mechanical properties such as fracture toughness, energy absorption, strain recovery, impact resistance, and load-bearing capacity [15–19]. Particularly, the ability to fabricate cement-based materials with complex forms and architectures via 3D-printing has resulted in novel mechanical responses and unique performance characteristics [20–23]. However, the presence of processing-induced heterogeneities such as weak and layered interfaces [24] in brittle materials such as cement paste has remained a major challenge and has posed concerns in terms of mechanical properties [25–30]. More specifically, several researchers have intended to eliminate or strengthen the interfaces in 3D-printed cement-based materials due to its weak characteristics [31–33], while some others have attempted to harness the weak interface by tying it to the materials' architecture to control the mechanical response [20,22,34]. Nevertheless, there seems to be a great deal of ambiguity on the role of the interfaces on the mechanical responses of cement-based materials as well as lack of converging research on the best way to approach the interfaces. This chapter investigated the compressive mechanical properties and fracture behaviors of architected

brittle cement paste elements with weak interfaces induced during the 3D-printing process. Two types of nature-inspired internal architectures: “lamellar” and “Bouligand” were used to investigate the mechanical properties of 3D-printed hardened cement paste (hcp) elements in comparison with reference cast hcp elements. A lab-based X-ray microscope (i.e., not requiring synchrotron facilities). Subsequently, the property-fracture was used to investigate the cracking pattern in fractured lamellar, Bouligand, and reference cast elements. The following were examined: (a) the compressive stress-strain behavior, compressive strength, and work-of-failure, and (b) the characteristics of cracks using an XRM.

## 6.2 Methods

### 6.2.1 3D-Printing, Slicing, and Design

A 3D printer capable of printing cement paste via layer-by-layer extrusion process with two separate units was previously established by the authors and was used in this work [24]. A standard Nordsen nozzle (gauge 15 with 1.36. I.D.) was used for depositing materials with a width of 1.63 mm. Similarly, a commercially available slicer (Simplify3D) was used to generate the G-code commands. A slicing procedure was previously established by the authors and was used in this work [24]. A cubical 3D object (25x25x25 mm cube) was inserted in the slicer to design the printing paths necessary to achieve the desired lamellar and Bouligand elements. The geometrical parameters (including filament height, width, and orientation at each layer) and processing parameters (such as printing speed, extrusion multiplier, and infill percentage) were assigned using the slicer. A continuous printing path in each layer was designed to create lamellar and Bouligand elements, as shown in **Figure 6.1a.1,b1**. A rotation angle (also known as pitch angle  $\gamma$ ) of  $3^\circ$  per layer (in the Z direction) was used to create a helical rotation form in the design of the Bouligand elements (**Figure 6.1b.1**). To achieve a toolpath for solid specimens (as shown in **Figure 6.1a.2,b2**), 100% infill was used for both lamellar and Bouligand architectures. A layer height (filament height) of 1.00 mm and the extrusion width of 1.63 were specified in the slicer (using a nozzle with of I.D. of 1.36 mm). The specified printing speed was 250 mm/min., resulting in a speed of 93 s per layer. Each layer was exposed to the environment for a duration between 9.6 s to 186 s. A schematic cross-section of the lamellar and Bouligand architectures was shown for clarity

in **Figure 6.1a.3,b.3**. The resulting 3D-printed lamellar and Bouligand elements were shown in **Figure 6.1.a4-b4**.

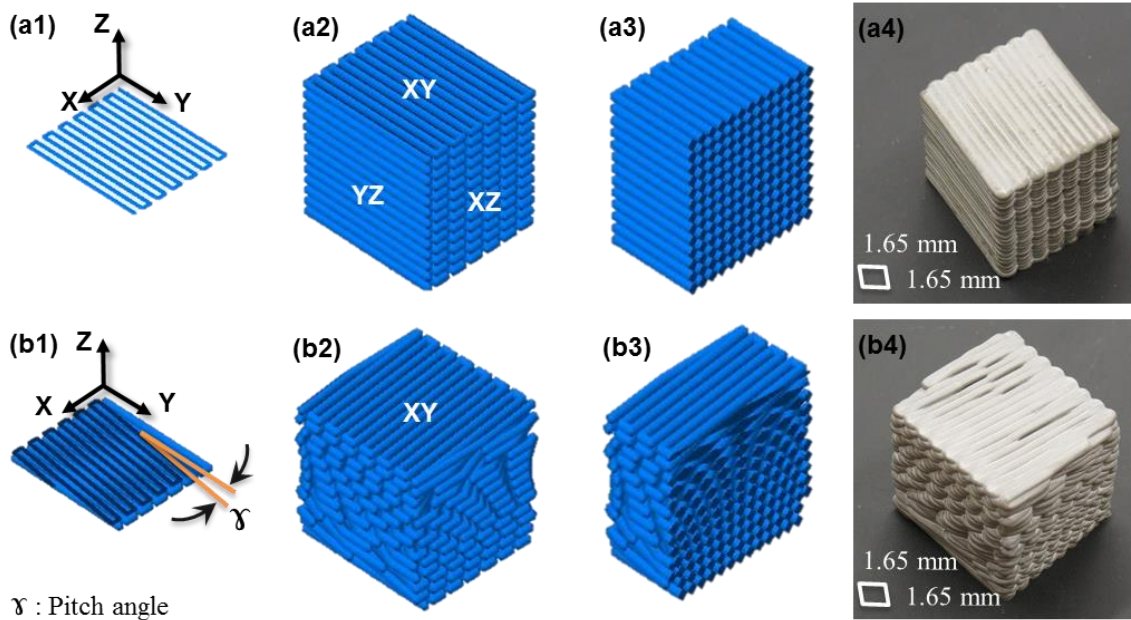


Figure 6.1. Schematics of printing path and resulting 3D-printed specimens with (a1-a4) lamellar architected element and (b1-b4) Bouligand architected elements: (a1) schematics of printing path of individual layers of lamellar architecture; (b1) Schematics of printing path of individual layers of Bouligand architecture (with pitch angle of  $\gamma = 3^\circ$  in Z direction); (a2,b2) schematics of printing path of the entire elements; (a3) schematics of the cross-section of the elements; (a4) resulting 3D-printed lamellar and Bouligand architected elements.

## 6.2.2 Ink Design, Mixing Procedure, and Curing

The final ink used in this work consisted of the sub-150  $\mu\text{m}$  fraction of commercially available Type I cement (ASTM C150 [35]) obtained from Buzzi Unicem, USA; deionized water; HRWRA (MasterGlenium 7700), and VMA (MasterMatrix 362). For each 250.0 grams of cement, 65.2, 1.1 and 3.0 grams of deionized water, HRWRA and VMA were used, respectively. A mixing and materials handling procedure using Twister Evolution Venturi vacuum mixer was previously developed by authors and was used in this work [36]. The specimens were 3D-printed and cast in a lab environment at  $18 \pm 3^\circ\text{C}$  and  $45 \pm 5\%$  relative humidity. Immediately after printing (or casting), the specimens were placed in a curing container in which the temperature of  $18 \pm 3^\circ\text{C}$  and the relative humidity of  $93 \pm 2\%$  (by using a saturated solution of potassium nitrate) was kept

constant for 3 days when the specimens were taken out of the curing chamber for micro-CT characterization.

### **6.2.3 Sample Preparation and Mechanical Testing**

To examine the compressive properties, the specimens were tested in uniaxial compression using an MTS machine with stainless steel platens. A loading rate of 0.1 mm/min was used for all specimens. The 3D-printed lamellar elements were tested in all three planes (i.e., XY, XZ, and YZ), and the 3D-printed Bouligand elements were tested in the XY plane (as indicated in **Table 6.1**). It must be noted that the XY testing plane was the same plane in which layers were printed in both architectures. All cast and 3D-printed specimens were tested at the age of 3 days. All specimens were polished ground using silicon carbide powder to remove surface flaws and obtain flat and parallel surfaces with  $\pm 0.1$  mm tolerance prior to testing. Stress-strain curves were obtained by loading all specimens up to 0.7 mm extension corresponding to a strain of 0.028 strain (mm/mm). The peak load was used in the strength calculations, and the area under the curve corresponding to a 20% drop of the peak load was used for the determination of WOF. Specific compressive strength (Sp. C.S.) and specific work-of-failure were used to take into account the internal porosities, and corresponding densities of each element.

### **6.2.4 Micro-Computed Tomography (Micro-CT) of Fractured Elements**

In this study, a Zeiss Xradia 510 Versa X-ray microscope (XRM) was utilized for qualitative analysis of the fractured cast, lamellar, and Bouligand elements. The fractured cast element, three 3D-printed lamellar elements, and a 3D-printed Bouligand element was characterized using 0.4X geometric magnification scan (initial lower resolution) to allow for a large FOV and thus facilitated capturing the tomographic view of the entire element. The geometric magnification involved setting distances between the source, detector, and element. The resolutions of 33.01, 34.86, 31.74, 34.35, 34.35  $\mu\text{m}$  pixel size was used for the scans of the fractured cast, lamellar (tested in XY, YZ, XZ planes), and Bouligand (tested in XY plane), respectively. The beam energies of 110, 120, 120, 100, and 100 keV, the power levels of 10, 10, 10, 9, and 9 W, and exposure times of 1, 0.6, 1, 0.75, and 0.75 s were used for the scans of the fractured cast, lamellar (tested in XY, YZ, XZ planes),

and Bouligand (tested in XY plane), respectively. Dragonfly software was used for post-processing and visualization of the 2D and 3D images.

### 6.3 Results and Discussion

#### 6.3.1 Mechanical Properties of Cast and Architected Elements

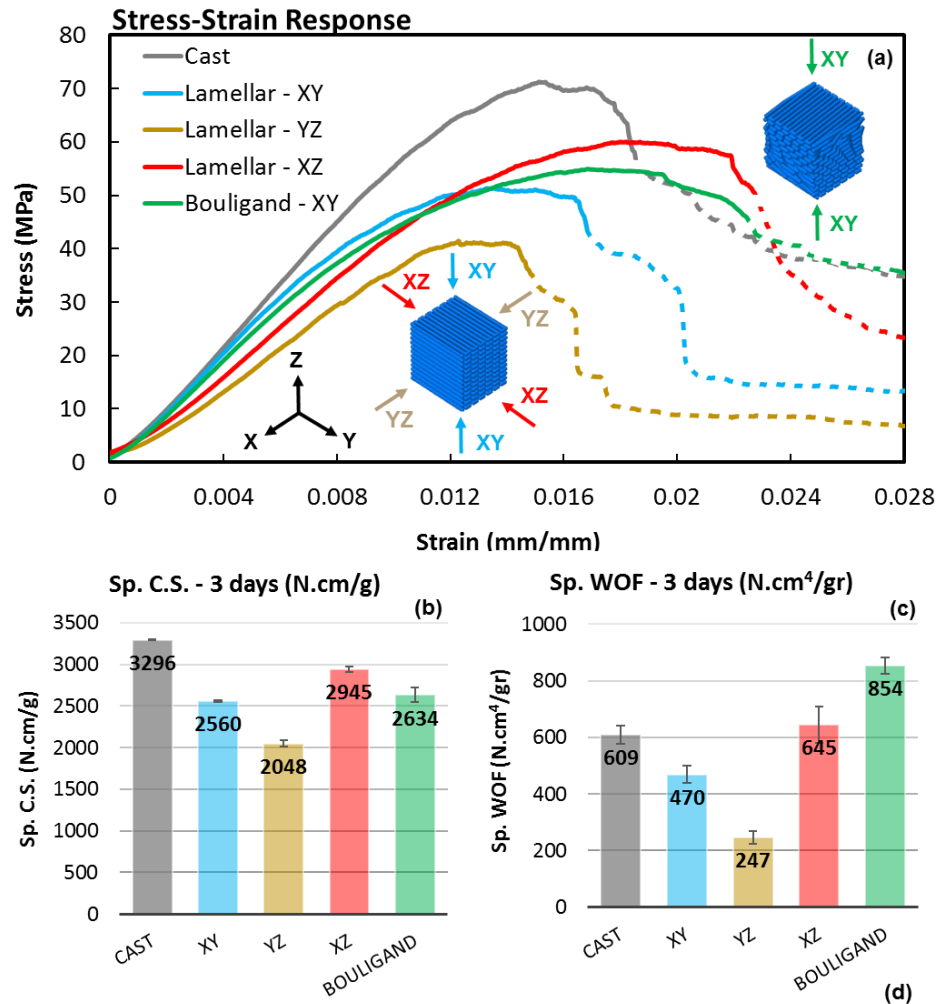
The mechanical response of cast and 3D-printed architected lamellar (tested in XY, YZ, and XZ) and Bouligand (tested in XY) hcp elements were investigated. Rendition of the two architected elements and the testing direction are elaborated in **Table 6.1**. The mechanical responses, including representative stress-strain behavior, specific compressive strength (Sp. C.S.), and specific work-of-failure (Sp. WOF), are reported in **Figure 6.5 a-d**.

Table 6.1. Rendition of the cast, 3D-printed lamellar, and 3D-printed Bouligand elements and their respective plane in which they were tested (shown in dashed lines) in uniaxial compression (dash lines represent testing plane)

Elements	Testing Planes (in dashed lines)
Cast	
Lamellar	
Lamellar	
Lamellar	
Bouligand	

### 6.3.2 Stress-Strain Behavior

The comparison of representative stress-strain behavior demonstrated several distinct differences in the overall mechanical response between the cast, and 3D-printed lamellar and Bouligand elements (**Figure 6.2.a**). The cast elements demonstrated a stress-strain behavior notably different than all the 3D-printed architected elements.



Specific Work of Failure (Sp. WOF)					
	Cast	XY	YZ	XZ	Bouligand
Cast		Non-Sig.	Sig.	Non Sig.	Sig.
Lamellar - XY	Sig.		Sig.	Sig.	Sig.
Lamellar - YZ	Sig.	Sig.		Sig.	Non-Sig.
Lamellar - XZ	Non Sig.	Sig.	Sig.		Sig.
Bouligand - XY	Non Sig.	Non Sig.	Sig.	Non Sig.	

Specific Compressive Strength (Sp. C.S.)					
--	--	--	--	--	--

Figure 6.2. Comparison of (a) stress-strain; (b) specific compressive strength (Sp. C.S.) and (c) Specific work-of-failure (Sp. WOF) of the cast, lamellar, and Bouligand architected hcp elements at the age of 3 days quantified up to 20% drop of the peak load; and (d) corresponding statistical differences between them.

The Bouligand elements tested in the XY plane demonstrated a superior overall stress-strain behavior compared to the other two types of 3D-printed elements.

The lamellar elements tested in the XZ plane and the Bouligand element tested in the XY plane demonstrated a superior overall stress-strain behavior compared to the other two types of 3D-printed elements. In terms of strain at maximum stress, the lamellar elements tested in the XZ plane and the Bouligand elements tested in the XY plane also demonstrated higher degrees of deflection compared to cast elements (**Figure 6.5a**). In contrast, the lamellar elements tested in both XY and YZ planes demonstrated a lower degree of deflection compared to cast elements (**Figure 6.5a**). Consequently, the lamellar elements, due to differences in the degrees of deflection and maximum stress, demonstrated three distinct stress-strain behaviors in three testing planes of XY, YZ, and XZ (**Figure 6.5a**). Comparing stress-strain behavior between lamellar and Bouligand elements, both tested in the XY plane demonstrated a significant difference both in terms of stress and deflection (**Figure 6.5a**). Moreover, while Bouligand elements demonstrated a steady post-peak drop in stress levels, all lamellar, including the one tested in the same plane as Bouligand element (XY), exhibited a rather drastic and significant post-peak drop in stress-strain plot (**Figure 6.5a**). A higher degree of post-peak drop was also observed in all lamellar elements in comparison to reference cast elements. In terms of stiffness, no apparent difference between the cast and 3D-printed lamellar and Bouligand elements were observed.

From **Figure 6.5a**, it is evident that lamellar elements exhibited anisotropic compressive mechanical properties. In other words, the testing planes play a substantial role in altering the compressive mechanical responses of lamellar elements (**Figure 6.5a**). Comparing stress-strain behaviors between lamellar and Bouligand elements, both tested in the XY plane, demonstrated the role of the architecture of the material in altering the mechanical response of 3D-printed elements. In a sense, the difference in stress-strain behavior of lamellar elements in different testing planes also revealed further evidence on the role of architecture on changing the mechanical response of 3D-printed elements.

In summary, lamellar and Bouligand elements tested in the same testing plane (XY) demonstrated different stress-strain behaviors in terms of peak load, post-peak behavior, and area under the curve. In a given lamellar element, the arrangement of filaments with respect to the testing plane also results in significantly different stress-strain behaviors.

### 6.3.3 Specific Compressive Strength (Sp. C.S.)

The comparison of specific compressive strength and specific work-of-failure of the cast and 3D-printed elements are presented in **Figure 6.5b** and **Figure 6.5c**, respectively. The result of statistical significance tests for Sp. C.S. and Sp. WOF properties are reported in the lower half of **Figure 6.5d**. The lamellar elements tested in XY and YZ planes demonstrated significantly lower Sp. C.S. compared to the cast elements (**Figure 6.5b**). However, the lamellar elements tested in the XZ plane did not demonstrate any significant difference in Sp. C.S. when compared to the cast (**Figure 6.5b**). No significant difference in the Sp. C.S. of the Bouligand elements tested in XY plane and lamellar architecture tested in the YZ plane with the cast was found. This ‘equivalent’ strength compared to the cast is an interesting feature of the lamellar element when the filaments’ orientation is aligned with the load. Such ‘equivalent’ strength of Bouligand elements compared to the cast was also attributed to the specific helical and layered architecture and will be discussed further in the chapter. Although the lamellar elements tested in the XY and XZ planes also did not demonstrate a significant difference in terms of Sp. C.S. (**Figure 6.5b**), those tested in the YZ plane demonstrated a significantly lower Sp. C.S. with respect to the other lamellar elements tested in the XY and YZ planes (**Figure 6.5b**), all were providing evidence that lamellar hcp elements 3D-printed using a specific DIW process do represent anisotropic compressive strength when tested in uniaxial compression.

### 6.3.4 Specific Work-of-Failure (Sp. WOF)

The highest Sp. WOF among all cast and 3D-printed elements was achieved in Bouligand architectures (**Figure 6.5c**). More importantly, the Bouligand architectures demonstrated a significantly higher Sp. WOF compared to cast counterparts, featuring an outstanding fracture behavior and energy dissipation characteristic of this architecture. Unlike the lamellar elements tested in the YZ plane, the lamellar elements tested in XZ and XY planes did not demonstrate any significant difference Sp. WOF compared to cast elements (**Figure 6.5c**). Although not significant, the Sp. WOF of the lamellar elements tested in the XZ plane was slightly larger than that of the cast elements. This ‘equivalent’ Sp. WOF compared to the cast was also an interesting feature of the lamellar element and has to do with the alignment of the filaments’ orientation with the load. Due to the significant difference in Sp. WOF among 3D-printed lamellar elements, it can be

determined that 3D-printed lamellar elements represent anisotropic Sp. WOF properties, in addition to anisotropic Sp. C.S. discussed earlier.

### **6.3.5 Discussion of the Overall Mechanical Responses**

Lamellar elements exhibited anisotropic compressive strength and work-of-failure. Lamellar elements (tested in XZ plane where the orientation of the lamella is parallel to the loading direction) also demonstrated an interesting feature to maintain the load-bearing capacity at post-peak stress levels compared to the cast elements. Bouligand elements, on the other hand, demonstrated significantly higher work-of-failure and the capacity to maintain the load at post-peak stress levels (without sacrificing the strength) compared to cast counterparts. Hence, it can be stated that the architecture can be potentially utilized as a means to enhance some of the mechanical properties of 3D-printed elements compared to cast elements that were made of the same hcp materials.

In summary, it can be inferred that the Bouligand architecture demonstrated effectiveness in increasing energy dissipation and a promising capacity to maintain the load at post-peak stress levels (as exhibited in the steady post-peak drop in the stress-strain plot in **Figure 6.5a**) at higher levels compared to cast elements. Such favorable characteristics, such as load-bearing capacity and mechanical properties of Bouligand architecture, are mechanically very desirable when achieved without sacrificing the strength (as indicated in **Figure 6.5b**). Nevertheless, identification of underlying mechanisms responsible for different mechanical responses in 3D-printed elements requires investigation of the elements during testing or after the fracture has occurred (i.e., post-mortem). Further discussions followed in the next section will discuss the cracking involved in shaping up the mechanical responses discussed in **Figure 6.5** using an XRM.

### **6.3.6 Fracture Behaviors**

The three cast, lamellar and Bouligand elements tested in the same direction (XY plane) were selected for qualitative analysis of fracture behavior and are presented in **Figures 6.6, 6.7, 6.8**. The two lamellar elements tested in XZ and YZ planes were also analyzed and discussed in **Figure 6.S1** and **Figure 6.S2**, providing supportive information about fracture behavior in lamellar elements.

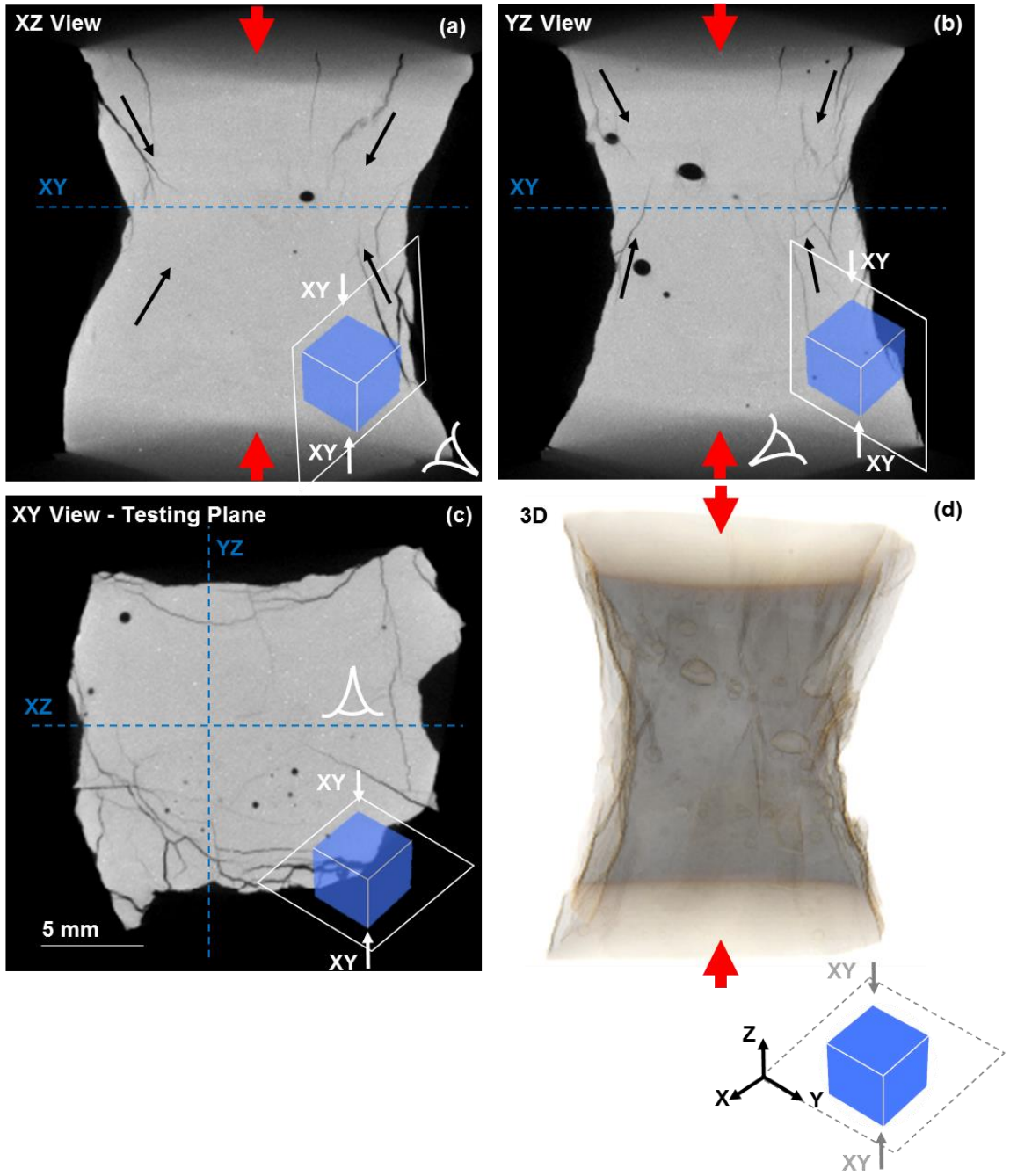


Figure 6.3. Post-fracture X-ray micro-CT images of the microstructure of cast hardened cement paste specimen tested in XY plane and collected during 0.4X scan: (a) 2D view on the XZ plane; (b) 2D view on the YZ plane; (c) 2D view on the XY plane; and (d) three-dimensional rendition of the entire volume of the element.

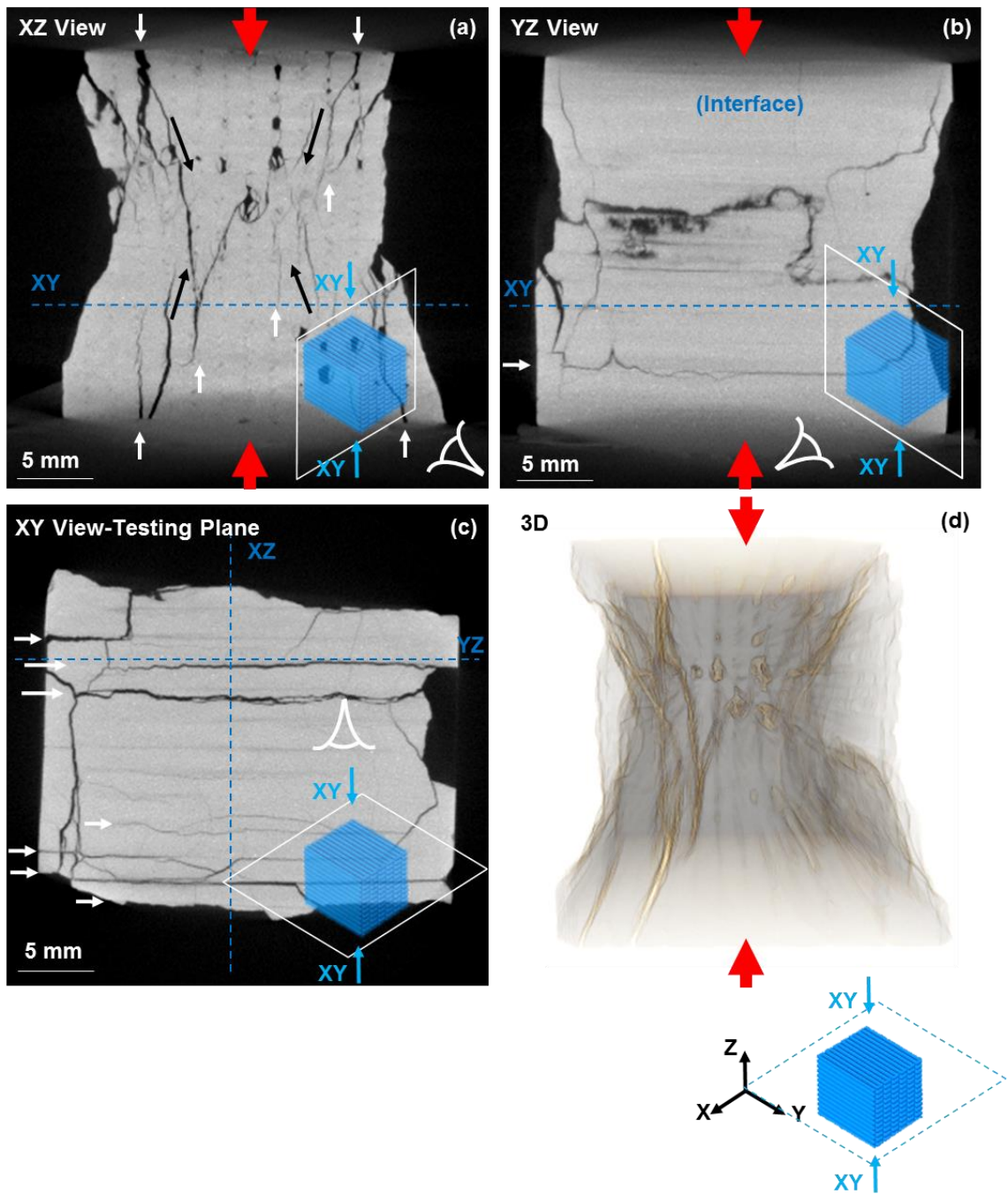


Figure 6.4. Post-fracture X-ray micro-CT images of the microstructure of 3D-printed hardened cement paste specimen with lamellar architecture tested in XY plane and collected during 0.4X scan: (a) 2D view on the XZ plane; (b) 2D view on the YZ plane; (c) 2D view on the XY plane; and (d) three-dimensional rendition of the entire volume of the element.

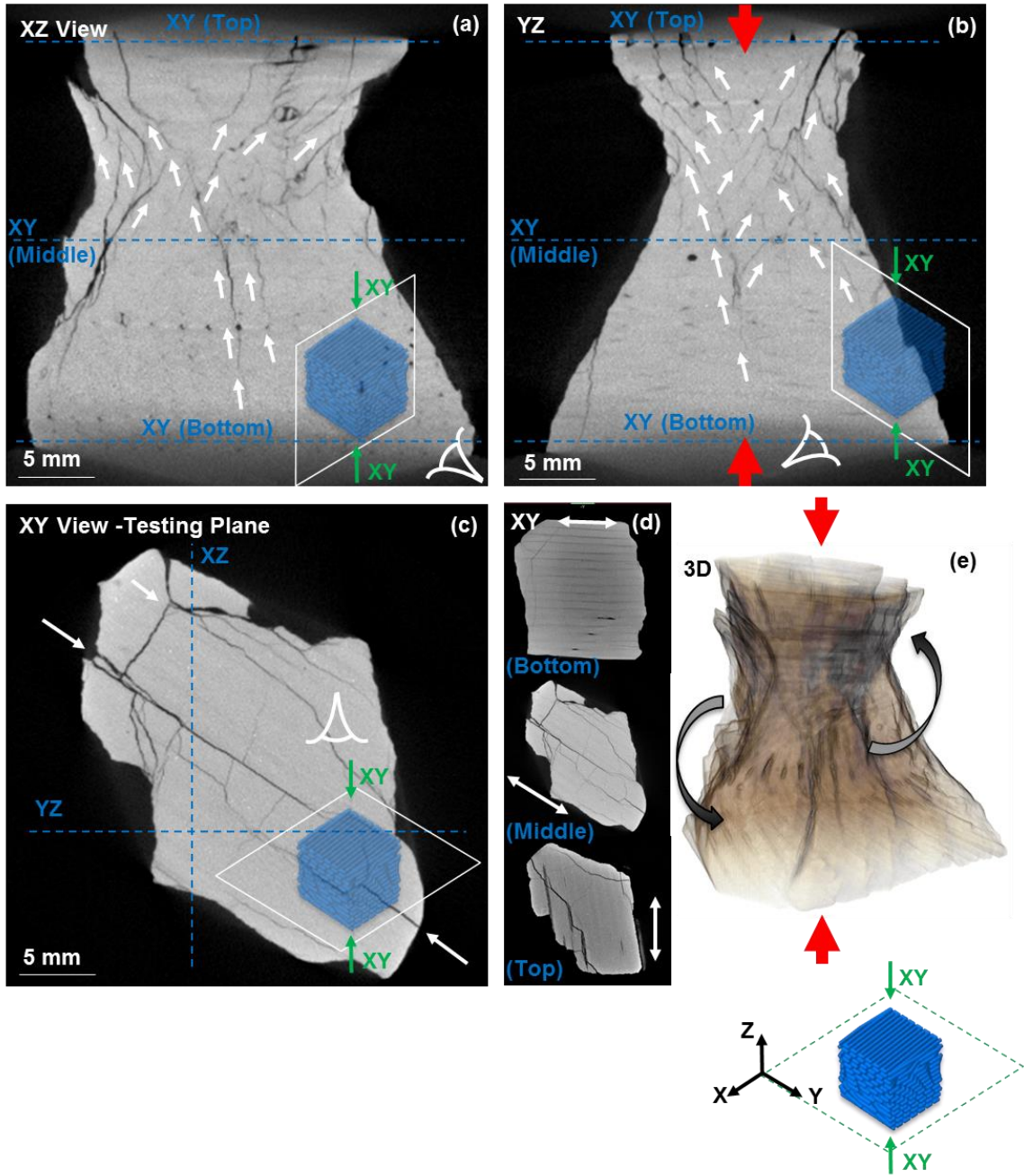


Figure 6.5. Post-fracture X-ray micro-CT images of the microstructure of 3D-printed hardened cement paste specimen with Bouligand architecture tested in XY plane and collected during 0.4X scan: (a) 2D view on the XZ plane; (b) 2D view on the YZ plane; (c) 2D view on the XY plane; (e) 2D view on the XY plane at three different heights of the specimen (f) three-dimensional rendition of the entire volume of the specimen.

### 6.3.7 Cast Element (Tested in XY Plane)

The post-fracture images of the reference cast element are demonstrated in XZ, YZ, XY, and in three-dimensional view in **Figure 6.6a,b,c,d**, respectively. Most importantly, no specific crack pattern was observed in the fractured cast element. A shear cone, as expected in brittle hcp elements (at the presence of friction between the element and the compression platens), was observed at the core of the element. This shear cone is indicative of a shear failure (on oblique planes), as shown with black arrows in **Figure 6.6a,b**. With regard to a pore-crack interaction, it was observed that the majority of the pores have remained undamaged (**Figure 6.6a,b,c**).

### 6.3.8 Lamellar Element (Tested in XY Plane)

The post-fracture images of the 3D-printed lamellar element tested in the XY plane are demonstrated in XZ, YZ, XY, and in three-dimensional views in **Figure 6.7a,b,c,d1,d2**, respectively. Here the element was tested in the same plane that it was printed in layers. As pointed out with white arrows in **Figure 6.7c** (XY view), Several cracks appeared to have localized in the nearly straight vertical form at the interfaces between the filaments of different layers (in the YZ plane). These interfacial cracks in the YZ plane were also visible in the XY view (**Figure 7.a**), as pointed out with white arrows. On the other hand, almost no cracks in the XY plane was populated, as indicated in **Figure 6.7a,b**, respectively. There was only one visible interfacial crack in the YZ plane (**Figure 6.7b**). Another important feature to mark was the formation of a partial shear cone at the core (at about middle one third) of the element that was indicative of a partial shear failure on oblique planes, as shown with black arrows in **Figure 6.7a**. It is important to note that the shear cone was only present in the XZ view, as indicated in **Figure 6.7a,b**, indicating that weak interfaces between the filaments have potentially facilitated a preferential shear failure. The partial shear failure can also be seen in three dimensions in **Figure 6.7d**, where the brighter slits are indicative of cracks in the element upon testing. Most importantly, the overall fracture behavior of the lamellar element here (**Figure 6.7d**) was found distinctively different compared to the cast element, mainly due to the prevalent vertical cracking at the interfaces between the filaments (**Figure 6.6d**).

### 6.3.9 Bouligand Element (Tested in XY Plane)

The post-fracture images of 3D-printed Bouligand elements tested in XY direction are demonstrated in XZ, YZ, XY views, and in three dimensions in **Figure 6.8a-e**. To refresh, Bouligand element here holds a pitch (rotation) angle of  $3^\circ$  per layer in the Z direction. A rather different crack pattern was identified in Bouligand architecture compared to the lamellar architecture. In distinct contrast with lamellar elements, there was a lack of a large number of localized straight vertical cracks at the interfaces here. Instead, the cracks appeared to delocalize into widespread smaller and more distributed microcracks throughout the interfaces of the Bouligand element, in the form of a helical pattern (as demonstrated with white arrows in **Figure 6.8a,b**). However, similar to the lamellar element, a few major cracks have localized at the interfaces between the filaments were also present (as pointed out with white arrows **Figure 8.c**). These internal cracks nonetheless did not take a straight vertical form such as those in the lamellar element and rather followed the helical pattern along the Z direction (**Figure 6.8a,b**). At any given layer in the XY plane (such as the one shown in **Figure 6.8c**), the majority of the populated cracks and microcracks were aligned with the orientation of the architecture in that layer. A similar helical pattern was also evident from exterior surfaces (**Figure 6.8d**). The twisting pattern in the exterior surfaces from the bottom to the top was demonstrated by white arrows in **Figure 6.8d** and black arrows in **Figure 6.8e**. Viewing the exterior of the Bouligand element (in **Figure 6.8a,b**) demonstrated the formation of a shear cone similar to the lamellar element. However, in Bouligand element, the shear failure was accompanied by crack twisting evident from **Figure 6.8d,e**.

### 6.3.10 Discussion on Fracture Behaviors

Three distinct fracture behaviors in the cast, lamellar, and Bouligand elements under compressive loads can be recognized. Cast elements demonstrated an overall fracture behavior with a typical shear cone and no specific cracking pattern (**Figure 6.6**). The presence of shear cone in cast and 3D-printed elements can be attributed to the constraints induced by friction that was present at the contact surfaces between the elements and the plattens. Moreover, the internal flaws in the cast hcp, such as pores, did not generally appear to have served as crack nucleation sites throughout the cast element. Lamellar and Bouligand elements, on the other hand, each demonstrated unique fracture behaviors, unparalleled to the cast. Lamellar element demonstrated

a rather frequent population of straight vertical cracks at the interfaces between the filaments, accompanied by the formation of a partial shear cone at the core (**Figure 6.7**). The abundant presence of localized cracks, patterned in the vertical planes, indicated that the interfaces are weaker than the filament itself (i.e., the hcp material in filament). Based on the evidence provided in Appendix **Figure 6.S1**, it must be noted that the interfaces (both horizontal interfaces between the layers and vertical interfaces between the filaments) are weaker than the material. Moreover, the interfaces between the layers are weaker than the interface between the filaments. Although it is not clear whether the cracks observed in the post-mortem lamellar element were initiated at the interfaces or not (i.e., whether weak interfaces have served as crack nucleation sites), it can reasonably be concluded that the weak interfaces in the intact lamellar element, weaker than the material [24], have contributed to a preferential cracking at the vertical interfaces. The unique fracture behavior of Bouligand element, in contrast to the cast and lamellar elements, was evident from the (i) widespread delocalization of cracks into smaller microcracks, and (ii) their helical pattern (**Figure 8**). Although it is not determined whether weak interfaces have served as crack nucleation sites, it is indisputable that the combination of the weak interfaces and helical architecture with 3° rotation angle has resulted in distributed cracking (i.e., the spread of the damage) and have guided the cracks into the interfaces' helical forms (**Figure 6.8**). The fact that there exists a helical exterior surface (**Figure 6.8d,e**) implies that the guidance of crack through the interfaces must have also been in play at the exterior damaged volume (that was not included in the scanned volume). Distinct fracture behaviors of lamellar and Bouligand elements compared to cast elements have certain ramifications for the mechanical response of the element that is further discussed as follows.

### **6.3.11 Discussion on Fracture Behavior in Relation to Mechanical Properties**

The insight obtained from the fracture behaviors of the cast, lamellar, and Bouligand elements can be used to draw inferences about the corresponding mechanical response. The Sp. C.S. of lamellar elements was superseded by that of the cast elements (**Figure 6.5**). The presence of initially weak interfaces and the resulting vertically patterned localized cracks in lamellar elements (**Figure 6.7**) can be hypothesized to be responsible for the significant reduction in strength in lamellar elements compared to cast. In the case of Bouligand elements, the Sp. WOF significantly superseded that of the cast element (**Figure 6.5**). The widespread delocalization of cracks into smaller microcracks

throughout the core volume observed in the Bouligand elements (**Figure 6.8**) requires a higher amount of energy to be dissipated, which subsequently explains the significantly higher WOF in Bouligand element compared to that of the cast counterpart. In other words, the initiation or propagation of micro-cracks through multiple interfaces of the Bouligand element (**Figure 6.8**) has resulted in a higher amount of energy dissipation compared to reference cast hcp element, in which no interface pre-existed and specific fracture patterned occurred as evident from **Figure 6.6**). In terms of overall mechanical response, the rather prevalent localization of cracks into smaller microcracks throughout the weak interfaces in Bouligand architecture (**Figure 6.8**) also explained the extension of the peak stress toward larger strains as well as the rather steady post-peak behavior (Shown in green in **Figure 6.5.a**), compared to the cast hcp element with the rather drastic post-peak drop. The spread of the damage throughout the element in Bouligand elements can also be the reason for a more ductile behavior of hcp elements under unidirectional compressive load.

More specifically, in Bouligand elements, the pre-existed weak interfaces in a helical form have prevented one major crack from localizing and have resulted in more efficient energy dissipation in this element compared to the cast. Due to the common presence of helical crack patterns in Bouligand elements, a toughening mechanism can be speculated in which the weak interfaces could have been utilized to advance the cracks in twisting patterns. In such a hypothetical case, helical interfaces allow for redistribution of stress and further spread of the damage in multiple weak paths in the element (i.e., homogenizing the damage in the element by spreading it at the interfaces).

## 6.4 Conclusion

This chapter investigated the mechanical properties and fracture behavior of 3D-printed lamellar and Bouligand hardened cement past elements in comparison with cast counterparts. An X-ray microscope was used to characterize the fracture behavior of elements upon testing. It was found that the presence of interfaces (i) introduces anisotropy in mechanical properties among 3D-printed elements and alters the stress-strain response among compared to cast elements, (ii) the interfaces are weaker than the material and the horizontal interfaces between the layers are weaker than the vertical interfaces between the filament, and (iii) promotes unique cracking characteristics (such as large populations of interfacial cracking) in Bouligand architecture. It was

also found that the fracture behavior significantly depends upon not only the internal architecture of the material, but also whether the element is 3D-printed or is cast. The unique load-displacement responses and distinct fracture behaviors of the cast, lamellar, and Bouligand elements indicated of: (i) the widespread helical delocalization of cracks into smaller microcracks in Bouligand, and (ii) the patterned vertical cracks localized at the interfaces in lamellar, both in contrast to the cast elements with no specific crack pattern.

In summary, the type of architecture and the presence of the interface were found to dictate the overall mechanical response and fracture behavior of the 3D-printed lamellar and Bouligand elements. The presence of weak interfaces and the ability to control the architecture via 3D-printing can be used to improve crack delocalization by promoting the spread of the damage at the interfaces in layer-wised 3D-printed elements. More specifically, Bouligand architecture and weak interfaces can be used to enhance one material property (such as work-of-failure) without sacrificing another (strength). The enhanced mechanical properties in compression were achieved by taking advantage of a Bouligand architecture with a small pitch angle ( $\gamma = 3^\circ$ ) and allowing crack delocalization and promoting the spread of the damage in the elements. The authors have previously proven the interfaces were highly porous and weak [24] and that they can be combined with Bouligand architectures in favor of flexural mechanical responses [22]. In conclusion, it was demonstrated that the pre-existing helical porous interfaces of the Bouligand architecture produced during 3D-printing, promoted higher energy dissipation capacities, maintaining of a steady post-peak, and increase in the inelastic deformation, without sacrificing the strength compared to lamellar and cast hcp elements. The results of this chapter provide a new approach for incorporation of the weak interfaces in the design, fabrication, and deployment of patterned cement-based elements via 3D-printing that are under compressive or hydrostatic loads such as columns and piers or submarine infrastructures.

## 6.5 Acknowledgments

The authors gratefully acknowledge the generous support of this research by the National Science Foundation (CMMI Grant 1562927). The authors would like to thank the BASF chemicals company for providing materials. The authors acknowledge fruitful discussions with other members of the collaborative NSF project, Dr. Florence Sanchez of Vanderbilt University, and Dr. Joseph Biernacki of the Tennessee Technological University. The authors would also like to thank

the 2017 Major Multi-User Equipment Program, offered by the Office of the Executive Vice President for Research at Purdue University, for supporting the acquisition of the X-ray microscope (micro-CT) used in data reviewed in this research.

## 6.6 Appendix

### *Fracture Behavior of 3D-Printed Lamellar Element (Tested in XZ Plane)*

The post-fracture images of 3D-printed lamellar element tested in XZ plane are demonstrated in XZ, YZ, XY and in three-dimensional views in **Figure 6.S1.a,b,c,d1,d2**, respectively. In this testing plane, the filaments were loaded in compression in their longitudinal direction as demonstrated with red arrows in **Figure 6.S1.b,c** (i.e., filaments' longitudinal orientation is parallel to with loading direction). As pointed out with white arrows in **Figure 6.S1.a** (XZ view), cracks appear to be present in the straight form at both the interfaces between the layers in the XY plane (as shown with blue dashed line) and interfaces between the filaments of different layers in the YZ plane (as shown with blue dashed line). The presence of numerous cracks at the interfaces indicated that both the interfaces between the layers and the interfaces between the filaments are weaker than the filament itself. However, there was a much higher population of cracks at the interfaces between the layers than between the filaments of different layers (**Figure 6.S1.a**).

Viewing the element in the YZ plane (**Figure 6.S1.b**) demonstrated that there was a formation of a shear cone at the core (the middle one third) of the element that was indicative of a shear failure on oblique planes (as shown with black arrows). Outside the core of the element, this shear cone was accompanied by what appears to be the buckling of filaments at the exterior one-third of the element.

Viewing the element in XY plane (**Figure 6.S1.c**) on the other hand, demonstrated that (i) there are limited number of cracks at the interfaces (compared to numerous ones that can be observed in YZ plane in **Figure 6.S1.b**), (ii) there was a formation of a shear cone at the core (similar to the one observed in YZ view) as pointed out with black arrows, and (iii) there was no buckling on the exterior of the element (compared to the buckling observed in YZ view in **Figure 6.S1.b**). The latter was further elucidated in **Figure S1.d1** and **Figure S1.d2** in a three-dimensional view where the element has buckled in the YZ view but not the XY view.

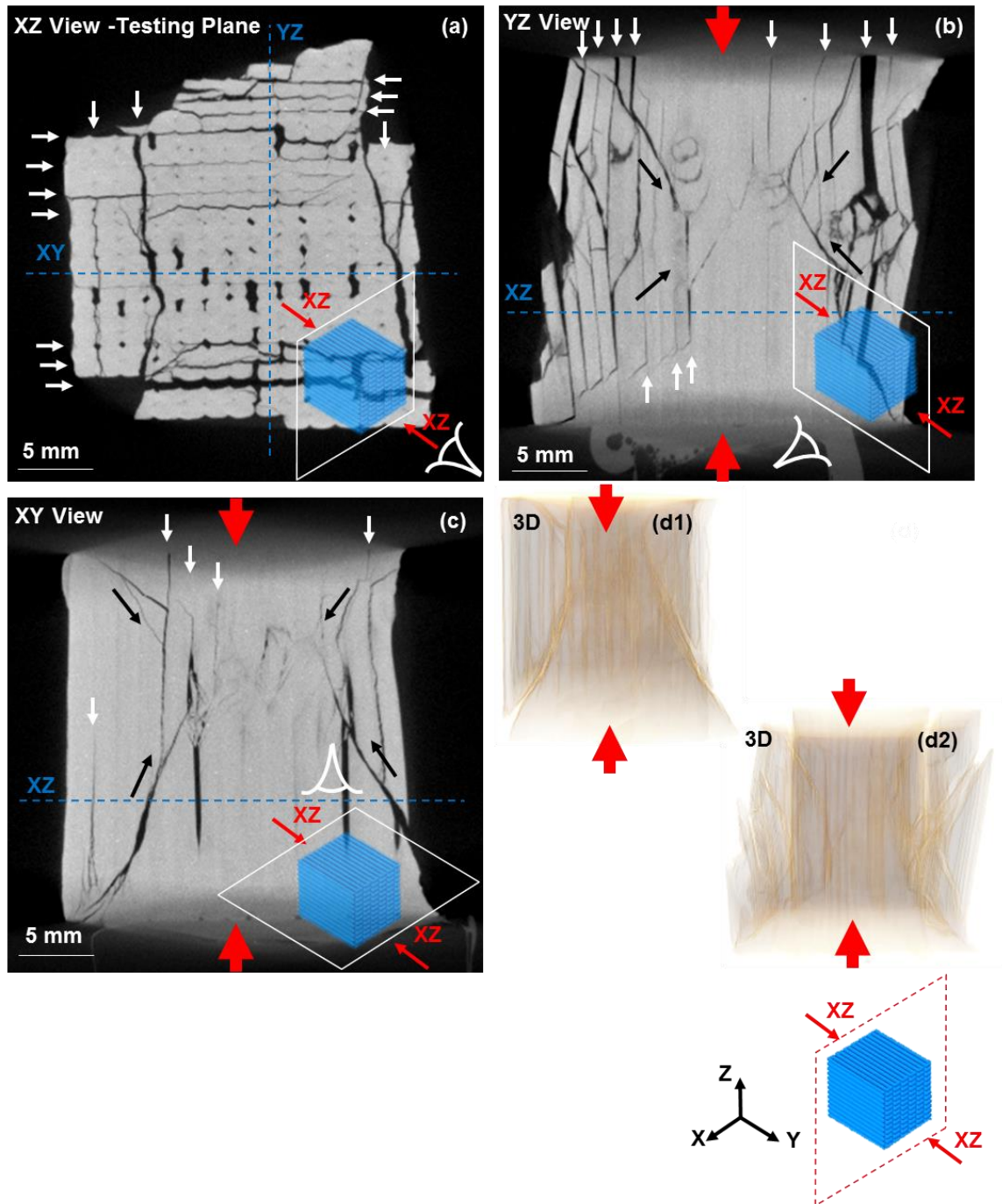


Figure 6.S1. Post-fracture X-ray micro-CT images of the microstructure of 3D-printed hardened cement paste specimen with lamellar architecture tested in XZ plane and collected during 0.4X scan: (a) 2D view on the XZ plane; (b) 2D view on the YZ plane; (c) 2D view on the XY plane; and (d1, d2) three-dimensional rendition of the entire volume of the element.

The overall fracture pattern in lamellar elements tested in the XZ plane is then the numerous population of cracks at the interfaces, principally at the exteriors, accompanied by the formation of a shear cone at the core as demonstrated in **Figure 6.S1.a,b,c**. Consequently, the prevalent crack pattern at the interfaces indicates that fracture behavior, if not pre-dominantly, were at least partially governed by the presence of the weak interfaces. This anisotropic fracture behavior caused by numerous preferential cracking at the interfaces can be correlated with the anisotropic mechanical properties of lamellar architecture tested in YZ direction. More importantly, cracking characteristics in lamellar architecture tested in the XZ plane were discernibly different from those of the cast (**Figure 6.6d, Figure 6.S1.d1,d2**) and the lamellar architecture tested in the other two directions (XY and YZ).

The higher population of cracks at the interfaces between the layers (**Figure 6.S1.b**) compared to the interfaces between the filaments (**Figure 6.S1.c**) can suggest that the interfaces between the layers (present in XY plane) are weaker than the interfaces between the filaments (present in the YZ plane) in the 3D-printed lamellar elements. The distinct presence of buckling phenomena (with associated delamination between the filaments) shown in the **Figure 6.S1.b**, as compared to the limited number of interfacial cracks and the lack of buckling and delamination shown in **Figure 6.S1.c**, also supports the same hypothesis about the weakness of the two interfaces relative to one another.

The interfaces between the layers (present in the XY plane) is weaker than the interfaces between the filaments mainly due to the higher evaporation rate and the presence of higher porosity at interfacial regions between the layers that have pre-existed in the intact elements in this plane. It can be concluded that a longer exposure time (up to  $90 \text{ s} \times 2 = 180 \text{ s}$ ) at the interfaces between the layers compared to that in between the filaments (20 s), could be the reason for higher degree of porosity at the interfaces between the layers. Longer exposure time results in more rapid evaporation and higher scarcity of water (and a possibly lower degree of hydration).

**Figure 6.S1** demonstrated that both interfaces between the filaments/layers are weaker than the material, and the interfaces between the layers are weaker than the interface between the filaments. Given the interfacial fracture pattern, it can be speculated that the presence of interface could have possibly triggered other energy dissipation and toughening mechanisms (other than cracking at the interfaces) such as buckling, delamination, and debonding that would be contributing to the increase of Sp. WOF in lamellar elements tested in this loading direction.

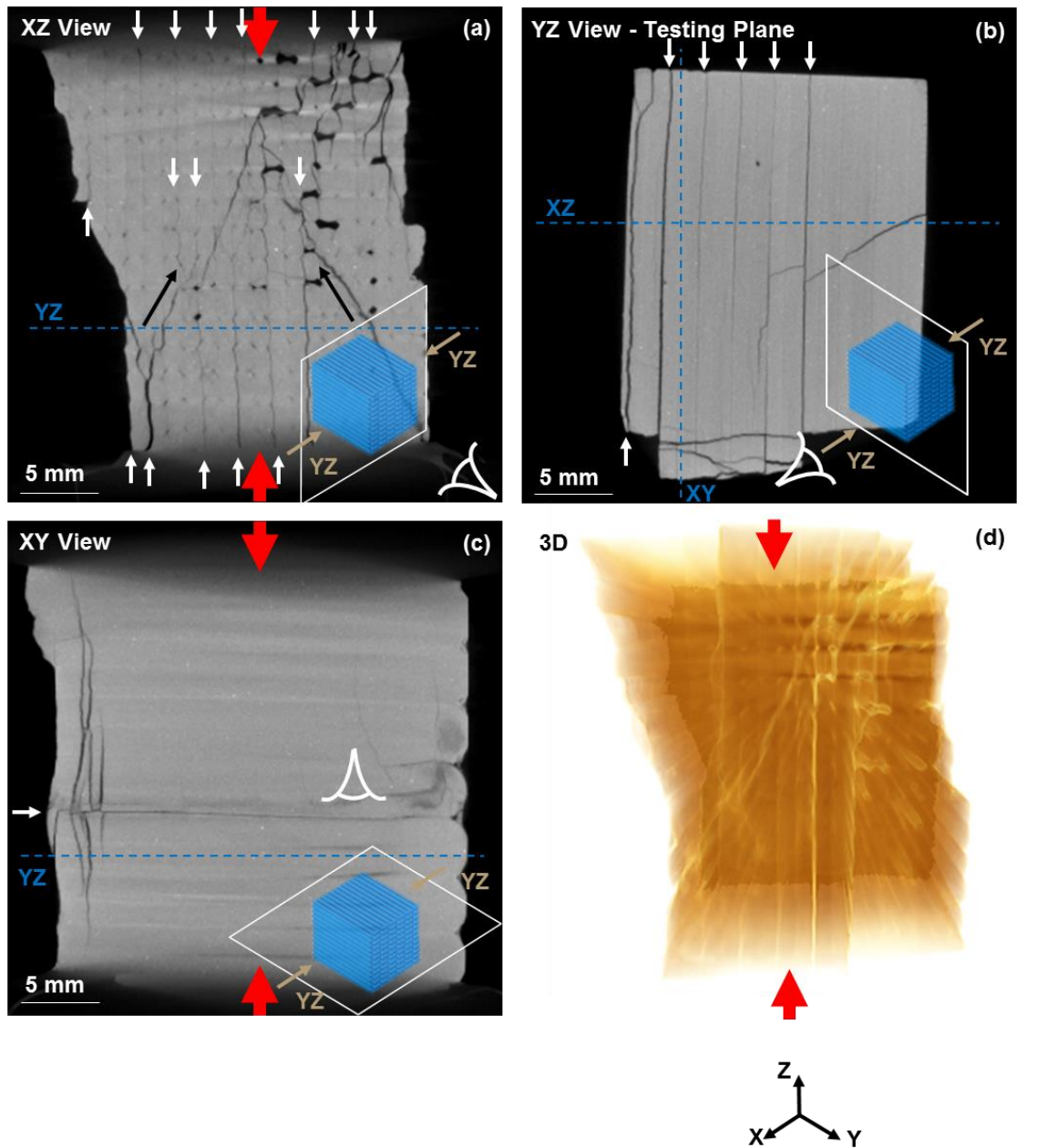


Figure 6.S2. Post-fracture X-ray micro-CT images of the microstructure of 3D-printed hardened cement paste specimen with lamellar architecture tested in YZ plane and collected during 0.4X scan: (a) 2D view on the XZ plane; (b) 2D view on the YZ plane; (c) 2D view on the XY plane; and (d) three-dimensional rendition of the entire volume of the element

### *Fracture Behavior of Lamellar Element (Tested in YZ Plane)*

The post-fracture images of the 3D-printed lamellar element tested in YZ direction were demonstrated in XZ, YZ, XY views, and in three-dimensional view in **Figure 6.S2.a,b,c,d**,

respectively. As pointed out with white arrows in **Figure 6.S2.a** (XZ view), a number of cracks appeared to be present in the straight form at the interfaces between the layers in the XY plane. These interfacial cracks are also visible in **Figure 6.S2.b** (YZ view), as pointed out with white arrows. On the other hand, almost no cracks appear to be populated in the YZ plane at the interface between the filaments of different layers, as indicated in **Figure 6.S2.a,c**. There was only one minor interfacial crack in the YZ plane (**Figure 6.S2.c**). Some other clear features to point out was the formation of a partial shear cone at the core of the element that was indicative of a shear failure on oblique planes (as shown with black arrows in **Figure 6.S2.a**). It is essential to note that a shear cone in this testing direction was only present in XZ view, as indicated in **Figure 6.S2.a,c**. The partial shear cone can also be seen in three dimensions in **Figure 6.7.d**, where the oblique bright slits were indicative of cracks in the microstructure.

The overall fracture pattern in lamellar elements tested in the XY plane was the population of cracks at the interfaces accompanied by the formation of a partial shear cone at the core, as indicated in **Figure 6.S2.a,d**. The presence of interfacial cracks further indicates that the interface between the filaments was weaker than the material itself, and makes the crack pattern in this lamellar element different than the cast elements (**Figure 6.6.d**).

In **Figure 6.S1**, it was discussed that the interface between the layers (present in the XY plane) was weaker than the interface between the filaments of different layers (present in the YZ plane). The common crack patterns at the interfaces between the layers evident from **Figure 6.S2.b**, further supports the hypothesis that the interfaces between the layers were weaker than the material.

## 6.7 References

- [1] C. Gosselin, R. Duballet, P. Roux, N. Gaudillière, J. Dirrenberger, P. Morel, Large-scale 3D printing of ultra-high performance concrete - a new processing route for architects and builders, *Mater. Des.* 100 (2016) 102–109. doi:10.1016/j.matdes.2016.03.097.
- [2] J.J. Biernacki, J.W. Bullard, G. Sant, K. Brown, F.P. Glasser, S. Jones, T. Ley, R. Livingston, L. Nicoleau, J. Olek, F. Sanchez, R. Shahsavari, P.E. Stutzman, K. Sobolev, T. Prater, Cements in the 21 st century: Challenges, perspectives, and opportunities, *J. Am. Ceram. Soc.* 100 (2017) 2746–2773. doi:10.1111/jace.14948.

- [3] S. Lim, R.A. Buswell, T.T. Le, S.A. Austin, A.G.F. Gibb, T. Thorpe, Developments in construction-scale additive manufacturing processes, *Autom. Constr.* 21 (2012) 262–268. doi:10.1016/j.autcon.2011.06.010.
- [4] Ed. By: Sanjayan, J. G., A. Nazari, B. Nematollahi. *3D Concrete Printing Technology: Construction and Building Applications*, Butterworth-Heinemann, 2019.
- [5] Ed. By: A. Perrot. *3D Printing in Concrete: General Considerations and Technologies*, ISTE LTD, 2019.
- [6] M. Xia, J. Sanjayan, Method of formulating geopolymers for 3D printing for construction applications, *Mater. Des.* 110 (2016) 382–390. doi:10.1016/j.matdes.2016.07.136.
- [7] G. Franchin, P. Scanferla, L. Zeffiro, H. Elsayed, A. Baliello, G. Giacomello, M. Pasetto, P. Colombo, Direct ink writing of geopolymeric inks, *J. Eur. Ceram. Soc.* 37 (2017) 2481–2489. doi:10.1016/j.jeurceramsoc.2017.01.030.
- [8] B. Panda, S.C. Paul, N.A.N. Mohamed, Y.W.D. Tay, M.J. Tan, Measurement of tensile bond strength of 3D printed geopolymer mortar, *Meas. J. Int. Meas. Confed.* 113 (2018) 108–116. doi:10.1016/j.measurement.2017.08.051.
- [9] B. Panda, C. Unluer, M.J. Tan, Extrusion and rheology characterization of geopolymer nanocomposites used in 3D printing, *Compos. Part B Eng.* 176 (2019) 107290. doi:10.1016/j.compositesb.2019.107290.
- [10] M. Xia, B. Nematollahi, J. Sanjayan, Printability, accuracy and strength of geopolymer made using powder-based 3D printing for construction applications, *Autom. Constr.* 101 (2019) 179–189. doi:10.1016/j.autcon.2019.01.013.
- [11] S. Xiao, H. Mei, D. Han, W. Yuan, L. Cheng, Porous (SiC w -Si<sub>3</sub>N<sub>4</sub>w)/(Si<sub>3</sub>N<sub>4</sub>-SiC) composite with enhanced mechanical performance fabricated by 3D printing, *Ceram. Int.* 44 (2018) 14122–14127. doi:10.1016/j.ceramint.2018.05.011.
- [12] A. Zocca, P. Colombo, C.M. Gomes, J. Günster, Additive Manufacturing of Ceramics: Issues, Potentialities, and Opportunities, *J. Am. Ceram. Soc.* 98 (2015) 1983–2001. doi:10.1111/jace.13700.
- [13] U.K. Roopavath, S. Malferrari, A. Van Haver, F. Verstreken, S.N. Rath, D.M. Kalaskar, Optimization of extrusion based ceramic 3D printing process for complex bony designs, *Mater. Des.* 162 (2019) 263–270. doi:10.1016/j.matdes.2018.11.054.

- [14] L.R. Meza, S. Das, J.R. Greer, Strong, lightweight, and recoverable three-dimensional ceramic nanolattices., *Science*. 345 (2014) 1322–6. doi:10.1126/science.1255908.
- [15] Z. Jia, L. Wang, 3D printing of biomimetic composites with improved fracture toughness, *Acta Mater.* 173 (2019) 61–73. doi:10.1016/j.actamat.2019.04.052.
- [16] D. Herzog, V. Seyda, E. Wycisk, C. Emmelmann, G.T. Gray, V. Livescu, P.A. Rigg, C.P. Trujillo, C.M. Cady, S.R. Chen, J.S. Carpenter, T.J. Lienert, S.J. Fensin, T. Tancogne-Dejean, A.B. Spierings, D. Mohr, H. Manzano, J.S. Dolado, A. Ayuela, F. Abdeljawad, D.S. Bolintineanu, A. Cook, H. Brown-Shaklee, C. DiAntonio, D. Kammler, A. Roach, A. Pineau, A.A. Benzerga, T. Pardoen, S. Xiao, H. Mei, D. Han, W. Yuan, L. Cheng, C. Zhang, X. Hu, T. Sercombe, Q. Li, Z. Wu, P. Lu, Additive manufacturing of metals, *Acta Mater.* 117 (2016) 371–392. doi:10.1016/j.actamat.2016.07.019.
- [17] M.R. Mansouri, H. Montazerian, S. Schmauder, J. Kadkhodapour, 3D-printed multimaterial composites tailored for compliancy and strain recovery, *Compos. Struct.* 184 (2018) 11–17. doi:10.1016/j.compstruct.2017.09.049.
- [18] X. Zheng, W. Smith, J. Jackson, B. Moran, H. Cui, D. Chen, J. Ye, N. Fang, N. Rodriguez, T. Weisgraber, C.M. Spadaccini, Multiscale metallic metamaterials, *Nat. Mater.* 15 (2016) 1100–1106. doi:10.1038/nmat4694.
- [19] G.X. Gu, M. Takaffoli, M.J. Buehler, Hierarchically Enhanced Impact Resistance of Bioinspired Composites, *Adv. Mater.* 29 (2017) 1–7. doi:10.1002/adma.201700060.
- [20] S.M. Sajadi, P.J. Boul, C. Thaemlitz, A.K. Meiyazhagan, A.B. Puthirath, C.S. Tiwary, M.M. Rahman, P.M. Ajayan, Direct Ink Writing of Cement Structures Modified with Nanoscale Additive, 1801380 (2019) 1–10. doi:10.1002/adem.201801380.
- [21] Y. Xu, H. Zhang, E. Schlangen, M. Lukovi, B. Savija, Cementitious cellular composites with auxetic behavior, 111 (2020). doi:10.1016/j.cemconcomp.2020.103624.
- [22] M. Moini, J. Olek, J.P. Youngblood, B. Magee, P.D. Zavattieri, Additive Manufacturing and Performance of Architected Cement-Based Materials, *Adv. Mater.* 30 (2018). doi:10.1002/adma.201802123.
- [23] J.A. Rosewitz, H.A. Choshali, N. Rahbar, Bioinspired design of architected cement-polymer composites, *Cem. Concr. Compos.* 96 (2019) 252–265. doi:10.1016/j.cemconcomp.2018.12.010.

- [24] M. Moini, J. Olek, B. Magee, P. Zavattieri, J. Youngblood, Additive Manufacturing and Characterization of Architected Cement-based Materials via X-ray Micro-Computed Tomography, in: 1st Rilem Int. Conf. Concr. Digit. Fabr., 2018.
- [25] M. DeVries, G. Subhash, A. Mcghee, P. Ifju, T. Jones, J. Zheng, V. Halls, Quasi-static and Dynamic Response of 3D-printed Alumina, *J. Eur. Ceram. Soc.* 38 (2018) 3305–3316. doi:10.1016/j.jeurceramsoc.2018.03.006.
- [26] H. Xing, B. Zou, S. Li, X. Fu, Study on surface quality, precision and mechanical properties of 3D printed ZrO<sub>2</sub> ceramic components by laser scanning stereolithography, *Ceram. Int.* 43 (2017) 16340–16347. doi:10.1016/j.ceramint.2017.09.007.
- [27] B. Zareiyan, B. Khoshnevis, Interlayer adhesion and strength of structures in Contour Crafting - Effects of aggregate size, extrusion rate, and layer thickness, *Autom. Constr.* 81 (2017) 112–121. doi:10.1016/j.autcon.2017.06.013.
- [28] J.G. Sanjayan, B. Nematollahi, M. Xia, T. Marchment, Effect of surface moisture on inter-layer strength of 3D printed concrete, *Constr. Build. Mater.* 172 (2018) 468–475. doi:10.1016/j.conbuildmat.2018.03.232.
- [29] B. Panda, S. Chandra Paul, M. Jen Tan, Anisotropic mechanical performance of 3D printed fiber reinforced sustainable construction material, *Mater. Lett.* (2017). doi:10.1016/j.matlet.2017.07.123.
- [30] W.R. Leal, D.A. Silva, T.J. Andersen, A. Kudsk, K.F. Jørgensen, 3D Concrete Printing of post-tensioned elements, *Annu. IASS Symp. Creat. Struct. Des.* (2018).
- [31] S.C. Paul, Y.W.D. Tay, B. Panda, M.J. Tan, Fresh and hardened properties of 3D printable cementitious materials for building and construction, *Arch. Civ. Mech. Eng.* (2018). doi:10.1016/j.acme.2017.02.008.
- [32] T.T. Le, S.A. Austin, S. Lim, R.A. Buswell, R. Law, A.G.F. Gibb, T. Thorpe, Hardened properties of high-performance printing concrete, *Cem. Concr. Res.* 42 (2012) 558–566. doi:10.1016/j.cemconres.2011.12.003.
- [33] Y.W.D. Tay, G.H.A. Ting, Y. Qian, B. Panda, L. He, M.J. Tan, Time gap effect on bond strength of 3D-printed concrete, *Virtual Phys. Prototyp.* 0 (2018) 1–10. doi:10.1080/17452759.2018.1500420.

- [34] W.K. J. Mata-Falcón, P. Bischof, Exploiting the Potential of Digital Fabrication for Sustainable and Economic Concrete Structures, (2019) 157–166. doi:10.1007/978-3-319-99519-9.
- [35] ASTM C150 – Standard Specification for Portland Cement (2017), (n.d.).
- [36] M. Moini, J. Olek, B. Magee, P. Zavattieri, J. Youngblood, Additive manufacturing and characterization of architected cement-based materials via X-ray micro-computed tomography, 2019. doi:10.1007/978-3-319-99519-9\_16.

## 7. CONCLUSIONS AND RECOMMENDATIONS

Several hypotheses were examined in the previous five chapters from which a number of inferences were drawn. Chapter two alluded that shear moduli,  $G$ ,  $G^*$ , and  $G'$ , are more relevant rheological property of the material that should be controlled if buckling is the failure mechanism that dominates the buildability of the 3D-printed elements. Specifically, the shear modulus  $G$ , was confirmed to be the most important rheological property for buildability. Chapter two also inferred that materials' yield stress is only vital at earlier layers and stages of the printing process where yielding failure has a probability of occurrence (depending on the loading and printing rate). Overestimation of buildability using Euler's theory, suggested that in the future, imperfections in a vertically printed element must be considered. In the future, realistic geometrical deviations from a straight and vertical element during 3D-printing must be taken into account and be incorporated in the prediction of buildability using Euler's linear elastic model. The assumption of linear elasticity itself can be further examined in early-ages of cement pastes and mortars using direct input from the materials' deformation (such as yielding and buckling) during the 3D-printing process.

Chapter three affirmed that the processing-induced interfaces are indeed porous and, therefore, weak. In this chapter, several other microstructural features (including macro-pores, micro-channels, micro-pores) were found. Chapter four revealed that in micro-channels and micro-pores that were thought to be connected at a large resolution were indeed connected at a smaller resolution. A connected pore network was, therefore, claimed. In the future, this line of research can be explored by investigating means to control the pore network that enables the fabrication of novel and advanced material.

Chapter five confirmed that bio-inspired designs of cement-based materials are possible. It also concluded that the weak interface could be harnessed to improve mechanical response and flexural properties of brittle materials such as cement paste. It verified that combining such weak interfaces, combined with clever architectures such as Bouligand elements leads to delocalization of the damage in the brittle materials and allows for a ductile behavior and enhanced toughness, without sacrificing the strength, in comparison to cast elements that are made of the same materials. In the future, the advantages mechanical characteristics of novel architectures, some of which can

be found in nature, can be further explored using a layer-by-layer 3D-printing process that allows for embedment of flaws such as weak interfaces in the material.

Chapter six confirmed that made certain that the materials' internal arrangements such as Bouligand and lamellar architectures, dictates the overall mechanical response and in the fracture behaviors under compressive loads, some anisotropic and all distinctly different from the cast counterparts. It also determined that Bouligand architectures combined with weak interfaces improved toughness without sacrificing the strength, in comparison to cast counterparts. While this chapter focused on post-mortem fracture behaviors, future directions can focus improving the understanding of the mechanical response of 3D-printed elements and provides insight for developments at large scales.

In summary, the findings of this dissertation put forward new knowledge in the areas of early-age deformations of cement-based materials and design of cement-based structures fabricated using additive manufacturing technologies. Chapter two demonstrated the two mechanisms concerning the shape stability of 3D-printed elements, yield, and buckling. This chapter translates the shape stability requirements into the most relevant material rheological properties in the development of 3D-printed elements. Chapter three and chapter four, resolve the questions about the characteristics of the interfaces and reveal the 'weak' and 'interconnected' nature of the interfaces of 3D-printed elements, though, these characteristics can be highly processing-dependant. Chapter five and chapter six demonstrated a new pathway in the design of brittle and quasi-brittle materials in tension and compression. These chapters put forward prospective ideas for novel performance characteristics, including compliancy, improved ductility, and toughness. These pathways can serve as a precursor for the structural design of plain cement-based structures. However, they are additionally valuable when combined with other advancements in construction materials and technologies such as alternative fibers and topology optimization.